

QATAR UNIVERSITY

COLLEGE OF ARTS AND SCIENCES

OPTIMIZATION AND STABILIZATION OF P-TYPE BISBTE/GRAPHENE

NANOCOMPOSITES FOR EFFICIENT THERMOELECTRIC ENERGY CONVERSION

BY

AICHA SIDI LEMINE

A Thesis Submitted to

the College of Arts and Sciences

in Partial Fulfillment of the Requirements for the Degree of

Masters of Science in Material Science and Technology

January 2020

© 2020 Aicha Sidi Lemine. All Rights Reserved.

## COMMITTEE PAGE

The members of the Committee approve the Thesis of  
Aicha Sidi Lemine defended on [Defense Date].

---

Dr. Khaled Youssef  
Thesis/Dissertation Supervisor

---

Dr. Ahmad Ayesh  
Committee Member

---

Dr. Ahmed Elzatahry  
Committee Member

---

Dr. Ahmed Abdala  
Committee Member

Approved:

---

Ibrahim Al-Kaabi, Dean, College of Arts and Sciences

## ABSTRACT

LEMINE, AICHA, SIDI, Masters :

January : 2020, Material Science and Technology

Title: Optimization and Stabilization of p-type BiSbTe/Graphene Nanocomposites for Efficient Thermoelectric Energy Conversion

Supervisor of Thesis : Khaled, Mohamed, Youssef.

The state-of-the-art Bismuth Antimony Telluride (BiSbTe) alloys have a promising potential to advance thermoelectric applications in energy harvesting for efficient power generation and active refrigeration. In this thesis, the combination of High-Energy Ball Milling and FAST/SPS Sintering Press showed a reliable and cost-effective synthesis approach for artifact-free nanostructured bulk BiSbTe/Graphene nanocomposites. The results show successfulness in synthesizing homogenous elemental distribution and stable single phase of  $\text{Bi}_{0.4}\text{Sb}_{1.6}\text{Te}_3$  either in the pristine nanopowder or the multicomponent nanocomposites. It also confirms the crucial rule of graphene addition time on its structure, as well as, the morphology, mechanical behavior, and thermoelectric performance of the synthesized nanocomposites. The 5mins nanocomposite showed an ultrahigh micro-hardness of 1.78GPa, the highest power factor of  $1.73\text{mW}/\text{m}\cdot\text{K}^2$  at 323K, and the lowest thermal conductivity of  $0.723\text{W}/\text{m}\cdot\text{K}$  at 323K. This has resulted in its optimum Figure-of-Merit of 0.70 at 323K with 25% of improvements compared to the pristine BiSbTe.

## DEDICATION

*To who taught me "My philosophy all my life has been the pursuit of excellence". I truly follow a similar approach towards life, as you have recommended. Thus, I am currently in pursuit of excellence through the application to this master's degree and I am lovingly dedicating it to you.*

## ACKNOWLEDGMENTS

The master's degree with Materials Science and Technology Master Program (MATS) was a beneficial chance to me for learning and professional development. In which I got frequent support and guidance by a group of esteemed individuals to accomplish this degree in a professional manner, thus thanking them is the least right toward this grace. First and foremost, I would like to express my thanks to God, who gave me the health and strength to take advantage of this opportunity to the extreme.

Additionally, I would like to thank Qatar University and staff members in its sciences college, especially the coordinator of MATS program, Dr. Talal Altahtamouni for giving me this valuable opportunity to learn and gain work experience, which is a milestone in my learning and career development. Also, many thanks to my thesis supervisor, Dr. Khaled Youssef for his excellence in supervision and devotion in directing this thesis.

Furthermore, I would like to extend my gratitude to my committee members for their kindness and guidance namely: Dr. Ahmad Ayesh, Dr. Ahmed Elzatahry, and Dr. Ahmed Abdala. Besides that, I would like to express my deepest gratitude and special thanks to the Central Lab Unit at QU (CLU), Center for Advanced Materials (CAM), and Core Lab Unit at QEERI (CLU) and their staff members for their indispensable contribution in data analysis within this thesis research.

Last but not the least, I would like to thank all of my colleagues with whom I worked with during this program, particularly my batch the "Material Scientists Group". Finally, I am highly indebted to my family members for untiring assistance and encouragement throughout this graduate study. I consider myself a very lucky individual for their presence in my life and I always pray to God to bless all of them.

## TABLE OF CONTENTS

DEDICATION .....	iv
ACKNOWLEDGMENTS .....	v
LIST OF TABLES .....	x
LIST OF FIGURES .....	xii
CHAPTER 1: INTRODUCTION .....	1
1.1 Thesis Research: Significances & Novelty .....	1
1.2 Thesis Research: Objectives & Hypothesis.....	2
CHAPTER 2: LITERATURE REVIEW.....	5
2.1 Thermoelectrics: Historical Development.....	5
2.2 Thermoelectrics: Technology Definition .....	7
2.3 Thermoelectrics: Principles of Energy Conversion .....	9
2.3.1 Thermoelectric Model of Power Generation (Seebeck Effect) .....	10
2.3.2 Thermoelectric Model of Active Refrigeration (Peltier Effect) .....	12
2.4 Thermoelectrics: Device Module.....	14
2.5 Thermoelectrics: Remarkable Properties .....	18
2.5.1 Low Thermal Conductivity (k) .....	18
2.5.1.1 Lattice Phonon Thermal Conductivity ( $k_L$ ) .....	19
2.5.1.2 Electronic Thermal Conductivity ( $k_e$ ) .....	21
2.5.2 High Electrical Conductivity ( $\sigma$ ) .....	22
2.5.2.1 Seebeck Coefficient (S) .....	22
2.5.2.1.1 Charge Carriers Diffusive Seebeck Coefficient ( $S_d$ ) .....	23
2.5.2.1.2 Lattice Phonon Drag Seebeck Coefficient ( $S_g$ ) .....	24
2.5.2.2 Electrical Mobility & Resistivity .....	24

2.5.3 High Power Factor (PF) .....	25
2.5.4 High Figure-of-Merit (ZT) .....	26
2.5.5 High Thermoelectric Efficiency ( $\eta_p$ or $\eta_c$ ) .....	28
2.5.6 High Nanostructuring Thermal Stability .....	28
2.6 Thermoelectrics: Promising Materials Systems.....	32
2.6.1 Promising P-type $\text{Bi}_2\text{Te}_3$ -Based TE Systems ( $\text{Bi}_{2-x}\text{Sb}_x\text{Te}_3$ ) .....	37
2.7 Thermoelectrics: Advancing Approaches .....	37
2.7.1 Phonon Transport Engineering .....	37
2.7.1.1 Atomic Doping/Alloying .....	38
2.7.1.2 Nanostructuring .....	39
2.7.1.3 Nanoemulsions .....	40
2.7.2 Charge Transport Engineering .....	43
2.7.2.1 Nanocomposite .....	43
2.8 Thermoelectrics: Synthesis & Sintering Techniques .....	46
2.8.1 TE Synthesis Techniques: High-Energy Ball Milling (HE-BM) .....	47
2.8.2 TE Sintering Techniques: FAST/SPS Sintering Press (DSP-510) .....	49
CHAPTER 3: RESEARCH EXPERIMENTAL METHODOLOGY .....	52
3.1 Thesis Research: Specimens Preparations.....	52
3.2 Thesis Research: Processing Methods .....	55
3.2.1 TE Nanopowder Synthesis Method: High-Energy Ball Milling (HE-BM) .....	55
3.2.2 TE Nanopowder Sintering Method: FAST/SPS Sintering Press (DSP-510)	
.....	58
3.3 Thesis Research: Characterization Techniques .....	61
3.3.1 Structural Characterization Techniques .....	61

3.3.1.1 X-Ray Diffractometer (XRD) Instrument .....	61
3.3.1.2 Transmission Electron Microscope (TEM) .....	65
3.3.1.3 Raman Microscope.....	68
3.3.2 Mechanical Characterization Techniques .....	71
3.3.2.1 Vickers Micro-Hardness Tester Instrument .....	71
3.3.3 Thermal Characterization Techniques .....	75
3.3.3.1 Differential Scanning Calorimeter (DSC) Instrument .....	75
3.3.4 Thermoelectric Characterization Techniques.....	77
3.3.4.1 NETZSCH SBA-458 Nemesis Instrument.....	77
3.3.4.2 NETZSCH LFA-467 HyperFlash-Light Flash Apparatus .....	79
CHAPTER 4: RESEARCH RESULTS & DISCUSSIONS .....	82
4.1 Structural Characterization.....	82
4.1.1 X-ray Diffraction Analysis of the Pristine $\text{Bi}_{0.4}\text{Sb}_{1.6}\text{Te}_3$ Nanopowders.....	82
4.1.2 X-ray Diffraction Analysis of the Graphene/ $\text{Bi}_{0.4}\text{Sb}_{1.6}\text{Te}_3$ Nanocomposites .....	85
4.1.3 TEM Analysis of the Pristine and the Nanocomposites Samples .....	88
4.2 SPS Consolidation.....	93
4.2.1 Thermal Analysis of the Pristine and the Nanocomposites Samples .....	93
4.2.2 Structural Analysis of the Consolidated Samples .....	98
4.3 Mechanical Characterization .....	101
4.3.1 Mechanical Properties of the Pristine $\text{Bi}_{0.4}\text{Sb}_{1.6}\text{Te}_3$ Nanopowders .....	101
4.3.2 Mechanical Properties of the Graphene/ $\text{Bi}_{0.4}\text{Sb}_{1.6}\text{Te}_3$ Nanocomposites ....	102
4.4 Thermoelectric Properties.....	108
CHAPTER 5: CONCLUSIONS & RECOMMENDATIONS.....	113



5.1 Thesis Research: Conclusions .....	113
5.2 Thesis Research: Recommendations .....	117
REFERENCES .....	119

## LIST OF TABLES

Table 2.1 The Summary of the Atomic Dimensions and Crystal Structure, Physical Properties, Thermal Properties, Electrical Properties, and Mechanical Properties of Constituents' Elements for $\text{Bi}_{2-x}\text{Sb}_x\text{Te}_3$ TE Material.....	38
Table 2.2 The Summary of the Outstanding Properties for 2D Graphene Material.....	46
Table 3.1 The Summary of Raw Materials Utilized in this Thesis Research .....	56
Table 3.2 The Atomic Composition, Mass Composition, and Elemental Weight for Specimens Preparations .....	57
Table 3.3 The Common Conditions of High-Energy Ball Milling Adopted for Specimens Preparations .....	60
Table 3.4 The Common Conditions of FAST/SPS Sintering Press (DSP-510) Adopted for Consolidating the Pre-Synthesized Nanopowder Specimens .....	64
Table 3.5 The Uniform Operating Conditions of PANalytical XRD Instrument (EMPYREAN model) on Pre-Synthesized Nanopowder Specimens .....	67
Table 3.6 The Uniform Operating Conditions of DXR Raman Microscope Instrument on Pre-Synthesized Nanopowder Specimens .....	75
Table 3.7 The Uniform Operating Conditions of Carver Hydraulic Laboratory Press Instrument for Cold compaction of Pre-Synthesized Nanopowder Specimens.....	77
Table 3.8 The Uniform Operating Conditions of Vickers Micro-hardness Tester Instrument on Cold-Compacted Specimens .....	79
Table 3.9 The Uniform Operating Conditions of Q-2000 Differential Scanning Calorimetry (DSC) Instrument on Nanopowder Specimens .....	82

Table 3.10 The Uniform Operating Conditions of NETZSCH SBA-458 Nemesis® Instrument on Pre-Consolidated Nanopowder Specimens .....	84
Table 3.11 The Uniform Operating Conditions of NETZSCH LFA-467 Instrument on Pre-Consolidated Nanopowder Specimens .....	86

## LIST OF FIGURES

Figure 2.1 Vital sectors for waste heat recovery via Thermoelectric Generators (TEGs).....	9
Figure 2.2 The German physicist Thomas Seebeck (a), the schematic representation for the thermoelectric model of power generation (b), and the diagram of power generation efficiency in terms of $ZT_{avg}$ (c).....	10
Figure 2.3 The French physicist Jean Peltier (a), the schematic representation for the thermoelectric model of active cooling (b), and the diagram of active cooling efficiency in terms of $ZT_{avg}$ (c).....	13
Figure 2.4 The Schematic representations of typical thermoelectric device modules (a) and it's alternating n-type and p-type thermoelectric materials connected electrically in series and thermally in parallel (b).....	15
Figure 2.5 The Schematic representations of the most common architectures for thermoelectric device modules and examples on the applications that they can fit properly.....	19
Figure 2.6 The Flow chart of the common effective phonon scattering mechanisms for bulk scale and nanoscale thermoelectric materials.....	21
Figure 2.7 The Thermoelectric properties in terms of free carrier concentrations for the main classes of materials .....	31
Figure 2.8 The Schematics of energy-band diagrams for insulators, semiconductors, and conductors.....	32
Figure 2.9 The Figure-of-merit (ZT) in terms of the absolute temperature for the promising TE systems in both p-type (a) and n-type (b).....	34
Figure 2.10 The Figure-of-merit (ZT) in terms of the absolute temperature for the p-	

type $\text{Bi}_x\text{Sb}_{2-x}\text{Te}_3$ in different alloying compositions (x) .....	36
Figure 2.11 The Rhombohedral and quintuple layered crystal structure of promising $\text{Bi}_{0.4}\text{Sb}_{1.6}\text{Te}_3$ system for TE applications of low-temperatures .....	37
Figure 2.12 The Accumulated percentage of lattice thermal conductivity ( $k_{\text{lat}}$ ) in terms of phonon mean free path (a) and the corresponding ZT values (b) for different phonon scattering approaches on multiple length scales .....	42
Figure 2.13 The Schematic representation of various advancing approaches based on phonon transport engineering for multiple length-scale phonon scattering .....	44
Figure 2.14 The Schematic representation of charge carriers filtering effect at SiC nano inclusions and $\text{Bi}_{0.3}\text{Sb}_{1.7}\text{Te}_3$ interface .....	45
Figure 2.15 The Schematic representations of various graphitic materials based on the 2D graphene sheet .....	47
Figure 2.16 The Dependence of lattice (a) and total (b) thermal conductivities on the variations of graphene content (x in wt.%) for $\text{Bi}_{0.48}\text{Sb}_{1.52}\text{Te}_3$ /graphene nanocomposites .....	48
Figure 2.17 The Variations of ZT with graphene content (x in wt.%) for $\text{Bi}_{0.48}\text{Sb}_{1.52}\text{Te}_3$ /graphene nanocomposites .....	49
Figure 2.18 The Improved ZT and reduced lattice thermal conductivity ( $k_{\text{lat}}$ ) for various micro and nanoscale TE materials synthesized via HE-BM technique .....	51
Figure 2.19 The Schematics for conventional hot pressing (a) and advanced FAST/SPS (b) sintering techniques of high-performance TE materials .....	53
Figure 3.1 The mBRAUN-LABstar Glovebox workstation (a) and its touch panel (b) along with Ohaus balance weighting equipment (c) .....	59
Figure 3.2 The SPEX SamplePrep 8007 Stainless Steel grinding vial set including a	

screw-on cap with O-ring and stainless-steel balls (a). The SPEX SamplePrep 8000-series Mixer/Mills (b) with single-clamp (c) and schematic of its high-energy ball milling process (d) ..... 61

Figure 3.3 The FAST/SPS Sintering Press (DSP-510) (a) and schematics of its internal parts (b) and sintering process (c) for uniaxial consolidation (d) of nanopowder into a dense disc with the target dimensions (e) ..... 63

Figure 3.4 The PANalytical X-Ray Diffractometer (XRD) instrument of EMPYREAN model (a) and schematics diagrams for its operating principle (b) and Bragg's law parameters (c) along with used sample holder for nanopowder specimens (d)..... 66

Figure 3.5 The Thermo Scientific High-Resolution Transmission Electron Microscope (HR-TEM) instrument of Talos F200C model (a) and schematic diagram for its electron column (b) along with the used FEI Versa 3D Dual Beam FIB/SEM instrument (c) for specimens thinning (d)..... 70

Figure 3.6 The Thermo Scientific DXR Raman microscope instrument (a) and the used DXR 532nm FILTER for laser excitation (b) of specimens placed over clear glass microscope slides (c) under Raman microscope (d) to obtain their Raman spectrum (e) ..... 73

Figure 3.7 The Carver Hydraulic Laboratory Press instrument of 4386 Model (a) with the used Tungsten Carbide die and rods (b) along with its gauge reads (c). The compacted discs placed over quartz cylinder in specimen holder (d) prior being grinded/polished using Metkon Grinder/Polisher automatic machine with double wheels and FORCIPOL-2V model (e) ..... 76

Figure 3.8 The Future Tech. Vickers Micro-hardness Tester instrument of FM-ARS9000 model (a) with diamond indenter placed above-tested specimen (b) and

schematic diagram for the resulted Vickers diamond square-based pyramid (c) .....	78
Figure 3.9 The TA Differential Scanning Calorimeter (DSC) instrument of Q2000 model (a) with its DSC cell containing the reference and sample pans (b) made up of Tzero Aluminum (c) along with schematic diagram on its DSC cell arrangements (d) .....	80
Figure 3.10 The NETZSCH SBA-458 Nemesis <sup>®</sup> instrument (a) and the entire sample setup (b) along with its schematic diagrams for sample setup (c), measurements of electrical conductivity (d), and Seebeck coefficient (e) .....	83
Figure 3.11 The NETZSCH LFA-467 HyperFlash-Light Flash Apparatus (a) and the entire sample setup (b) along with its schematic diagram for sample setup (c) and light flash technique (d) .....	85
Figure 4.1 The XRD patterns of the pristine Bi <sub>0.4</sub> Sb <sub>1.6</sub> Te <sub>3</sub> nanopowders (a) milled at 4, 8, 12, 16, and 20 hours. The Effect of milling time on average grains size (in blue) and microscopic lattice strain (in green) of pristine Bi <sub>0.4</sub> Sb <sub>1.6</sub> Te <sub>3</sub> nanopowders (b) based on the integral breadth analysis on their XRD patterns using Warren-Averbach method.....	88
Figure 4.2 The XRD patterns of the Graphene nanoplatelets alone and 0.05wt% Graphene/Bi <sub>0.4</sub> Sb <sub>1.6</sub> Te <sub>3</sub> nanocomposites (a) milled at full time, half time, last 1hr, and last 5min of overall 16hr. The Effect of graphene milling time on average grains size (in blue) and microscopic lattice strain (in green) of 0.05wt% Graphene/Bi <sub>0.4</sub> Sb <sub>1.6</sub> Te <sub>3</sub> nanocomposites (b) based on the integral breadth analysis on their XRD patterns using Warren-Averbach method.....	91
Figure 4.3 The Comparative linear regressions on the pristine BiSbTe at 16hr milling and the 5mins milled nanocomposite based on the integral breadth analysis on their	

XRD patterns using the Warren-Averbach method for precise calculations of their grain size and lattice strain.....93

Figure 4.4 The HR-TEM observations of typical nanostructures in the pristine  $\text{Bi}_{0.4}\text{Sb}_{1.6}\text{Te}_3$  nanopowder synthesized at 16hr of milling via its bright (a) and dark (b) field TEM micrographs. The upper right inset in (a) is the SADP and shows the equiaxed nanograins in random orientations. A similar nanostructure is observed in 0.05wt% Graphene/ $\text{Bi}_{0.4}\text{Sb}_{1.6}\text{Te}_3$  nanocomposite synthesized at the last 5min of overall 16hr milling as illustrated in its bright (d) and dark (e) field TEM micrographs and the upper right inset in (d) is its SADP. The statistical grain size distribution plots of pristine  $\text{Bi}_{0.4}\text{Sb}_{1.6}\text{Te}_3$  nanopowder and 0.05wt% Graphene/ $\text{Bi}_{0.4}\text{Sb}_{1.6}\text{Te}_3$  nanocomposite are shown in (e) and (f), respectively. .... 95

Figure 4.5 The Recognition of twinning interfacial defect in the 0.05wt% Graphene/ $\text{Bi}_{0.4}\text{Sb}_{1.6}\text{Te}_3$  nanocomposite synthesized at the last 5min of overall 16hr milling as illustrated in its high-magnification bright-field TEM micrograph (a) and SADP (b). It is clear in the SADP (b) that the nanocrystals on either side are the mirror images of the other side. .... 97

Figure 4.6 The DSC heating curves (a) and cooling curves (b) with the onset temperatures for melting and crystallization peaks for two continuous thermal cycles conducted at a constant heating rate of  $10^\circ\text{C}/\text{min}$  on the pristine  $\text{Bi}_{0.4}\text{Sb}_{1.6}\text{Te}_3$  nanopowder at 16hr milling and 0.05wt% Graphene/ $\text{Bi}_{0.4}\text{Sb}_{1.6}\text{Te}_3$  nanocomposites.. 99

Figure 4.7 The HAADF-STEM images and their corresponding EDS elemental mapping analysis on Bismuth (Bi), Antimony (Sb), and Tellurium (Te) atoms distribution in the pristine  $\text{Bi}_{0.4}\text{Sb}_{1.6}\text{Te}_3$  nanopowder synthesized at 16hr of milling (top row) and 0.05wt% Graphene/ $\text{Bi}_{0.4}\text{Sb}_{1.6}\text{Te}_3$  nanocomposite synthesized at the last 5min



of overall 16hr milling (bottom row).....	101
Figure 4.8 The Effect of graphene milling time on the normalized enthalpies of melting (in red) and crystallization (in blue) for two continuous thermal cycles conducted at a constant heating rate of 10°C/min on pristine Bi <sub>0.4</sub> Sb <sub>1.6</sub> Te <sub>3</sub> nanopowder at 16hr milling (non-linked squares) and 0.05wt% Graphene/Bi <sub>0.4</sub> Sb <sub>1.6</sub> Te <sub>3</sub> nanocomposites (linked squares). .....	102
Figure 4.9 The XRD patterns of sintered pellets for pristine BiSbTe and 0.05wt% Graphene/Bi <sub>0.4</sub> Sb <sub>1.6</sub> Te <sub>3</sub> nanocomposites (a) milled at full time, half time, last 1hr, and last 5min of overall 16hr. The top inset shows in-plane surface of as-pressed disc perpendicular to its SPS pressing. The Effect of graphene milling time on average grains size (in blue) and microscopic lattice strain (in green) of sintered pellets for pristine BiSbTe and Graphene/Bi <sub>0.4</sub> Sb <sub>1.6</sub> Te <sub>3</sub> nanocomposites (b) based on integral breadth analysis on their XRD patterns using Warren-Averbach method.....	105
Figure 4.10 The Effect of milling time on the average Vickers micro-hardness (in blue) and average grain size (in green) of pristine Bi <sub>0.4</sub> Sb <sub>1.6</sub> Te <sub>3</sub> nanopowders.....	107
Figure 4.11 The Effect of graphene milling time on average Vickers micro-hardness (in blue) and average grain size (in green) of 0.05wt% Graphene/Bi <sub>0.4</sub> Sb <sub>1.6</sub> Te <sub>3</sub> nanocomposites. ....	108
Figure 4.12 The Raman spectra of the reference graphene nanoplatelets, 16hr milled pristine Bi <sub>0.4</sub> Sb <sub>1.6</sub> Te <sub>3</sub> nanopowder, and 0.05wt% Graphene/Bi <sub>0.4</sub> Sb <sub>1.6</sub> Te <sub>3</sub> nanocomposites (a) at DXR laser excitation of 532nm. The Effect of graphene milling time on the 2D band intensity to G band intensity ratio (I <sub>2D</sub> /I <sub>G</sub> ratio) (in blue) indicates the dramatic change in the number of graphene layers (in green) present in the synthesized 0.05wt% Graphene/Bi <sub>0.4</sub> Sb <sub>1.6</sub> Te <sub>3</sub> nanocomposites (b).....	110

Figure 4.13 The Evolutions of D, G, 2D, and D+G bands in the Raman spectra of the reference graphene nanoplatelets, 16hr milled pristine  $\text{Bi}_{0.4}\text{Sb}_{1.6}\text{Te}_3$  nanopowder, and 0.05wt% Graphene/ $\text{Bi}_{0.4}\text{Sb}_{1.6}\text{Te}_3$  nanocomposites at DXR laser excitation of 532nm. ....112

Figure 4.14 The Temperature dependence of thermoelectric parameters: Electrical conductivity (a), Seebeck coefficient (b), Power factor (c), Total thermal conductivity (d), Lattice thermal conductivity (e), and Figure-of-Merit (f) for SPS pellets of the pristine  $\text{Bi}_{0.4}\text{Sb}_{1.6}\text{Te}_3$  at 16hr milling and 0.05wt% Graphene/ $\text{Bi}_{0.4}\text{Sb}_{1.6}\text{Te}_3$  nanocomposites. ....116

# Chapter 1: INTRODUCTION

## 1.1 Thesis Research: Significances & Novelty

A recent study by the US Energy Information Administration (EIA) predicted a vast growth in the worldwide energy consumption from 495 quadrillion BTU in 2007 to 739 quadrillion BTU in 2035 by 1.4% per year [1]. This continuous demand for energy is in parallel to the rapid growth in population and economic activities. Thus, it is challengeable to fulfill this demand on a massive scale by burning non-renewable fossil fuels, which currently covers most of it [2]. However, relying on these fuels has raised serious concerns about the consequences of their combustion in terms of long-term sustainability and global warming. Nowadays, there is a global perception of these consequences and unremitting efforts towards investing in optimizing Carbon-free alternative energy sources [2]. The State of Qatar is one of the leading countries in green energy technologies and top participants in reducing global warming [3]. Thus, it invests continuously in advancing thermoelectric (TE) materials and optimizing their synthesis techniques, which are one main objective of sustainable energy development towards achieving the 2030 Qatar National Vision.

The selective investment in TE technology is referred to its unique capability for effective recovering of waste heat from intensive electricity consumption sectors and converting it into useful electrical energy for powering their electronic devices, lowering their operating costs, and minimizing their greenhouse emissions [4]. Accordingly, TE technology has the potential to play a key role in overcoming the global energy challenge in the 21<sup>st</sup> century; as it is neither limited by region (e.g. water) nor time (e.g. solar and wind), hence ensuring continued and balanced power supplies [4]. This leading power generation technology is inspiring the researching

community for more breakthroughs in rising its energy conversion efficiency for long-term operation and worldwide commercialization. Herein, this master thesis is researching on the optimization and stabilization of the p-type Bismuth Antimony Telluride system (BiSbTe) and Graphene nanocomposites for efficient TE energy conversion. It spotlights for the first time on the effect of nanostructuring, doping, and nanocompositing on thermal stabilization and TE performance of the p-type BiSbTe with exclusive highlights on its:

- Reliable synthesizing and consolidating techniques
- Crystallinity and nanostructure evolutions
- Mechanical behavior
- Thermal behavior
- Thermoelectric performance

## **1.2 Thesis Research: Objectives & Hypothesis**

This thesis research is designed based on a set of objectives including:

1. Synthesizing a nanostructured p-type BiSbTe towards maximizing the Figure-of-Merit (ZT) of TE device.
2. Utilizing the unique properties of 2D Graphene in upgrading the efficiency of energy conversion in the synthesized nanostructured bulk TE material.
3. Sufficiently stabilizing the synthesized nanocomposite for reliable service.

These objectives will be accomplished by adopting the following hypothesis to further optimize the energy conversion efficiency of Bi-Te system:

1. Nanostructuring of Bi-Te Alloy

It is an effective approach to upgrade TE performance by the quantum confinement effect in which the grain size will decrease to nanoscale. This will increase the number of grain boundaries that will act as phonon scattering sites to lower significantly lattice thermal conductivity, which will in turn increase ZT. These new boundaries will act also as barriers for dislocations motion and then strengthening the mechanical behavior of synthesized TE nanocomposite. This approach will be accomplished via the implementation of High-Energy Ball Milling technique, which is a well-known novel and cost-effective technique for mechanical alloying of nanopowders [5].

## 2. Resonant Level Doping

It's the most important strategy of band engineering as it is proven with advantages in enhancing the TE performance of nanostructured Bi-Te system [5]. The doping will change the charge carrier concentration ( $n$ ), increase the Seebeck coefficient ( $S$ ), introduce defects into nanocrystalline Bi-Te powder, and decrease thermal conductivity ( $k$ ). The dopant element will be Antimony (Sb) which is a common dopant for p-type Bi-Te. The ZT enhancement for p-type BiSbTe is much easier than n-type BiSeTe due to strong texture and high anisotropic properties of n-type as frequently reported [6].

## 3. Nanocompositing with 2D Graphene

It will be utilized in forming a nanocomposite with p-type BiSbTe due to its exceptional intrinsic properties that fulfill TE standards including its: high electrical charges mobility and conductivity, high mechanical

stiffness and strength, and high specific surface area [6]. The structure of the synthesized nanocomposite will enhance the carriers' mobility via strengthening the carrier energy filtering effect. This effect is based on filtering out the low energy carriers via scattering them at the interfacial potential of filler and matrix to allow only the high energy carriers passing through. This will increase the power factor (PF) and Seebeck coefficient (S) with a negligible decrease in electrical conductivity ( $\sigma$ ). However, the use of graphene in TE technology has limitations and needs optimization of its composition in the BiSbTe matrix due to its high thermal conductivity that will lower significantly TE energy conversion efficiency.

#### 4. Nanostructuring Thermal Stabilization for Synthesized Nanocomposite

It's an important approach to maintain the performance of the TE device, prevent its failure, and extend its life cycle for reliable service and sustainable power generation. This will be attained by investigating the thermal behavior of synthesized BiSbTe/Graphene nanocomposites. This investigation will also participate in verifying the proper consolidating conditions using the Spark Plasma Sintering (SPS) technique to stabilize its bulk nanostructure. This will significantly modify TE properties of final product and prevent growth of nanocrystals under continuous exposure to high thermal stresses during its operation.

## **Chapter 2: LITERATURE REVIEW**

### **2.1 Thermoelectrics: Historical Development**

In 1820, the thermoelectric effect was discovered in Western Europe via a group of recognizable scientists and its early studies were initiated in Berlin [7]. This effect is a two-way process in which a temperature gradient across the material can be tuned to promote the production of electric current and vice versa. The first process of heat-to-electricity conversion was discovered by a German physicist named Thomas Seebeck in 1821 [7]. Then it was further explored in detail in 1834 by a French physicist named Jean Peltier, hence it was later on reported as the Peltier-Seebeck effect [8]. The second process of electricity-to-heat conversion was discovered by a Scottish-Irish physicist named William Thomson (i.e. Lord Kelvin) in 1854 [8]. This reverse process states that either cooling or heating can be implemented via application of an electric current across thermoelectric material and such effect is known as Thomson effect.

Thereafter, a German scientist named Edmund Altenkirch was able to correctly calculate the potential efficiency of thermoelectric generators in 1909 and the performance of thermoelectric coolers in 1911 [9]. These derivatives were developed later into a significant formula for calculating a dimensionless parameter that can be utilized in practical applications to characterize the efficiency of thermoelectric devices; such parameter is known as Thermoelectric Figure-of-Merit (ZT). Then in 1928, a Russian physicist named Abram Loffe was able to describe the phenomenon of thermoelectric energy conversion in terms of the modern theory of semiconductor quantum physics, which was a pioneer work in understanding and engineering such phenomenon [9]. Consequently, in 1930 the first radio powered by a thermoelectric generator was publicized and in 1959 the first equipped spacecraft with Radioactive Thermoelectric Generator (RTG) named “SNAP III” was launched by US president

Dwight Eisenhower to orbit the earth as a navigational satellite [10]. Additionally, in 1970 the Medtronic Healthcare Company in France developed a miniature RTG to power the first cardiac pacemaker implanted into the human body [11].

Later on in 1993, a remarkable theory paper entitled of “Effect of Quantum Well Structures on the Thermoelectric Figure of Merit” was published by Hicks and Dresselhaus to highlights on the significance of nanotechnology as a new and effective approach for rapid advances in thermoelectrics performance; hence it was the milestone for the modern era of thermoelectrics [12]. As a result, the scientist John Fairbanks in 1995 initiated a research program in the US to develop nanostructure-based thermoelectric generators to be incorporated into automotive engines in order to harvest its waste heat energy into useful electrical energy [13]. The program was also able to develop successfully a nano-FeSi based thermoelectric prototype for Porsche automobile manufacturer. Additionally, in 1998 the Japanese Seiko Holding Corporation launched the Thermic wrist-worn watch based on a nanoscale BiTe thermoelectric generator to be the first-ever watch that’s fully powered from body heat [14].

Furthermore, the Gentherm Incorporated was successfully able to create in 1999 the first thermoelectric heating/cooling seat system for the automotive industry using nanostructured BiTe material [14]. This leading-edge system was firstly adopted by the American Ford motor company in its Lincoln Navigator luxury brand and the Japanese automaker Toyota in its Lexus luxury brand [15]. In 2004, the global awareness to the negative impacts of global warming on the vital signs of earth planet was the main driving force for devoting special attention to intensive research on new, green, and advancing technologies to lower burning of fossil fuel and emission of greenhouse gases without affecting the growing human and industrial activities.



Consequently, the BMW in conjunction with the US Department of Energy (DOE) funded a recent research program for advancing automotive thermoelectric generators for engines waste heat recovery to reduce fuel consumption and pollutant emission [15]. Nowadays, there is extensive research on engineering nanostructured thermoelectric materials to form powerful thermoelectric generators for waste heat recovery on a larger scale, particularly in industrial plants.

## **2.2 Thermoelectrics: Technology Definition**

Thermoelectric is a new, green, and promising future sustainable energy technology for efficient, direct, and reversible energy conversion between thermal energy and electrical energy using a novel class of materials known as thermoelectric materials. Currently, the economic crisis, global warming, global population growth, global energy crisis, increasing global consumption and demand of energy, fluctuating prices and diminish in stocks of non-renewable energy resources such as fossil fuel and coal have all drawn the global attention towards alternative energy harvesting and generation technologies, particularly thermoelectric technology [16]. This extensive and renewable interest in such technology is due to owing numerous unique features including: solid-state devices, no hazardous working fluids, small size and scalable devices, compact structure, no moving parts, noise-free, no pollutants emissions, Chlorofluorocarbons (CFC)-free, lowering Carbon Footprint, direct energy conversion, electric power generations, thermal management, high reliability and stability with negligible maintenance cost, simplicity, low cost electricity, high durability, and remarkable feasibility in wide range of temperatures [16–18].

As a result, it has the capability to fulfill the worldwide energy requirements and match the global environmental constraints on broad range of potential applications such as: waste heat recovery (e.g.: automobile engines), temperature measurements and

controls (e.g.: semiconductor lasers), heat pumps (e.g.: in industrial plants), solid-state coolers (e.g.: in compact refrigerators and in luxury cars seats), space power generation (e.g.: RTG), and in many other solid-state power generation and cooling/heating applications [19–21]. Additionally, there is a high need for conscious governments and research institutes to invest in the outstanding features and capabilities of thermoelectric technology towards harvesting waste heat energy into usable electrical energy. This is currently a paramount approach to increase its efficiency in energy conservation and conversion to be the worldwide promising competitor that will overcome the global future energy challenges and the catastrophic outcomes of conventional energy technologies [22].

Nowadays, the need of this paramount approach arises after the publication of the annual report for year 2018 by the Global Footprint Network in which it highlights on the urgent need for advanced energy technology to recover the large proportion of around 60-70% of the global applied energy carriers that are converted to unused thermal energy, mainly during various combustion processes conducted in vital sectors such as aerospace, industrial, automotive, and defense [23]. This considerable amount of energy lost indicates that only 20-30% of the originally feeding primary energy is used wisely, hence violating the global environmental constraints [23]. Additionally, its negative impacts on the environment will increase the Carbon Footprint and Ecological Footprint, hence the Global Footprint. Thus, the high-performance thermoelectric technology is a profitable and promising candidate to recover such considerably unutilized energy and directly converting it to usable electricity via the implementation of solid-state Thermoelectric Generators (TEGs) in such vital sectors as displayed in Figure 2.1 [24].

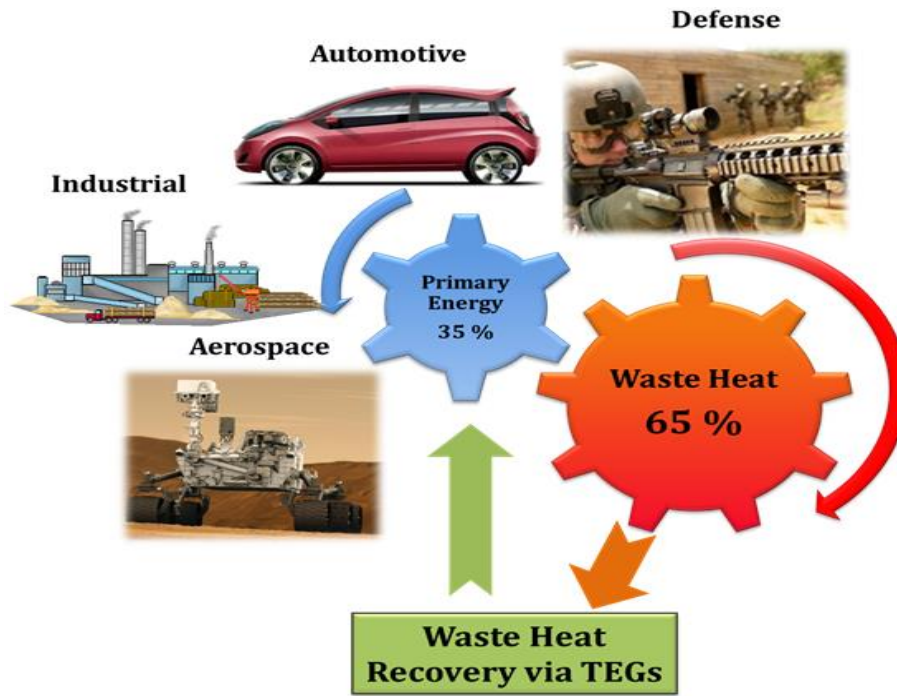


Figure 2.1 Vital sectors for waste heat recovery via Thermoelectric Generators (TEGs) [24].

For instance, TEGs could be used to utilize the waste heat in the automotive industry as from the exhaust pipe of the car and to convert it directly into electric power for supplying a set of electrical utilities within the car or charging its battery [25]. This strategy in the design of advanced automobiles will lower their pollutants emission due to the significant improvements in fuel burning efficiency. Consequently, the report also predicts that the market of thermoelectric energy harvesting will grow rapidly in the next 9 years to reach over \$1.5 billion by the end of 2028.

### 2.3 Thermoelectrics: Principles of Energy Conversion

The principle of energy conversion within thermoelectric (TE) materials depends on the presence of temperature gradient between its hot and cold sides that will derive its charge carriers (electrons and holes) to move in parallel direction to the

temperature gradient (from hot to cold side) due to their high thermal energy at the hot side [6]. These motions of charge carriers will build up an electric voltage across TE material leading to the generation of electricity via the flow of electric current, hence the complete conversion of thermal energy (i.e. presence of temperature gradient) to electrical energy (i.e. flow of electric current) [6]. This thermoelectric effect could be modeled into two different models namely: power generation model based on the Seebeck effect and active refrigeration model based on the Peltier effect as discussed below.

### 2.3.1 Thermoelectric Model of Power Generation (Seebeck Effect)

The Seebeck effect is the thermoelectric model of power generation, which is stated by the German physicist Thomas Seebeck (Figure 2.2 (a)) in 1821 based on his experimental observations of compass needle deflection in a closed electric circuit of two dissimilar conductive materials jointed with junctions at different temperatures [26]. He stated that the presence of temperature gradient across TE materials has induced voltage gradient and generated an electric current in the circuit, which in turn created a magnetic field that leads to the deflection of the compass needle.

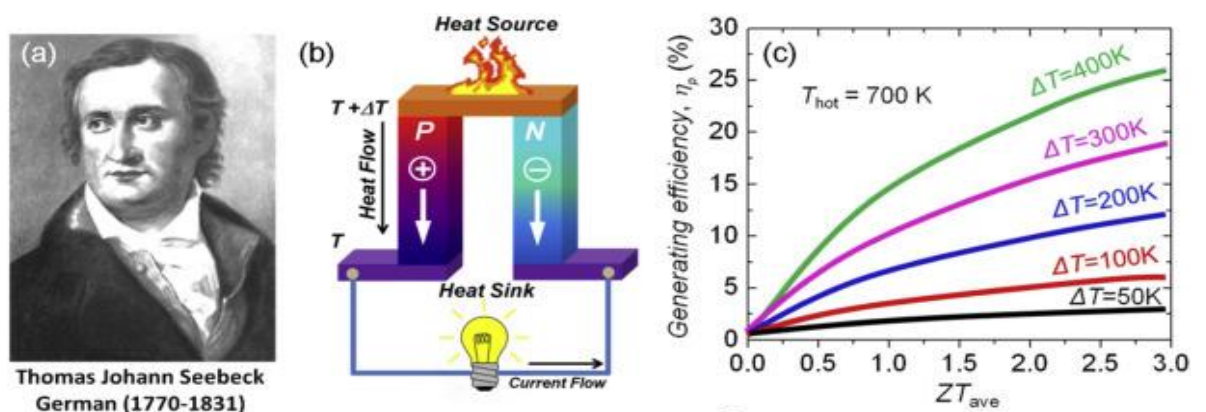


Figure 2.2 The German physicist Thomas Seebeck (a), the schematic representation

for the thermoelectric model of power generation (b), and the diagram of power generation efficiency in terms of  $ZT_{avg}$  (c) [27].

This phenomenon is well-known as Seebeck effect in which the application of different temperatures on the junctions will lead to that one of the junctions will act as a heat source ( $T+\Delta T$ ) while the other will be the heat sink ( $T$ ), as illustrated in Figure 2.2 (b) [27]. This will result in the formation of the temperature gradient ( $\Delta T$ ) across the jointed 2 dissimilar TE materials (p-type TE and n-type TE materials). This  $\Delta T$  acts as a thermoelectric force that will stimulate the different electric charge carriers (holes in p-type TE and electrons in n-type TE) to diffuse from hot side (i.e. high thermal energy regime) to cold side (i.e. low thermal energy regime). Consequently, the diffuse of these electric charges will lead to inhomogeneous charge distribution and formation of Seebeck electric voltage ( $\Delta V$ ) across TE material, hence inducing the generation of an electric current that can perform an electric work such as lightening the attached bulb to this TEG, as demonstrated in Figure 2.2 (b) [28].

The produced  $\Delta V$  is directly proportional to the applied  $\Delta T$  between the 2 junctions and its proportionality constant is termed as Seebeck coefficient ( $S$ ), which is a thermodynamic state function, as shown in Equation (2.1) [29]. The negative value of  $S$  indicates n-type TE material where the majority of charge carriers are electrons, while the positive value of  $S$  is for p-type TE material with holes as the majority of charge carriers [29].

$$S = \frac{-\Delta V}{\Delta T} \quad (2.1)$$

Additionally, the efficiency of this electrical power generation ( $\eta_p$ ) could be estimated as a function of Carnot cycle efficiency ( $\eta_{Carnot} = T_h - T_c / T_h$ ) for typical heat

engines, average of Figure-of-Merit ( $ZT_{avg}$ ) for both p-type and n-type TE materials in leg shape, and absolute hot ( $T_h$ ) and cold ( $T_c$ ) temperatures as shown in Equation (2.2) [30].

$$\eta_p = \eta_{Carnot} * \left[ \frac{\sqrt{1 + ZT_{avg}} - 1}{\sqrt{1 + ZT_{avg}} + T_c/T_h} \right] \quad (2.2)$$

The  $ZT_{avg}$  could be estimated for each leg through plotting its ZT curve over the absolute hot ( $T_h$ ) and cold ( $T_c$ ) temperatures at its hot and cold ends, respectively as displayed in Equation (2.3) [30].

$$ZT_{avg} = \frac{1}{T_h - T_c} \int_{T_c}^{T_h} ZT dT \quad (2.3)$$

Moreover, it could be observed from Figure 2.2 (c) that as the temperature gradient ( $\Delta T$ ) increases the  $ZT_{avg}$  will increase leading to an incremental in energy conversion efficiency, hence high power generating efficiency ( $\eta_p$ ). For instance, the rise of  $\Delta T$  from 50K to 400K at  $T_h$  of 700K and  $ZT_{avg}$  of 2.0 will increase remarkably the  $\eta_p$  from ~2.5% up to 22%. It is also noticed that at  $ZT_{avg}$  of 3.0 and  $\Delta T$  of 400K the  $\eta_p$  reaches ~26%, which is comparable to the power efficiency ( $\eta_{Carnot}$ ) of conventional heat engines. Thus, TE technology plays a remarkable role in many advanced scientific fields as its thermal energy source is not limited to a certain source instead it could be from solar energy, waste heat, fuels, radioisotopes, and geothermal energy [31]. For instance, the RTG has been used in the aerospace field for a long time since 1959 as a power source in space probes and satellites [32].

### 2.3.2 Thermoelectric Model of Active Refrigeration (Peltier Effect)

The reverse of the Seebeck effect is the Peltier effect, which represents the thermoelectric model of active refrigeration and it is stated by the French physicist Jean Peltier (Figure 2.3 (a)) in 1834 [33]. In this effect, the application of electric current on

the electrified junctions of 2 dissimilar TE materials will lead to either active cooling (e.g. freezing the water into ice) or heating (e.g. melting the ice into water) depending on the flow direction of the applied electric current within the circuit [33]. Thus, the flow of electric current in a similar direction to the heat flow will activate the cooling mode (heat is rejected); while its opposite flow to heat flow will activate the heating mode (heat is absorbed). For instance, the flow of electric current from the attached electric source such as a battery into the closed-circuit will lead to the heat absorption at the lower junction ( $T$ ) and heat rejection at the upper junction ( $T-\Delta T$ ); hence the active cooling will occur at the upper end as demonstrated in Figure 2.3 (b) [34]. This is due to the presence of an electric source that forced the heat flow to be from active cooling at the upper junction to the lower junction against the normal temperature gradient.

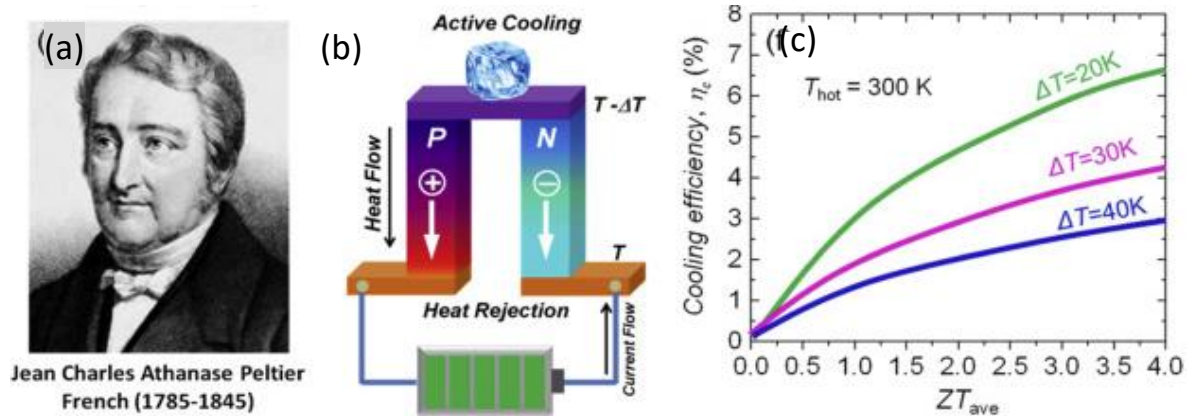


Figure 2.3 The French physicist Jean Peltier (a), the schematic representation for the thermoelectric model of active cooling (b), and the diagram of active cooling efficiency in terms of  $ZT_{avg}$  (c) [27].

The heat released (in cooling mode,  $-Q$ ) or absorbed (in heating mode,  $+Q$ ) is directly proportional to the flow of the applied electric current ( $I$ ) between the 2 junctions and its proportionality constant is termed as Peltier coefficient ( $\Pi$ ), as displayed in Equation (2.4) [35]. The negative value of  $\Pi$  indicates the cooling mode is on as the heat is released ( $-Q$ ), while the positive value of  $\Pi$  is for a heating mode where the heat is absorbed ( $+Q$ ) [35].

$$\Pi = \frac{Q}{I} \quad (2.4)$$

Additionally, the TE cooling/refrigeration efficiency ( $\eta_c$ ) or coefficient of performance (COP) is a function of similar parameters as power generating efficiency ( $\eta_p$ ) except that the  $\eta_{\text{Carnot}}$  will be reversed and replaced with the efficiency of typical refrigerator/heat pumps ( $\eta_{\text{refrigerator}} = T_c/T_h - T_c$ ), as shown in Equation (2.5) [36].

$$\eta_c = COP = \eta_{\text{refrigerator}} * \left[ \frac{\sqrt{1 + ZT_{\text{avg}}} - T_h/T_c}{\sqrt{1 + ZT_{\text{avg}}} + 1} \right] \quad (2.5)$$

It is also observed from Figure 2.3 (c) that the smaller the  $\Delta T$  between upper and lower junctions will increase  $ZT_{\text{avg}}$  and then raising the  $\eta_c$  in a similar manner to the  $\eta_p$ . For instance, lowering the  $\Delta T$  from 40K to 20K at  $T_h$  of 300K and  $ZT_{\text{avg}}$  of 2.0 will increase significantly the  $\eta_c$  from  $\sim 2.0\%$  up to 4.7%. It is also noticed that at  $ZT_{\text{avg}}$  of 3.0 and  $\Delta T$  of 20K the  $\eta_c$  reaches  $\sim 6\%$ , which is a remarkable cooling efficiency. Thus, the active cooling obtained via TE devices has been utilized in a set of electronic equipment, particularly for defense and military applications [37]. It has been also used widely in cooling computer components in order to maintain its temperature within the design limits for stable and optimum functioning [2]. Additionally, the TE Peltier coolers have been implemented in the applications of the optical fiber communication within a feedback loop in conjunction with a thermistor targeting to stabilize the



wavelength of the device via preserving a fixed temperature of its laser component, which is a thermal sensitive component [38].

## 2.4 Thermoelectrics: Device Module

The typical thermoelectric device is made up of numerous thermoelectric modules. Each thermoelectric module consists of: lower substrate usually based on ceramic material ( $\text{Al}_2\text{O}_3$ ) for electric insulation, lower metallic junctions as copper metal for electric conduction, many alternating legs of p-type and n-type TE elements, which have opposite concentrations in their majority charge carriers, another upper copper metallic junctions, and then the TE device will be enclosed with an upper ceramic substrate, as illustrated in Figure 2.4 (a) [39]. The device has also external electrical connections to carry out the generated electrical current from thermal energy conversion in TEGs or to input electric current for active heating and cooling applications. The alternating TE materials act as an array of thermocouples that are connected thermally in parallel and electrically in series, as demonstrated in Figure 2.4 (b) [40]. Thus, the heat flows in parallel through each TE leg, while the current flows sequentially along each leg.

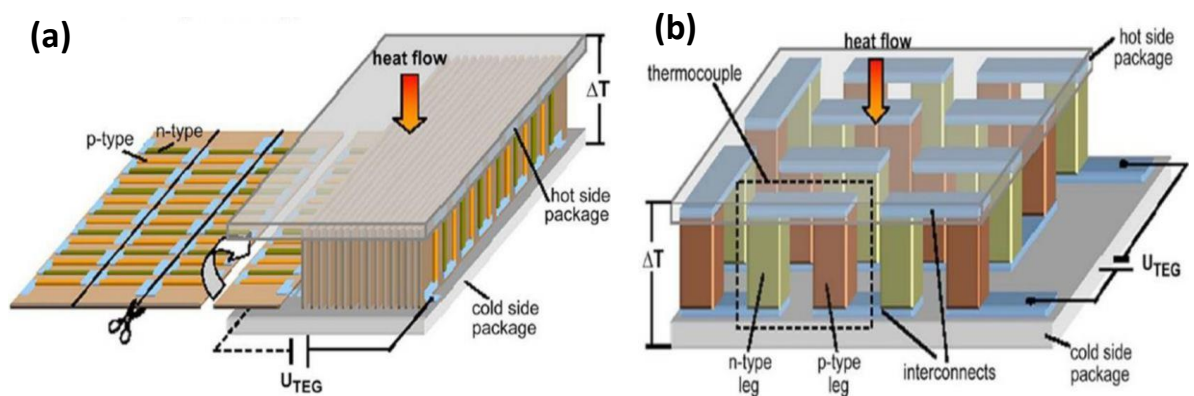


Figure 2.4 The Schematic representations of typical thermoelectric device modules (a) and it's alternating n-type and p-type thermoelectric materials connected electrically in

series and thermally in parallel (b) [39].

Moreover, the TE device modules generate current under subjection of temperature gradient ( $\Delta T$ ) along its TE legs via absorbing thermal energy on one of its sides to be the heat source and rejecting heat at the other side, which will be the heat sink. It is also worth mentioning that the use of alternating TE legs with opposite charge carriers (holes in p-type leg and electrons in the n-type leg) will maximize the amount of heat generated and absorbed via enlarging the difference in their Peltier coefficients ( $\Pi=Q/I$ ) [41]. Additionally, the connection of thermocouples in series will bring the Seebeck voltage ( $\Delta V$ ) of TE device to be closer to the voltage generated via electrochemical reactions on electrodes within typical DC power sources such as batteries [42]. Thus, the  $\Delta V$  of the TE device could be calculated based on Seebeck coefficients of n-type ( $S_n$ ) and p-type ( $S_p$ ) TE legs as shown in Equation (2.6) [43].

$$\Delta V = n \int_{T_c}^{T_h} (S_p - S_n) dT \quad (2.6)$$

On the other hand, the overall electrical resistance of TE device ( $R$ ) is a summation of electrical resistance from TE legs, metallic junctions, and their contact resistance as shown in Equation (2.7) [43].

$$R = n \left( \frac{\rho_n l}{A_n} + \frac{\rho_p l}{A_p} + R_l \right) \quad (2.7)$$

Where  $R$  is electrical resistance of TE device,  $n$  is total number of TE legs,  $\rho_n$  and  $\rho_p$  are the densities of single n-type and p-type TE leg,  $A_n$  and  $A_p$  are the cross-sectional areas of single n-type and p-type TE leg,  $l$  is the uniform length (i.e. height) of TE leg, and  $R_l$  is the summation of metallic junctions resistance and TE leg-junctions

contact resistance. Additionally, the overall thermal conductance of the TE device ( $K$ ) could be calculated in a similar manner to its overall resistance, as shown in Equation (2.8) [43].

$$K = n \left( \frac{K_n A_n}{l} + \frac{K_p A_p}{l} + K_l \right) \quad (2.8)$$

Where  $K$  is thermal conductivity of TE device,  $K_n$  and  $K_p$  are the thermal conductivities of single n-type and p-type TE leg, and  $K_l$  is the parallel thermal loss per  $n$  legs, which is related to thermal radiation, thermal conduction via surrounding gas molecules, or any other form of thermal losses. Consequently, the amount of heat produced or absorbed within the TE device ( $Q$ ) could be estimated using Equation (2.9), which is based on the summation of heat terms in Peltier, Joule, and Fourier laws [43].

$$Q = I \Delta V \Delta T - K \Delta T - 0.5 I^2 R \quad (2.9)$$

Where  $Q$  is heat absorbed/released within TE device,  $I$  is input/output current of TE device,  $\Delta V$  is the Seebeck voltage of TE device,  $K$  is thermal conductivity of TE device,  $R$  is electrical resistance of TE device, and  $\Delta T$  is the temperature gradient along its TE legs. On the other hand, the  $ZT$  of the TE device is analogous to the  $ZT_{\text{avg}}$  for TE legs and could be approximated using Equation (2.3). The TE device efficiency could be evaluated using either Equation (2.2) for TEG applications or Equation (2.5) for active cooling/heating applications.

Furthermore, the TE devices vary noticeably in their 3D architectures as they are capable to harvest or generate  $\Delta T$  in a perpendicular direction to the device plane, as demonstrated in Figure 2.5 [44]. Thus, TE modules fabrications require placing TE legs in a suitable 3D spatial resolution. It is experimentally proven that increasing the spatial resolution in depositing TE legs will, in turn, increase the number of possible TE legs that can be deposited in a given area [45]. This will maximize the Seebeck voltage and in turn, the generated current of TE device, which is desirable in a number

of applications including wearable electronics and vehicles [46]. Thus, the density of TE legs plays a crucial role in designing TE devices, particularly for heat harvesting applications with small  $\Delta T$  as its power generation will be controlled by the small formed  $\Delta V$  per TE legs [46].

However, the use of ink-based technologies such as inkjet printing or screen printing will provide enough spatial resolutions that will increase sufficiently the density of TE legs, which will establish high  $\Delta V$  per TE legs and increase the amount of generated current [47]. Such technologies could be utilized in optimizing the fabrication of conventional 3D architectures to form shape and size adaptable TE device that's suitable for wearable electronic applications, ring-shaped architectures for ultrahigh harvesting of released heat from fuel combustion at the exhaust pipe of vehicles, and planar-shaped architectures for folded and flexible TE device needed for optimum thermal contact to maximize the heat harvesting from buildings, as demonstrated clearly in Figure 2.5 [44].

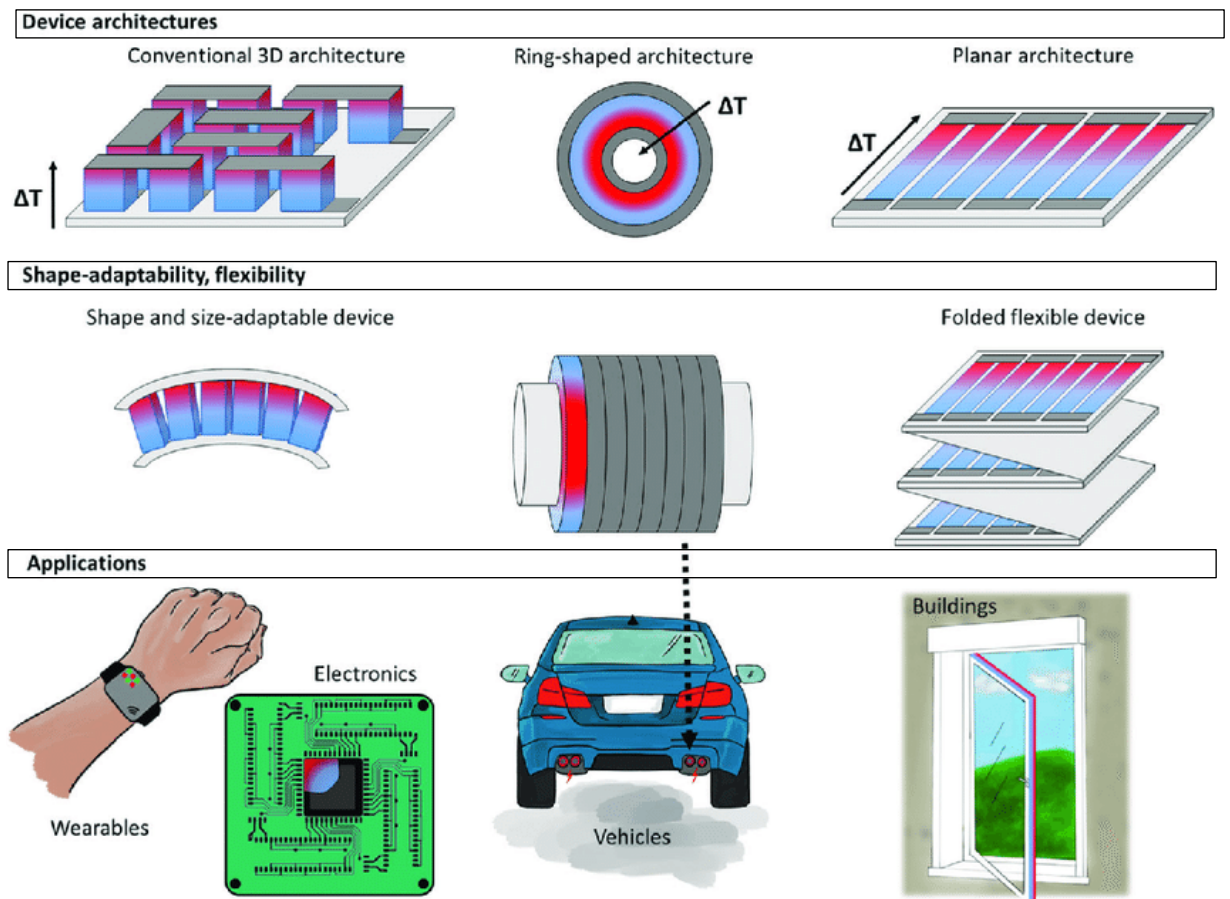


Figure 2.5 The Schematic representations of the most common architectures for thermoelectric device modules and examples on the applications that they can fit properly [44].

## 2.5 Thermoelectrics: Remarkable Properties

The high-performance thermoelectric devices depend on the use of advanced thermoelectric materials with a set of remarkable properties as discussed below to maximize the efficiency of energy conversion and power generation across the TE device.

### 2.5.1 Low Thermal Conductivity ( $k$ )

The thermal conductivity of TE materials depends on certain thermal transport processes that identify its ability to transfer heat. This conduction property is controlled

by the motion of charge carriers (holes and electrons) and phonons (vibrations of crystal lattice) across the solid TE material [48]. Thus, the thermal conductivity ( $k$ ) of TE materials includes the lattice phonon contribution ( $k_l$ ) which is dominant on electron contribution ( $k_e$ ) in semiconductors, as expressed in Equation (2.10) [49]. There are also other factors that contribute significantly in determining the thermal conductivity of TE materials such as crystal lattice defects, TE material size in the single crystal structure, TE material grains size in a polycrystalline structure, and interaction nature between charge carriers and lattice phonons [50].

$$k = (k_l + k_e) = \left( \frac{C_v * V * L}{3} \right) + (T * \sigma * L) \quad (2.10)$$

### **2.5.1.1 Lattice Phonon Thermal Conductivity ( $k_L$ )**

This dominant term of thermal conductivity in TE materials is governed by the phonon motion, which is analog to the continuous vibrations of their crystal lattice during heat flow in presence of a temperature gradient ( $\Delta T$ ) [51]. The phonon transport across TE materials depends mainly on the length of its mean free path, as shown in Equation (2.11) [51].

$$k_l = \frac{C_v * V * L}{3} \quad (2.11)$$

Where,  $k_l$  is the lattice phonon thermal conductivity,  $C_v$  is the heat capacity of TE material at a constant volume,  $V$  is the average sound velocity of phonons,  $L$  is the phonon mean free path before scattering, which is typically in the range of 10 $\mu$ m to 1nm [52]. Thus, the amorphous materials as glass have been frequently reported with the lowest  $k_l$  owing to the slowest phonon motion across their non-crystalline (random and disordered) structure [53]. However, minimizing  $k_l$  in the crystalline materials is restricted by the interatomic distances between their atoms [53]. Consequently, the common effective strategies adopted to lower  $k_l$  in crystalline materials are based on

utilizing the phonon scattering mechanisms at either bulk scale or nanoscale, as illustrated clearly in Figure 2.6 [54,55]. Thus, the dominant strategy that is commonly adopted in minimizing  $k_l$  is via introducing scattering agents such as imperfections, impurities, or a large number of grain boundaries to the crystal structure of TE material in order to shorten the phonon mean free path ( $L$ ) and then maximizing its scattering, hence lowering  $k_l$ .

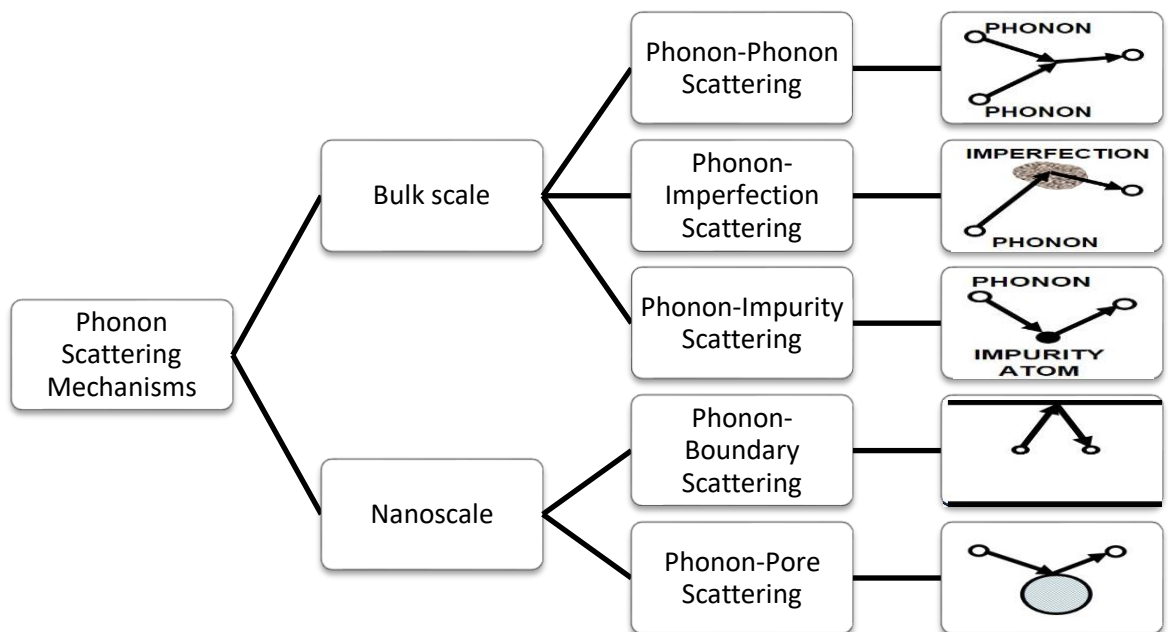


Figure 2.6 The Flow chart of the common effective phonon scattering mechanisms for bulk scale and nanoscale thermoelectric materials [54,55].

Additionally, the crystalline solid materials are frequently reported with low sound velocity ( $V$ ), which matches the ideal behavior of TE materials in undergoing the “phonon-glass electron-crystal” phenomenon [56]. This is proven in TE materials with intrinsic ultra-low  $k_l$  due to their large molecular weight ( $MW$ ) (i.e. having

constituents' elements with heavy atomic masses), weak chemical bonds, lattice distortion (i.e. imperfections), or complex crystal structure [57].

### **2.5.1.2 Electronic Thermal Conductivity ( $k_e$ )**

This less effective term on thermal conductivity of TE materials is related to the motion of the electric charge carriers, which contributes to both electrical and thermal conductivities. The proportionality relation between electrical conductivity ( $\sigma$ ) and thermal conductivity ( $k_e$ ) of the electric charge carriers is identified by Wiedemann-Franz law, as shown in Equation (2.12) [58].

$$k_e = T * \sigma * L \quad (2.12)$$

Where  $k_e$  is the electronic thermal conductivity,  $T$  is the absolute temperature,  $\sigma$  is the electronic electrical conductivity,  $L$  is the Lorenz number, which ranges between 1.50 and  $2.44 * 10^{-8} \text{ W} \cdot \Omega \cdot \text{K}^{-2}$  for non-degenerated and strongly degenerated semiconductors, respectively [58]. These semiconductors vary mainly in their level of doping, which will influence their electrical properties. For instance, the strongly degenerated semiconductors have a higher level of doping, significant interactions between dopant atoms and host lattice, and then the formation of donor or acceptor bands other than discrete energy levels as in non-degenerated semiconductors [59]. This alters their electrical properties to be close to that for metallic materials than semiconductors. Whereas, the non-degenerated semiconductors have moderate doping levels resulting in negligible interactions between dopant atoms and host lattice, hence forming discrete energy levels with low electrical conductivity [59].

Additionally, at absolute temperatures ( $T$ ) lower than room temperature, the bipolar diffusion term ( $k_{bi}$ ) has to be added to Equation (2.12) in order to involve the occurrence of electron-hole pair recombination process at the cold side of TE material after their thermal separation at its hot side. This term has negligible value in non-



degenerated systems (i.e. intrinsic/non-doped semiconductors) in which all charge carriers (electrons and holes) have equal concentrations and mobilities [60]. Whereas, it has a noticeable value in the degenerated systems (i.e. doped semiconductors) due to the wide difference in charge carriers concentrations resulting in the majority (high concentration charge carriers) and minority (low concentration charge carriers) carriers [60]. In such systems, the  $k_{bi}$  term will be governed by the mobility of minority charge carriers. Thus, the bipolar contribution in TE materials, which are mainly a class of degenerated systems could be nulled via minimizing the mobility of minority charge carriers (electrons in p-type TE and holes in n-type TE) [60]. This could be attained either via increasing the bandgap to rise their scattering or decreasing their effective mass to reduce their mobility [61].

However, the high-performance TE devices depend on advanced TE materials with a low thermal conductivity, which is commonly accomplished via minimizing the lattice phonon thermal conductivity through adopting a set of phonons scattering mechanisms, while maintaining its electronic thermal conductivity to avoid lowering its electrical conductivity. Thus, the ideal TE materials undergo phonon-glass behavior in their lattice thermal conductivity (minimizing its effect), while electron-crystal behavior in their electrical conductivity (maximizing its effect).

### **2.5.2 High Electrical Conductivity ( $\sigma$ )**

The electrical conductivity of TE materials depends mainly on its: Seebeck coefficient, electrical mobility, and resistivity, which identify its ability to transfer the electric charge, hence the flow of electric current [62]. This conduction property of TE material is affected by its crystal structure, temperature gradient, and scattering mechanisms of charge carriers (e.g. imperfections and impurities) [62].

### 2.5.2.1 Seebeck Coefficient ( $S$ )

This coefficient quantifies the magnitude of generated Seebeck voltage ( $\Delta V$ ) due to the presence of temperature gradient ( $\Delta T$ ) across TE material, as pre-shown in Equation (2.1). It also qualitatively defines the strength of the interaction between the heat flow and electrical current along TE material via accounting two important contributions, namely: electric charge carriers diffusive Seebeck coefficient ( $S_d$ ) and lattice phonon drag Seebeck coefficient ( $S_g$ ), as displayed in Equation (2.13) [63].

$$S = (S_d + S_g) \quad (2.13)$$

#### 2.5.2.1.1 Charge Carriers Diffusive Seebeck Coefficient ( $S_d$ )

This term of the overall Seebeck coefficient ( $S$ ) arises from the variation in diffusion rates of electric charge carriers (holes and electrons) at the applied temperature gradient ( $\Delta T$ ) across TE material [63]. The charge carriers will absorb thermal energy at the hot side (high energy regime), which will accelerate them to diffuse in different rates to the cold side (low energy regime) of TE material. The diffusion direction of electric charge carriers is in a parallel direction to the heat flow, hence indicating the presence of an interaction between them. Thus, an electric potential difference (i.e. Seebeck voltage ( $\Delta V$ )) will be build up between the two ends due to the diverse in diffusion rates of charge carriers along TE materials (p-type TE and N-type TE) leaving behind the opposite charge carriers [64].

However, this build-up voltage due to charges separation will limit the transfer of remained electric charges at the hot side to the cold side. Consequently, some of the electric charge carriers will be drifted back to the hot side in parallel direction to the formed electric field. This will result in the simultaneous presence of two opposite processes, which are the direct motions of charges from hot-to-cold sides in parallel to the applied  $\Delta T$  and the reverse motions of charges from cold-to-hot sides in parallel to

the formed electric field. Thus, the net current will be produced only if one of the processes is dominant among the other one [65]. Accordingly, the  $S_d$  could be enhanced via using degenerated TE materials as they are heavily doped materials with an excess amount of majority charge carriers, hence higher  $S$  and improved electrical conductivity. It is also worth mentioning that the sign of  $S$  indicates the type of doped TE material (i.e. negative  $S$  is n-type TE and positive  $S$  is p-type TE).

#### **2.5.2.1.2 Lattice Phonon Drag Seebeck Coefficient ( $S_g$ )**

This component of the overall Seebeck coefficient ( $S$ ) indicates the drag effect of lattice phonon on the electric charges movements [66]. This disturbs effect arises from the excitation of phonon at high temperatures to transfer heat but not carrying electric charges. During their transfer from hot-to-cold sides, they significantly interact with the flowing charge carriers in the same path (i.e. from hot-to-cold sides). This interaction will disturb charges movements and scatter them to the other end of the TE material. However, the phonon drag component disappears at temperatures above room temperature as it is a temperature-dependent parameter, while it is dominant at temperatures below room temperature, as shown in Equation (2.14) [66].

$$\theta_D \approx 5 * T \quad (2.14)$$

Where  $\theta_D$  is the Debye temperature at which the high-frequency phonons will be excited, and  $T$  is the absolute average temperature at which the TE material is operating. Additionally, the charge carrier concentration has an inverse proportionality with the phonon drag component, as noticed from Equation (2.15) [66].

$$S_g = - \frac{C_l}{3 * e * n} \quad (2.15)$$

Where  $S_g$  is the phonon drag component of the Seebeck coefficient,  $C_l$  is the specific heat of TE lattice,  $e$  is the electric charge, and  $n$  is charge carriers concentration. Thus,  $S_g$  has negligible value in case of heavily doped TE materials and operating at

high temperatures above the room temperature, as observed from Equations (2.14) and (2.15).

### 2.5.2.2 *Electrical Mobility & Resistivity*

In a similar manner to the Seebeck coefficient (S), the electrical mobility ( $\mu$ ) and resistivity ( $\rho$ ) of TE material quantify its electrical conductivity ( $\sigma$ ). The electrical resistivity is an intrinsic property of the material and it indicates its ability to slow down the flow of charge carriers via increasing their rate of scattering, hence lowering its electrical conductivity [67]. Thus, the electrical resistivity depends on the type of material (i.e. metallic, semiconductor, or non-metallic materials), microstructure, imperfections, diffusion rates, and operating conditions, particularly temperature [67]. For instance, TE materials are typical semiconductors and then their electrical resistivity will be governed by charge carriers mobility (i.e. mean free path to flow) and concentration, as noticed from Equation (2.16) [67].

$$\rho = \frac{1}{\sigma} = \frac{1}{q(n * \mu_n + p * \mu_p)} \quad (2.16)$$

Where,  $\rho$  is the electrical resistivity of TE material,  $\sigma$  is the electrical conductivity of TE material,  $q$  is the electric charge ( $1.6 * 10^{-19}C$ ),  $n$  and  $p$  are the concentrations of negative charge carriers (electrons) and positive charge carriers (holes),  $\mu_n$  and  $\mu_p$  are the mobility of negative and positive charge carriers, respectively. This equation can be reduced to a single term in the case of the heavily degenerated semiconductors (i.e. heavily doped semiconductors) such as TE materials [68]. For instance, in the p-type TE material the majority of charge carriers are positive holes (i.e. concentration  $p \gg n$ ) and then the minority charge carriers' term for negative electrons could be canceled (i.e.  $\rho \approx 1/q * p * \mu_p$ ). Additionally, the mobility of electric charges is sensitive to the temperature and presence of their scattering mechanisms such as imperfections, impurities, and lattice vibrations (phonons) [68]. Thus, the increase in

temperature will excite phonons to interact with the flow of charge carriers and then scattering them, hence reducing their mobility and lowering the electrical conductivity of TE material. Also, the presence of impurities and defects will scatter more the moving charge carriers, hence raising the electrical resistivity of TE material as repeatedly reported [68]. Thus, the efficient TE materials are frequently reported with high electrical conductivity due to their high Seebeck coefficient and charge carriers mobility [69].

### **2.5.3 High Power Factor (PF)**

The TE materials with a high power factor (PF) show the highest thermoelectric energy conversion efficiency due to the significant increment in their Figure-of-Merit (ZT). This factor indicates the power of energy conversion between thermal and electrical energies and then it depends on the Seebeck coefficient (S) and electrical conductivity ( $\sigma$ ) of TE material as shown in Equation (2.17) [70].

$$PF = S^2 * \sigma \quad (2.17)$$

The high PF values point to an increase in both the Seebeck voltage and generated current during the power generation process; hence it is the key parameter to attain high-performance TE devices. Consequently, there are various PF enhancement approaches, which principally focus on utilizing nanotechnology to produce nanoscale and complex TE structures in order to increase the number of the contributing phonon scattering mechanisms [71]. This will lower extensively the thermal conductivity of TE materials, particularly the lattice phonon thermal conductivity ( $k_l$ ). Thus, it is frequently reported that improving PF is a feasible and indispensable approach to eventually attain the desirable high ZT values [72].

Additionally, this effective and innovative approach is based on the quantum confinement effect, which was emphasized on its significances in 1993 by Hicks and

Dresselhaus in their landmark published theory paper as pre-discussed in section (2.1). Thus, its effectiveness is referred to the sharp and asymmetric density of state (DOS) nearby the Fermi level (EF) within nanoscale (low-dimensional) TE materials including quantum wells (2D), quantum wires (1D), and quantum dots (0D) [73]. However, these quantum structures have been challenging as their structures must be in the nanoscale ( $\leq 10^{-9}\text{m}$ ) and EF must be located at the proper position to return in both high S and PF, as repeatedly reported [73]. There are also many other effective and advance approaches that can be utilized to maximize the PF and then ZT of TE materials, which will be further discussed in section (2.7).

#### **2.5.4 High Figure-of-Merit (ZT)**

The energy conversion efficiency of TE materials is dependent on their physical transport properties, which could be monitored through the dimensionless Figure-of-Merit (ZT). This dimensionless parameter is dependent on their electrical conductivity ( $\sigma$ ), Seebeck coefficient (S), absolute temperature (T) at which these physical properties are measured, and thermal conductivity (k) that includes phonon contribution ( $k_l$ ), which is dominant on electron contribution ( $k_e$ ) in semiconductors, as shown in Equation (2.18) [74].

$$ZT = \frac{PF * T}{k} = \frac{S^2 * \sigma * T}{(k_l + k_e)} \quad (2.18)$$

It's obvious from this equation that an efficient TE material is the one that will record the highest electrical conductivity, highest Seebeck coefficient, and lowest thermal conductivity. It is also proven that there is a strong interdependence between these three thermoelectric parameters, which means that adjusting one of them will lead to a detrimental effect on others, as observed from Equations (2.10), (2.19), and (2.20) [75].

$$\sigma = n * e * \mu = n * e^2 * \frac{\tau}{m^*} \quad (2.19)$$

$$S = A * T * \left( \frac{m^*}{n^{\frac{3}{2}}} \right) = \left( \frac{8 * \pi^2 k_B^2}{3 * e * h^2} \right) * T * \left( \frac{m^*}{n^{\frac{3}{2}}} \right) \quad (2.20)$$

Where,  $\sigma$  is the electrical conductivity of TE material,  $n$  is charge carriers concentration,  $e$  is the electric charge of an electron,  $\mu$  is the mobility of charge carriers,  $\tau$  is the relaxation time,  $m^*$  is the charge carriers effective mass (near EF), which depend on band structure of TE material,  $S$  is the Seebeck coefficient of TE material,  $A$  is a constant,  $k_B$  is Boltzmann constant, and  $h$  is Plank constant [75]. Consequently, the main challenge is to tune these properties in an appropriate manner to have a significant design that will improve the TE performance through maximizing ZT.

In other words, to generate high electric power the  $S$  and  $\sigma$  should be high (i.e. high PF), which favors low  $k$  to maintain the  $\Delta T$  across TE legs (i.e. hot and cold ends per each TE leg within TE device). Thus, several effective and advanced approaches could be adopted to attain the desirable high ZT as demonstrated in section (2.7). For instance, the band engineering approach could be used to optimize the carriers concentration within TE material and then enhancing its PF, while the nanostructuring approach could be implemented to increase phonon scattering and then minimizing  $k_l$ , which is the only independent physical property of TE materials [75].

### 2.5.5 High Thermoelectric Efficiency ( $\eta_p$ or $\eta_c$ )

The efficiency of thermoelectric energy conversion depends mainly on the average ZT of TE legs within the TE device module as observed from Equations (2.2) and (2.5). Thus, maximizing  $ZT_{avg}$  will in return improve the TE conversion efficiency of either power generation ( $\eta_p$ ) or cooling/refrigeration ( $\eta_c$ ) models, as pre-discussed in detail in sections (2.3.1) and (2.3.2). Consequently, overcoming the typical Carnot efficiency of heat engines ( $\eta_{Carnot}$ ) and refrigerator/heat pump efficiency ( $\eta_{Refrigerator}$ ) for

TEGs and TE cooling/heating devices, respectively.

### **2.5.6 High Nanostructuring Thermal Stability**

The high thermal stability of nanostructured TE materials is a crucial optimizing property in order to maintain the performance of TE device, prevent its failure, and extends its life cycle for reliable service through the use of a stabilizer (e.g. Thioglycolic Acid (TGA)), proper sintering technique, or post-annealing heat treatment [76]. The stabilization of TE nanostructures will prevent the growth of nanocrystals under continuous exposure to high thermal stresses during TE device operation through relieving significantly their lattice strain [76]. Additionally, the Spark Plasma Sintering (SPS) technique could assist in the stabilization of synthesized nanopowders through the use of an electric spark that will result in the formation of more defects and evaporation of elements, which will significantly modify TE properties of the final product as frequently reported [77].

## **2.6 Thermoelectrics: Promising Materials Systems**

The interdependence of the three main physical properties ( $k$ ,  $\sigma$ , and  $S$ ), which identifies the performance of TE devices (i.e.  $ZT$ ) has limited the selection of suitable materials for TE applications. Also, their dependence on the free carrier concentration ( $n$ ) has resulted in difficulties in tuning them independently, as noticed in Figure 2.7 [78]. This figure shows clearly the exponential decrease in  $S$  (i.e.  $S$  proportional to  $-\ln n$ ) and linear increase in  $\sigma$  (i.e.  $\sigma$  proportional to  $n$ ) as the carrier concentration increases. Thus, there is an optimum value of  $n$  at around  $10^{19}$  and  $10^{20}\text{cm}^{-3}$  to maximize the PF (i.e.  $S^2\sigma$ ) for optimum  $ZT$ . These  $n$  values correspond to the typical  $n$  for degenerated semiconductors. Thus, the  $\sigma$  could be maximized further via utilization of the state-of-the-art TE semiconducting materials with outstanding carriers' mobilities.



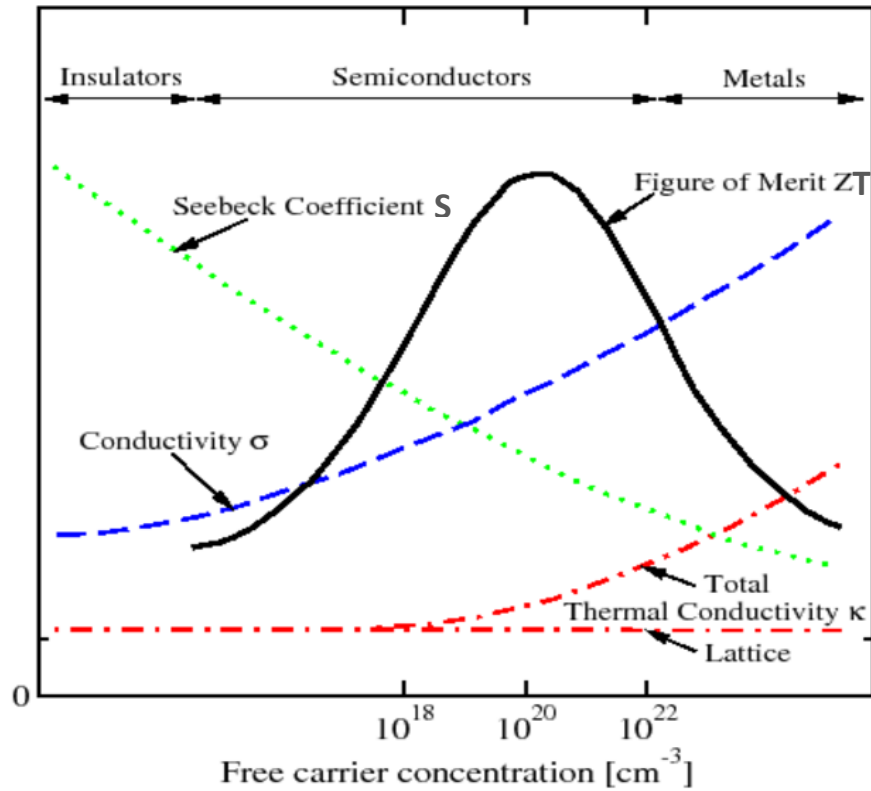


Figure 2.7 The Thermoelectric properties in terms of free carrier concentrations for the main classes of materials [78].

Additionally, it is proven frequently that there is no single material existing in nature, which possesses good TE properties [79]. This arises one of the major challenges in the TE field, which is the development of various materials to show low  $k$ , while high  $\sigma$  and  $S$  targeting to obtain the desired high  $ZT$  values. For instance, metals are good electrical and thermal conductors resulting in high  $\sigma$  and  $k$ , while low  $S$  due to their high carriers' concentration (i.e.  $>10^{22}\text{cm}^{-3}$ ), hence lower PF and  $ZT$  based on Equations (2.17) and (2.18), respectively. In contrast, the insulators are poor electrical and thermal conductors, which lead to low  $\sigma$ ,  $k$ , PF, and then  $ZT$ . Thus, it is proven that semiconductors are the ideal TE candidates as they show relatively lower  $k$ , higher  $\sigma$ , and  $S$ , hence optimum  $ZT$  values, as illustrated in Figure 2.7 [78]. Accordingly, the

promising TE systems are based classically on degenerated semiconductors with lattice thermal conductivity ( $k_l$ ) dominant on electron thermal conductivity ( $k_e$ ) [80].

Furthermore, the modern TE materials are typically semiconductors and then their electrical conductivity ( $\sigma$ ) is a temperature-dependent [80]. For instance, at high temperatures, more charge carriers will be excited to overcome the energy barrier (i.e. energy gap ( $E_g$ )) and flow from the valence band (VB) to the conduction band (CB) [81]. Thus, the CB will be occupied by the excited electrons, while the VB will have both the left-behind electrons in the vacant orbitals and the formed holes, all of which will contribute to the overall  $\sigma$  of the semiconductor as illustrated in Figure (2.8) [81].

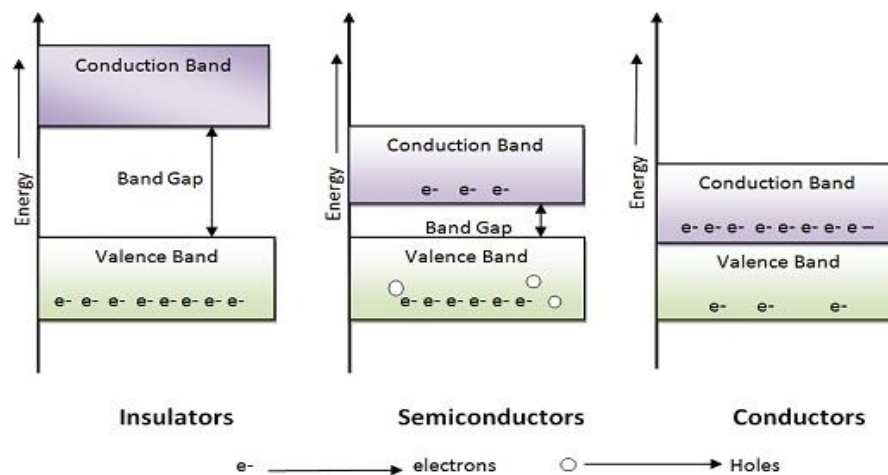


Figure 2.8 The Schematics of energy-band diagrams for insulators, semiconductors, and conductors [81].

Consequently, the promising TE systems that have been used for commercial applications could be classified into three main categories based on their TE performance at certain temperature ranges namely:  $\text{Bi}_2\text{Te}_3$ -based TE systems for TE

applications of low-temperatures ( $<400\text{K}$ ), PbTe-based TE systems for TE applications of moderate-temperatures ( $400\text{-}800\text{K}$ ), and  $\text{Si}_{1-x}\text{Ge}_x$ -based TE systems for TE applications of high-temperatures ( $>800\text{K}$ ), as clearly demonstrated in Figure 2.9 [82]. These classes of TE materials could be used in either their p-type or n-type based on the type of doping, which will result in obvious differences in their ZT values, as observed from Figure 2.9 (a) and (b), respectively. For instance,  $\text{Bi}_2\text{Te}_3$ -based TE systems show optimum ZT values in the p-type in which it exceeds the unity ( $ZT=1$ ), while in the n-type it is below the unity. Additionally, the  $\text{Bi}_2\text{Te}_3$  system shows the highest TE performance at RT and then it is used extensively in Peltier coolers, which have been commercialized several decades ago [83]. Whereas the PbTe system shows optimum TE performance between  $400\text{K}$  and  $800\text{K}$ , hence it has been utilized mainly for TEGs operating at high temperatures. The  $\text{Si}_{1-x}\text{Ge}_x$  system, which is based on a solid solution of Si and Ge to reduce effectively their  $k_l$  and maximize ZT at temperatures above  $800\text{K}$  to act as an efficient electricity source, particularly in spacecraft [84].

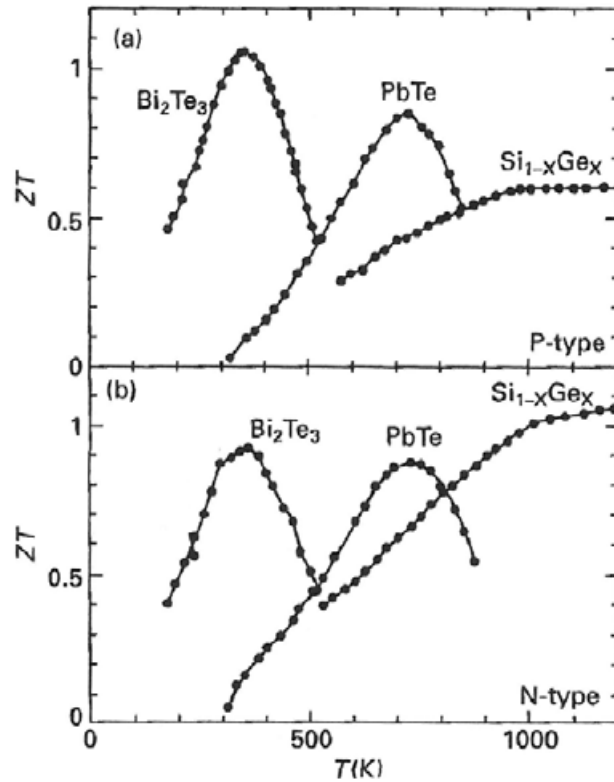


Figure 2.9 The Figure-of-merit ( $ZT$ ) in terms of the absolute temperature for the promising TE systems in both p-type (a) and n-type (b) [82].

### 2.6.1 Promising P-type $\text{Bi}_2\text{Te}_3$ -Based TE Systems ( $\text{Bi}_{2-x}\text{Sb}_x\text{Te}_3$ )

The  $\text{Bi}_2\text{Te}_3$ -based TE material and its alloys have been studied extensively since the 1950s due to their proven potentials as the ideal TE systems for low-temperature applications (near  $\text{RT} \approx 298\text{K}$ ), particularly for TE refrigeration and TEGs when their heat source is of low-temperatures ( $< 400\text{K}$ ) [85]. This is due to the narrowing in their bandgap as the operating temperature exceeds the RT resulting in VB and CB overlaps. This will mix the majority and minority conduction leading to high carriers' concentrations of both negative electrons and positive holes, hence lowering  $\mu$  and  $S$ , which matches the pre-observations from Figure 2.9. This undesired intrinsic thermal excitation has limited its application for waste heat recovery (WHR) at elevated

temperatures. Thus, their small band gap will degrade remarkably their PF and then ZT at temperatures either  $<200\text{K}$  or  $>400\text{K}$  to drop from 1.0 to 0.5 in both cases, as noticed from Figure 2.9 (a). However,  $\text{Bi}_2\text{Te}_3$ -based materials are still the dominant TE systems for TE applications of low-temperatures (200-400K).

Additionally, the  $k$  of  $\text{Bi}_2\text{Te}_3$  is considerably lowered via alloying it either with Antimony Telluride ( $\text{Sb}_2\text{Te}_3$ ) or Bismuth Selenium ( $\text{Bi}_2\text{Se}_3$ ), hence forming the p-type ( $\text{Bi}_{2-x}\text{Sb}_x\text{Te}_3$ ) and n-type ( $\text{Bi}_2\text{Te}_{3-x}\text{Se}_x$ ) doped Bismuth Telluride alloys, respectively [86]. Therefore, optimizing the alloying compositions ( $x$ ) of constituent elements and the carrier concentration within  $\text{Bi}_2\text{Te}_3$  alloys have resulted in maximizing their ZT to above 1.0 at RT [86]. It is also reported that the ZT value of this conventional TE system has been raised from the unity to  $\sim 2.4$  at 300K with further utilization of nanotechnology in nanostructuring the  $\text{Bi}_2\text{Te}_3$  alloys [87]. This is due to the significant reduction in their  $k_1$  while maintaining their  $\mu$  and PF.

Moreover, the ZT enhancements for p-type BiSbTe is much easier than n-type BiSeTe due to the strong texture and high anisotropic properties of n-type as frequently reported [88]. Thus, the Bismuth Antimony Telluride ( $\text{Bi}_{2-x}\text{Sb}_x\text{Te}_3$ ) has proven repeatedly its outstanding TE properties near room temperature till 375K and particularly  $\text{Bi}_{0.4}\text{Sb}_{1.6}\text{Te}_3$ , as illustrated in Figure 2.10 [89]. This figure proves the crucial effect of controlling the alloying composition ( $x$ ) on the ZT values for ternary  $\text{Bi}_{2-x}\text{Sb}_x\text{Te}_3$ . Thus, it clearly shows that a maximum ZT value of  $\sim 0.51$  has been achieved with  $x=0.4$  for  $\text{Bi}_{0.4}\text{Sb}_{1.6}\text{Te}_3$  alloy at  $\sim 375\text{K}$ . It is also reported with high thermoelectric conversion efficiencies up to 7.5% [90]. Thus, it has a high potential for further optimization of its TE performance, which matches the target of current researches.

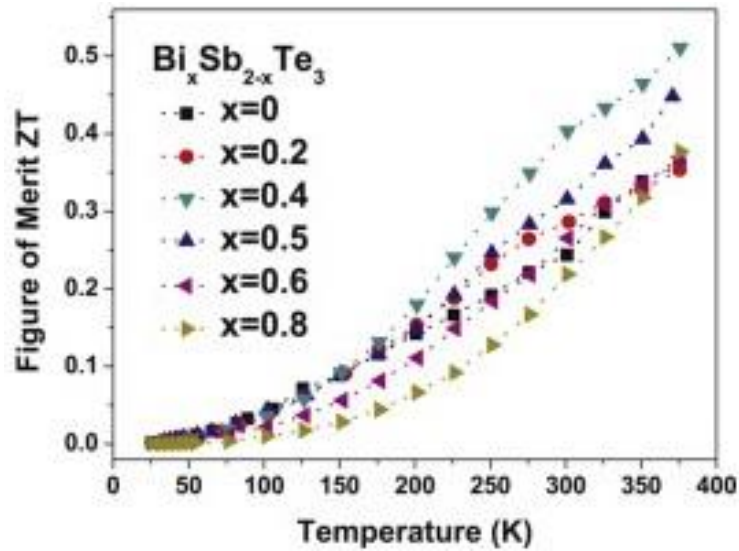


Figure 2.10 The Figure-of-merit ( $ZT$ ) in terms of the absolute temperature for the p-type  $\text{Bi}_x\text{Sb}_{2-x}\text{Te}_3$  in different alloying compositions ( $x$ ) [89].

Accordingly, it is characterized as a layered semiconductor with an indirect and narrow bandgap ( $E_g$ ) of  $\sim 160\text{meV}$ . It has a trigonal unit cell with lattice constants of  $c \approx 30.36\text{\AA}$  and  $a \approx 4.38\text{\AA}$ , as illustrated in Figure 2.11 [91]. The atomic layers of its constituents' elements forms numerous quintuple layers of  $\text{Te1-Sb(Bi)-Te2-Sb(Bi)-Te1}$  along the  $c$ -direction in  $\sim 1\text{nm}$  thickness, as displayed in Figure 2.11. This figure also shows the weak Van der Waals forces coupling these quintuple layers along the  $c$ -direction, while strong couplings of the ionic-covalent bond between  $\text{Sb(Bi)-Te1}$  and covalent bond between  $\text{Sb(Bi)-Te2}$ . Thus, in the crystal structure of  $\text{Bi}_{0.4}\text{Sb}_{1.6}\text{Te}_3$  the Bi atoms occupy quarter of Sb sites and its preferential orientations for optimum electrical transport properties (i.e. high  $\mu$  and  $\sigma$ ) is reported along the crystallographic planes of (0001), (10110), and (0115) with tilt angles of around  $0^\circ$ ,  $33^\circ$ , and  $54^\circ$  to  $ab$ -plane, respectively [92]. Accordingly, it is frequently reported with anisotropic TE properties that are optimum (high  $ZT$  values) along the perpendicular plane to  $c$ -axis [93].

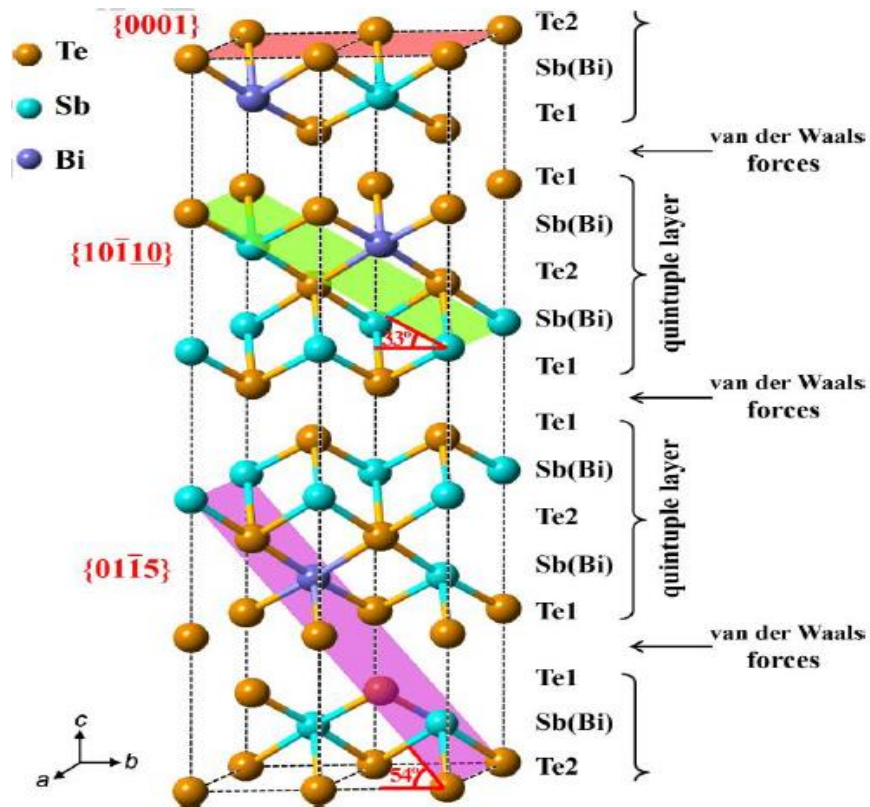


Figure 2.11 The Rhombohedral and quintuple layered crystal structure of promising  $\text{Bi}_{0.4}\text{Sb}_{1.6}\text{Te}_3$  system for TE applications of low-temperatures [91].

However, the structure of  $\text{Bi}_{0.4}\text{Sb}_{1.6}\text{Te}_3$  alloy is destroyed at elevated temperatures due to occurrences of the chemical decomposition, which will increase the possibility of tellurium vaporization [94]. Thus, the Te usage is governed by its melting temperature of  $\sim 722.66\text{K}$ . Also, the melting temperatures of its constituents' elements participate in limiting its utilization to only TE applications of low temperatures, as noticed from Table 2.1. Additionally, this table highlights significantly on the atomic dimensions and crystal structure, as well as, the physical, thermal, electrical, and mechanical properties of Bi, Sb, and Te elements, which builds up the crystal structure and identifies the TE performance of  $\text{Bi}_{2-x}\text{Sb}_x\text{Te}_3$  alloys. These

elemental properties need to be taken into consideration for its extreme optimization towards the desirable ZT values for practical TE applications. For instance, the heavy Bi and Te have very low sound velocities of 1790m/s and 2610m/s, respectively. This justifies the ideal TE behavior of Bi<sub>2</sub>Te<sub>3</sub>-based TE systems in undergoing the “phonon-glass electron-crystal” phenomenon for lowest  $k_1$ , hence the commercialization of Bi<sub>2-x</sub>Sb<sub>x</sub>Te<sub>3</sub> at RT [95].

Table 2.1 The Summary of the Atomic Dimensions and Crystal Structure, Physical Properties, Thermal Properties, Electrical Properties, and Mechanical Properties of Constituents’ Elements for Bi<sub>2-x</sub>Sb<sub>x</sub>Te<sub>3</sub> TE Material [96]

Bi <sub>2-x</sub> Sb <sub>x</sub> Te <sub>3</sub> Constituents’ Elements				
Property		Bismuth Bi	Antimony Sb	Tellurium Te
Atomic Dimensions & Crystal Structure				
Atomic radius	pm	143	133	123
Covalent radius	pm	148	139	138
Van der Waals radius	pm	N/A	N/A	206
Crystal structure	-	Base-centered	Simple	Simple
		Monoclinic	Trigonal	Trigonal
Lattice angles	°	$\pi/2, 1.926, \pi/2$	$\pi/2, \pi/2, 2\pi/3$	$\pi/2, \pi/2, 2\pi/3$
Lattice constants	pm	667.4, 611.7,	430.7, 430.7,	445.7, 445.7,
		330.4	1127.3	592.9
Lifetime	*10 <sup>19</sup> y	2.759	Stable	Stable
Physical Properties				
Series	-	Poor metal	Metalloid	Chalcogen



Phase	-	Solid	Solid	Solid
Color	-	Gray	Silver	Silver
Density	g/cm <sup>3</sup>	9.780	6.697	6.240
Speed of sound	m/s	1790	3420	2610
<b>Bi<sub>2-x</sub>Sb<sub>x</sub>Te<sub>3</sub> Constituents' Elements</b>				
Property		Bismuth Bi	Antimony Sb	Tellurium Te
<b>Thermal Properties</b>				
Melting point	K	544.40	903.78	722.66
Specific heat	J/kg.K	122	207	201
Thermal conductivity	W/m.K	8	24	3
<b>Electrical Properties</b>				
Electrical type	-	Conductor	Conductor	Semiconductor
Electrical conductivity	S/m	770,000	2,500,000	10,000
<b>Mechanical Properties</b>				
Brinell hardness	MPa	94.2	294	180
Mohs hardness	-	2.25	3.00	2.25
Bulk modulus	GPa	31	42	64
Shear modulus	GPa	12	20	16
Young's modulus	GPa	32	55	43

## 2.7 Thermoelectrics: Advancing Approaches

The pre-discussed promising TE systems need further enhancement of their TE properties ( $S$ ,  $\sigma$ , and  $k$ ) for higher TE energy conversion efficiency to overcome the benchmark value of  $ZT=1.0$  towards practical and commercial TE devices. This could be accomplished via adopting a set of novel advancing approaches of TE materials that depend either on phonon transport engineering to reduce  $k_l$  via strengthening phonon scattering mechanisms or charge transport engineering to

enhance PF via optimizing electron transport processes, as illustrated in below sections.

## **2.7.1 Phonon Transport Engineering**

### **2.7.1.1 Atomic Doping/Alloying**

The Russian physicist Lofe was the first one to adopt this approach to lowers the  $k_l$  of semiconducting TE materials via introducing point defects to their crystal structure for modifying their structural, mechanical, and electrical properties [97]. This pioneer engineering work has proven the efficient TE performance of alloyed/doped bulk TE materials with optimal alloying/doping compositions. Thus, the wise varying of the doping/alloying compositions in such extrinsic semiconductors will disturb efficiently their phonons transport for lower  $k_l$ , while improving their electrons transport for higher  $\sigma$ . This is attained via tuning set of critical TE parameters within the formed solid solution alloy including effective mass, carrier concentration, bandgap, and deformation potential [97].

For instance, the doping of  $\text{Bi}_2\text{Te}_3$ -based alloys with Sb will benefit in overcoming their TE performance degradation at prolonged thermal stresses or high temperatures ( $>400\text{K}$ ) [98]. This degradation in their TE performance is often referred to their intrinsically very small  $E_g$  of  $\sim 130\text{meV}$  [98]. This makes the detrimental thermal excitation of minority charge carriers easier and results in the occurrences of undesired bipolar effect, hence lowering  $S$ , rising  $k_e$ , and then lowering  $ZT$ . Thus, the utilization of such an advancing approach is crucial in broadening the  $E_g$  of  $\text{Bi}_2\text{Te}_3$ -based alloys to upshift their operating temperature, thermal stability, and service life [98]. The Sb doping is also favorable for high  $ZT$  values in  $\text{Bi}_2\text{Te}_3$ -based alloys as they act as strong point defects to improve the charge carrier concentrations (i.e. high  $\sigma$ ) and heat carriers scattering (i.e. phonons for low  $k_l$ ) [99].

However, the Sb doping is limited to an optimal value to avoid the high

positive charge carriers concentration (holes) due to the reduced formation energy of antisite defects, hence lowering  $S$  and rising  $k_e$  [99]. Additionally, it is frequently reported that the extrinsic point defects arise from Sb doping have modified the concentration of intrinsic point defects in  $\text{Bi}_2\text{Te}_3$ -based alloys, particularly antisite defects, hence upgrading their thermal and electrical properties [100]. Thus, the Sb dopant is the precursor to improve the thermoelectric properties of  $\text{Bi}_2\text{Te}_3$  alloys, which are primary determinant by their intrinsic point defects. The intrinsic point defects have higher thermal stability than extrinsic Sb defects as they are mainly entropic defects, hence showing a stable TE performance at elevated temperatures [100].

### **2.7.1.2 Nanostructuring**

The nanostructuring approach should be combined with the atomic doping/alloying approach for effective ZT enhancements in  $\text{Bi}_2\text{Te}_3$ -based TE systems. This advancing approach is based mainly on the Quantum confinement effect in which the grains size will be reduced to nano-size (i.e. high boundaries scattering for low  $k_l$ ), while the energy bands will be converted to discrete energy levels with incremental  $E_g$  (i.e. high density of states (DOS) near Fermi level for high  $S$  [101]. This transition from the bulk-scale (3D) to the nanoscale has strengthened the phonon scattering mechanisms, particularly phonon-boundary and phonon-phonon scatterings. Thus, impeding the phonons transport (i.e. heat flow) across such a TE system without affecting the mobility of its charge carriers [101].

However, the nanostructuring is capable to scatter only the phonons with short to medium mean free paths (3-100nm) via increasing density of grain boundaries for strong phonon-boundary interactions, as illustrated in Figure 2.12 (a) [102]. Whereas, the phonons with the long mean free path (>100nm) are scattered via nano precipitates, point defects (e.g. atomic doping/alloying) and nanocomposite for strong phonon-

phonon interactions in presence of high-density interfaces and mesoscale grains [102]. Consequently, the accumulated percentage of  $\kappa_{\text{lat}}$  will be reduced significantly from atomic-scale via solid solutions, nanoscale via nanostructuring and nano precipitates, to mesoscale with mesoscale grains, hence incrementing ZT from 1.1, 1.7, to 2.2, respectively, as displayed in Figures 2.12 (a) and (b).

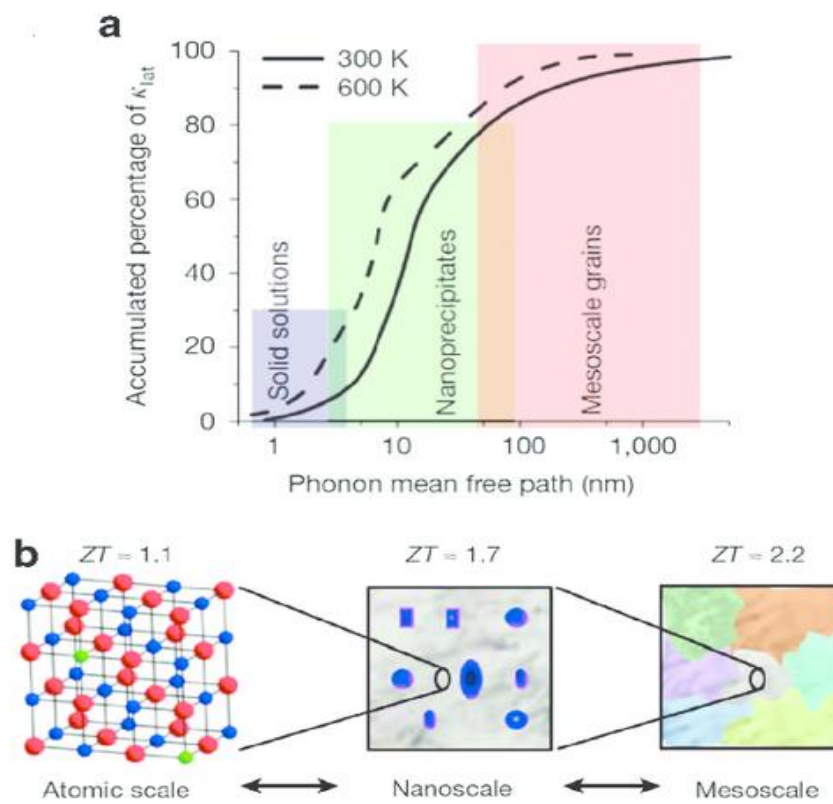


Figure 2.12 The Accumulated percentage of lattice thermal conductivity ( $\kappa_{\text{lat}}$ ) in terms of phonon mean free path (a) and the corresponding ZT values (b) for different phonon scattering approaches on multiple length scales [102].

Additionally, the grain-boundary and phonon-phonon scatterings play a significant role in improving TE performance, particularly in  $\text{Bi}_2\text{Te}_3$ -based TE systems

[103]. Thus, utilizing and integrating phonons scattering on multiple length scales (atomic, nano, and meso scales) to scatter all phonons in different frequencies have resulted in 30-50% ZT increments for the nanostructured  $\text{Bi}_{0.4}\text{Sb}_{1.6}\text{Te}_3$  [103]. This panoscopic approach is applicable for most of bulk TE materials to overcome their ZT enhancement challenges via harnessing all length scales towards efficient and effective phonons scattering.

### **2.7.1.3 Nanoemulsions**

The nanostructuring is not limited to nanosized grains instead it includes nanocomposites and nano inclusions, which must be taken into consideration for effective interface scattering of long-wavelength phonons. Thus, the presence of nano inclusions (i.e. nano precipitates) in the matrix of TE materials will increase significantly the density of grain boundaries and interfaces to lower further the  $k_l$ , as illustrated in Figure 2.13 [27]. This is due to their short mean free path of charge carriers, which is in few nanometers compared to the long phonons mean free path of hundred nanometers [104]. Thus, the combination of atomic doping/alloying (high point defects), nanostructuring (high-density grain boundaries), and nano-precipitates (high-density interfaces) are the optimal approaches in phonon transport engineering towards extensive and all-scale phonons scattering for lower  $k_l$  and ZT enhancements, as summarized in Figure 2.13.

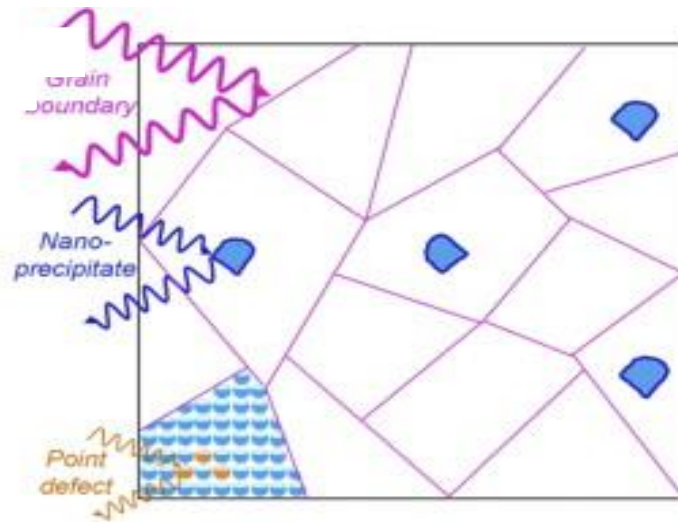


Figure 2.13 The Schematic representation of various advancing approaches based on phonon transport engineering for multiple length-scale phonon scattering [27].

It will also effectively scatter the phonons and particularly the ones with a high mean free path without affecting the carriers' mobility via carrier energy filtering effect. This effect is based on filtering out the low energy carriers via scattering them at the interfacial potential of nano inclusions and matrix to allow only the high energy carriers passing through [105]. This will increase PF and S with a negligible decrease in  $\sigma$ . For instance, the p-type  $\text{Bi}_2\text{Te}_3$  system is frequently reported with various dispersed nano inclusions (e.g. Te, SiC,  $\text{Y}_2\text{O}_3$ ,  $\text{CuInTe}_2$ , or ZnAlO nanoparticles) that have improved its mechanical properties (via blocking cracks growth and propagation in the bulk matrix) and TE properties (via interfaces and carrier energy filtering effect) [106]. It is also reported that the homogenous distribution of SiC nano inclusions in series of planes across the normal temperature gradient to the polycrystalline matrix of  $\text{Bi}_{0.3}\text{Sb}_{1.7}\text{Te}_3$  has strengthened its energy filtering effect at their interface to scatter numerous low energy carriers resulting in increased S and then ZT enhancements, as demonstrated in Figure 2.14 [88].

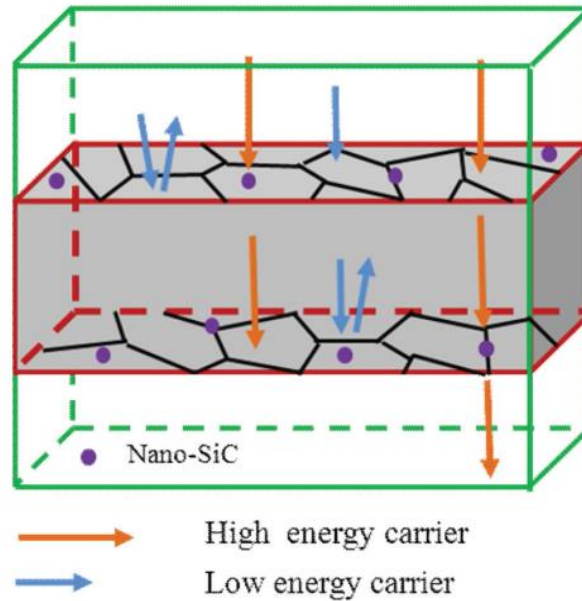


Figure 2.14 The Schematic representation of charge carriers filtering effect at SiC nano inclusions and  $\text{Bi}_{0.3}\text{Sb}_{1.7}\text{Te}_3$  interface [88].

## 2.7.2 Charge Transport Engineering

### 2.7.2.1 Nanocomposite

This is the main effective and recent advanced approach of charge transport engineering to enhance PF. It has overcome the dilemma of interconnectivity between TE properties through utilizing their strong reliance on the electronic and crystal structures of TE material towards optimizing the electron transport processes [107]. This breakthrough has improved significantly ZT of various conventional TE systems and offered pronounced suitability for vital practical applications in various WHR fields. This is referred to the effectiveness of introducing low-dimensionality structured materials (e.g. 2D, 1D, or 0D) into the nanostructured bulk TE material (3D) for improving its electrical and mechanical properties, hence high TE energy conversion efficiencies [107]. For instance, the compositing of nanostructured  $\text{Bi}_{2-x}\text{Sb}_x\text{Te}_3$  with 2D materials has proven its outstanding TE performance, particularly with the 2D

Graphene material [108]. This is due to its exceptional structural and electrical properties, which upgraded further the ZT of  $\text{Bi}_{2-x}\text{Sb}_x\text{Te}_3$  system, as summarized in Table 2.2 [109].

Table 2.2 The Summary of the Outstanding Properties for 2D Graphene Material [109]

Property		Graphene
Specific surface area	$\text{m}^2/\text{g}$	2630
Density	$\text{g}/\text{cm}^3$	>1
Thermal conductivity	$\text{W}/\text{m.K}$	5000
Electrical conductivity	$\text{S}/\text{cm}$	106
Charge mobility	$\text{cm}^2/\text{V.s}$	230,000
Elastic modulus	GPa	1100
Fracture strength	GPa	124

Additionally, the 2D Graphene is frequently characterized as a backbone for different graphitic materials due to its unique hexagonal lattice structure of covalently bonded carbon atoms in a form of a single and flat layer, as illustrated in Figure 2.15 [109]. It is also characterized as a semiconductor material with zero energy gap due to its lattice structure of 2D honeycomb carbon [110]. Thus, it has a high density of charge carriers (electrons and holes) that behave like massless relativistic particles (Dirac fermions) and move freely in rapid motions across the monolayer graphene, hence high electrical conductivity of  $\sim 106\text{S}/\text{cm}$  [110]. In addition, this single carbon layer is frequently reported with a high crystallinity structure of low defects density [110]. Thus, the absence of defects has resulted in raising its electrical conductivity as they



act as scattering sites for free charge carriers, which limit their mean free paths and inhibit their mobility. Accordingly, this thinnest sheet with a thickness of one carbon atom well matches the layered crystal structure of promising  $\text{Bi}_{0.4}\text{Sb}_{1.6}\text{Te}_3$  system for TE applications of low-temperatures [111].

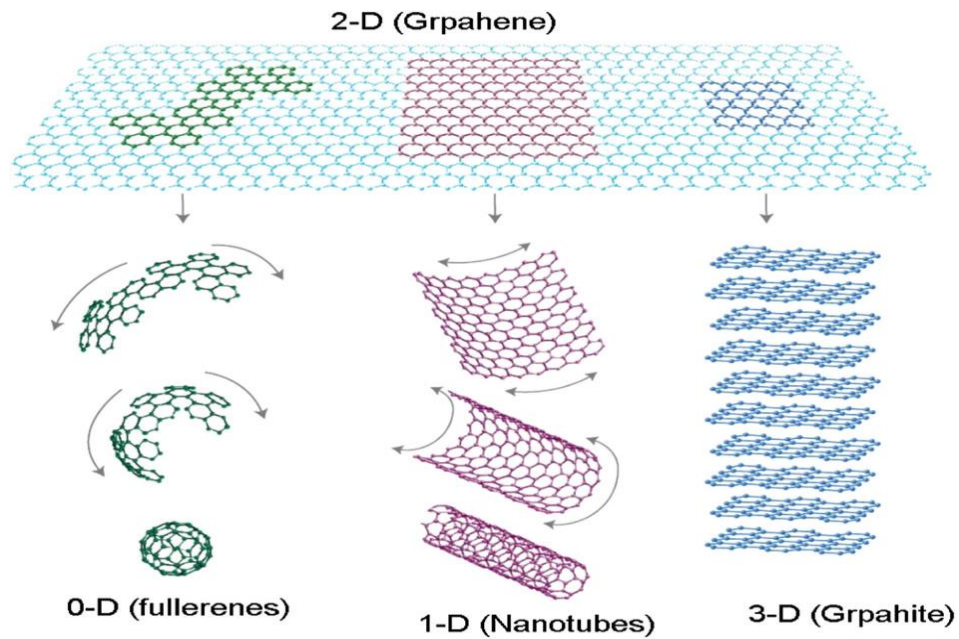


Figure 2.15 The Schematic representations of various graphitic materials based on the 2D graphene sheet [109].

However, the use of graphene in nanocomposite with  $\text{Bi}_{0.4}\text{Sb}_{1.6}\text{Te}_3$  system is limited due to its zero bandgap structure, which lowers  $S$  and strong C-C covalent bonds that leads to its high  $k$  of  $\sim 5000\text{W/m.K}$  [111]. Thus, the content of this conductive filler in  $\text{Bi}_{0.4}\text{Sb}_{1.6}\text{Te}_3$  metallic matrix should be selected properly to synthesis outstanding  $\text{Bi}_{0.4}\text{Sb}_{1.6}\text{Te}_3/\text{graphene}$  nanocomposites. Thus, attaining nanocomposites with low thermal conductivity, while high mechanical flexibility and electrical conductivity to fulfill the ZT enhancements towards high TE performance. Additionally, the strong

influence of graphene content on the lattice and total thermal conductivities of  $\text{Bi}_{2-x}\text{Sb}_x\text{Te}_3$  system is frequently proven, as displayed in Figure 2.16 (a) and (b), respectively [112]. This figure shows also that the graphene content of 0.05wt.% has the lowest  $k_{\text{lat}}$  and  $k_{\text{tot}}$  values for  $\text{Bi}_{0.48}\text{Sb}_{1.52}\text{Te}_3/\text{graphene}$  nanocomposites.

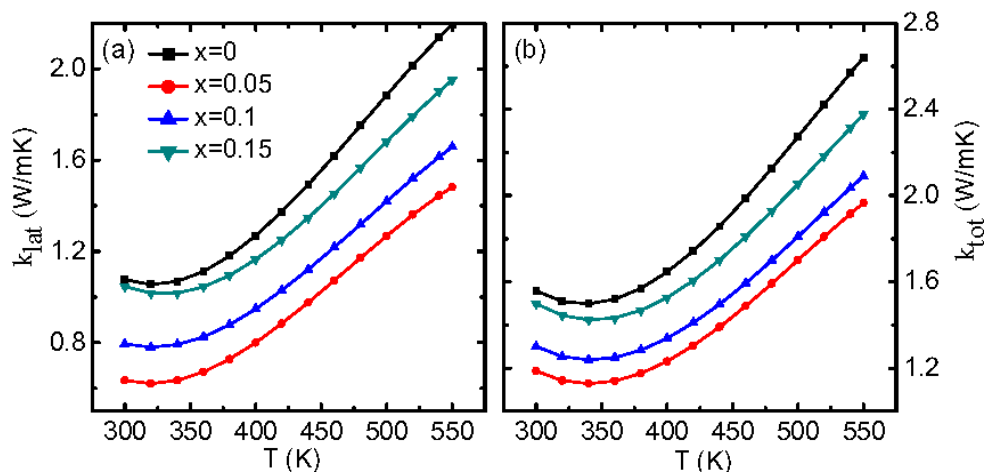


Figure 2.16 The Dependence of lattice (a) and total (b) thermal conductivities on the variations of graphene content ( $x$  in wt.%) for  $\text{Bi}_{0.48}\text{Sb}_{1.52}\text{Te}_3/\text{graphene}$  nanocomposites [112].

Accordingly, it has resulted in their ultra-high ZT values of  $\sim 1.26$  at 325K compared to the ZT of  $\sim 0.89$  for pristine  $\text{Bi}_{0.48}\text{Sb}_{1.52}\text{Te}_3$  (at  $x=0.00\text{wt}\%$ ) at the same temperature, as observed from Figure 2.17. This is referred to the well and even dispersion of graphene at low contents in nanostructured  $\text{Bi}_{0.48}\text{Sb}_{1.52}\text{Te}_3$  matrices, particularly near 0.05wt%. This has also facilitated its charge carrier transfer, strengthened its doping effect, and raised its interfaces densities for effective phonons scattering. Whereas, the graphene sheets tend to agglomerate and stakes on each other at high graphene contents ( $>0.05\text{wt}\%$ ) forming the graphite material (i.e. changing

from 2D graphene single layer to 3D graphite multiple layers) [113]. This undesirable state will destroy the unique structural properties of graphene and result in reducing its SA/V ratio, scattering its charge carriers, weakening its doping effect, and rising its k.

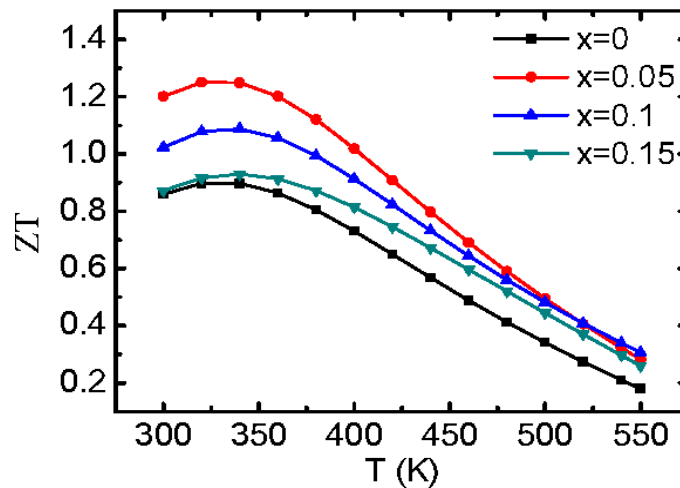


Figure 2.17 The Variations of ZT with graphene content (x in wt.%) for  $\text{Bi}_{0.48}\text{Sb}_{1.52}\text{Te}_3$ /graphene nanocomposites [112].

## 2.8 Thermoelectrics: Synthesis & Sintering Techniques

The selection of suitable synthesis and sintering techniques that satisfy the TE properties of certain TE system is a key parameter in designing high TE performance devices. This is referred to as the beneficial of property enhancement from processing development. Thus, there are numerous developments in different processing aspects to nanostructure advanced bulk TE materials, which focus on their nanopowder synthesis and sintering/consolidation techniques, as discussed in the below sections.

### 2.8.1 TE Synthesis Techniques: High-Energy Ball Milling (HE-BM)

The high-energy ball milling (HE-BM) is a simple and effective solid-state

mechanical grinding/alloying technique for facile synthesis and control of nano-grained alloys or nanocomposites via mechanochemical effect towards further ZT enhancements [114]. This powder metallurgical process can be easily scaled-up to matches the mass production requirements in industries to be a cost-effective and efficient method in commercializing TE materials on a large scale. It also produces well homogenous and narrows distributed nano-sized grains in 2-20nm via milling their powders of pristine metals in high-power mills [114]. It introduces the nanocrystalline structure into pristine powders through generating successively the 1D point and 2D dislocation defects in powder grains for their permanent deformation [115]. Thus, the powder grains undergo repeatedly the cold welding, crushing, and re-welding in dry milling conditions for effective transfer of high-energy impact to the milling powder from the successive collisions between milling balls in closed milling vial [115].

Additionally, there are multiple models of HE-BM machines such as shaker, planetary, and mixer mills, which undergo the same operating principle. Thus, the effectiveness of HE-BM is dependent on a set of parameters such as speed, time, number, and the ratio of milling balls to the milling powder (BPR). Accordingly, adjusting these parameters will result in a metastable structure either in the form of crystalline material (long-range order), solid solution (homogenous composition), an intermetallic compound, a mixture of components (non-homogenous composition), or amorphous material (short-range order) [115]. It will also result in the strengthening of nanostructured TE material (i.e. high hardness values) due to the constant increment in the density of generated defects with the milling time until their saturation limit [116]. However, there are other synthesis techniques of TE materials such as the chemical routes (e.g. solvothermal/hydrothermal methods), which are neither common nor effective due to their complexity, non-uniform grains, difficulties in controlling the

product morphology, and expensiveness in contrast to the physical routes (e.g. mechanical alloying) [117].

Moreover, this synthesis technique has proven its effectiveness in synthesizing the p-type  $\text{Bi}_2\text{Te}_3$ -based TE material and then has been utilized frequently to attain high ZT values, as shown in Figure 2.18 [118]. It is also observed from this figure that the effect of refined nanostructures on p-type  $\text{Bi}_2\text{Te}_3$  is dominated compared to other TE systems such as SiGe and Half-Heusler in either their nano n-type or p-type materials. Thus, the uppermost ZT value of 1.4 is reported for the nanostructured bulk BiSbTe based on the HE-BM processing technique, which offers great convenience for further optimization and utilization. This great TE enhancement is referred to the homogenous compositing, uniform nanograins distribution, and high defects density, which effectively suppressed the bipolar effect and strengthen the phonons scattering over wide wavelength spectrum [118]. This benefits in attaining lowest  $k_{\text{lat}}$  of 0.6 as noticed in Figure 1.8.

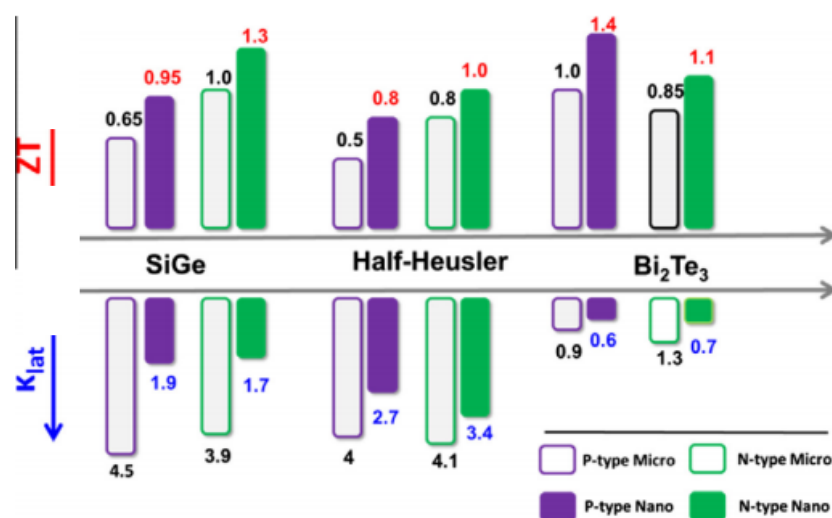


Figure 2.18 The Improved ZT and reduced lattice thermal conductivity ( $k_{\text{lat}}$ ) for various micro and nanoscale TE materials synthesized via HE-BM technique [118].

It is also reported that the mechanical strength of BiSbTe alloys has been improved significantly via nanostructuring them using HE-BM to overcome their cleavage nature due to their layered structure [119]. This is referred to the mixed orientations of cleavage planes and grain refinement, hence fulfilling the requirements for manufacturing miniaturized TE modules for practical applications [119]. It is also worth mentioning that this synthesis technique has shown outstanding TE performance in synthesizing homogenous nanocomposites and well-bonded interfaces of BiSbTe with graphene at room temperature in very short time to be the most favorable low cost and environmentally friendly synthesis approach for such nanocomposite. This has also assisted in simultaneous enhancements of electrical and phonon transport processes (i.e. increasing  $S$  and  $\sigma$ , while decreasing  $k_l$ ) towards the desired ZT enhancements [119].

### ***2.8.2 TE Sintering Techniques: FAST/SPS Sintering Press (DSP-510)***

The sintering of nano synthesized TE materials is the terminal stage in their processing to crystallize the grains in a compact form and stabilize further the main phase under suitable sintering conditions (dwell time, pressure, and temperature). This will result in a densely TE product with a fixed shape and high crystallinity for its TE measurements and characterizations. The efficient and rapid consolidation of a wide range of TE materials is recently reported via state-of-the-art Field Assisted Sintering Technology (FAST)/ Spark Plasma Sintering (SPS) machine manufactured by Dr. Fritsch Systeme GmbH, particularly model DSP-510 [120]. This advanced sintering press is an extension of the conventional Hot Pressing (HP) technique with design improvements to assist in fast, homogenous, and low-temperature sintering of various advanced TE ingots up to 70mm in diameter and 30mm in thickness [120]. It is reported as a promising sintering technique with interesting opportunities for industrial implementations towards improved and commercialized novel TE materials [120].

Additionally, this special version of SPS consists of a hydraulic pressing system, a water-cooled vacuum chamber, DC current pulse power supply system, vacuum, and atmospheric control system, and computer-aided process control system for measurement and control of sintering temperature and pressure (i.e. applied load) [121]. The presence of pulse power supply and absence of thermally insulated vessel or heating element in FAST/SPS has varied its performance from the conventional HP sintering technique. This unique design resulted in its homogenous heating, as well as, the sintered nanopowder, which is confirmed with negligible formation of thermal gradients ( $\Delta T$ ) across it even at elevated heating rates compared to conventional sintering techniques (e.g. HP), which are limited in application to low-moderate heating rates and longer dwell times ( $t^*$ ), hence incomplete homogenization, as illustrated in Figure 2.19 [122]. This figure shows clearly the typical thermal behavior of a sintering cycle for a nanopowder via recording its temperature at the center ( $T_I$ ) and edge ( $T_A$ ) to obtain its thermal gradients ( $\Delta T$ ) and dwells time ( $t^*$ ). This proves that FAST/SPS has the lowest  $\Delta T$  and  $t^*$ , which leads to its homogenous and fast sintering performance compared to the HP, respectively.

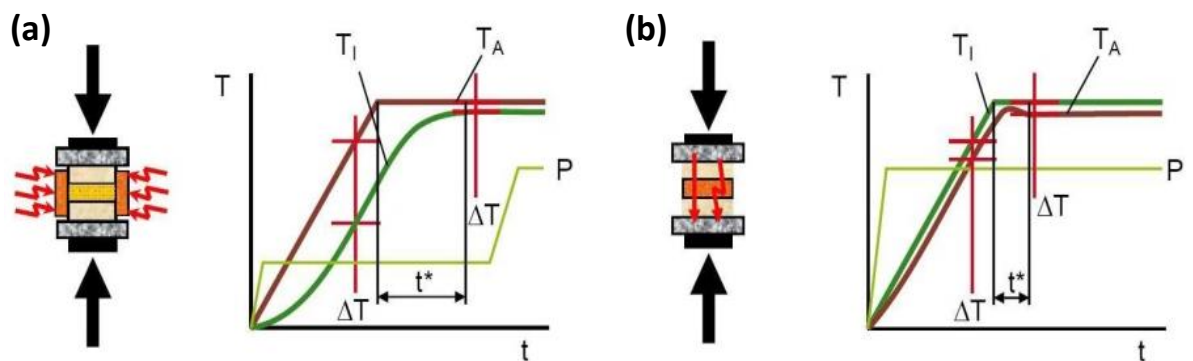


Figure 2.19 The Schematics for conventional hot pressing (a) and advanced FAST/SPS (b) sintering techniques of high-performance TE materials [122].

Therefore, the FAST/SPS technique is suitable for structural nanocomposite TE materials due to its fast powder consolidation, high heating and cooling rates via DC pulse electric current under atmospheric pressure and vertical uniaxial deformation [123]. This will result in multiple pulse cycles with homogenous distribution of heating power over the volume of sintered powder in the macroscopic scale and contact regions of powder particles on a microscopic scale [123]. This favorable sintering behavior ensures high reliability, easy operation, rapid sintering, and accurate control of various sintering parameters, especially sintering energy at high heating rates (e.g. 1000°C/min) [124].

This has also resulted in inhibiting powder decomposition and grains growth, which facilitate stabilizing and preserving the nanostructure of bulk TE nanocomposites, hence attaining the desired TE device with stable TE performance for reliable service [124]. For instance, the BiSbTe nanobulk is reported frequently with a significant reduction in its  $\sigma$  at elevated sintering temperatures via HP technique, while the opposite trend was observed via FAST/SPS technique [125]. This approves the different features of these sintering techniques and their impact on TE properties of sintered nanobulk TE materials.





## **Chapter 3: RESEARCH EXPERIMENTAL METHODOLOGY**


### **3.1 Thesis Research: Specimens Preparations**

The specimens in this thesis research are prepared based on the elemental powders of high purity Bismuth (Bi), Antimony (Sb), Tellurium (Te), and Graphene nanoplatelets, as displayed in Table 3.1. These powders have been utilized in the synthesis of 2 different nanopowder classes. The first class includes a set of specimens synthesized based on pristine  $\text{Bi}_{0.4}\text{Sb}_{1.6}\text{Te}_3$  alloy at fixed elemental compositions but different mechanical milling times ranging from 4, 8, 12, 16, to 20hrs. Accordingly, this class investigates the effect of milling time on the nanostructure and mechanical performance (i.e. Vickers Hardness) of synthesized nano-alloys. Its outcomes will be utilized in identifying the proper milling time for synthesizing the nanocomposites of  $\text{Bi}_{0.4}\text{Sb}_{1.6}\text{Te}_3$  and Graphene.

These nanocomposites are synthesized at the same elemental compositions and filler weight of 0.05wt.% Graphene. In this group, the time for nanocomposite formation will be optimized towards the desired stabilized nanocomposite structure and TE performance for reliable service and efficient thermoelectric energy conversion. This is attained via adjusting the time of filler addition (Graphene nanoplatelets) to the metal matrix (nanopowder of  $\text{Bi}_{0.4}\text{Sb}_{1.6}\text{Te}_3$ ). Thus, its addition time will vary from full time, half time, last 1hr, and last 5min of overall pre-identified proper milling time.

Table 3.1 The Summary of Raw Materials Utilized in this Thesis Research

Raw Material	Purity (%)	Source	Particles Size
Elemental Bismuth powder (Bi) 	99.999		200mesh (74 $\mu$ m)
Elemental Antimony powder (Sb) 	99.999	Alfa Aesar	200mesh (74 $\mu$ m)
Elemental Tellurium powder (Te) 	99.99		325mesh (44 $\mu$ m)

Raw Material	Purity (%)	Source	Particles Size
Graphene Nanoplatelets powder 	-	Sigma Aldrich	Few-layer graphene flakes with an average of 5-7 atomic layers.

This design approach fulfills the objectives of this thesis research in optimizing and stabilizing the structure and performance of BiSbTe/Graphene nanocomposites for the highest thermoelectric performance (i.e. high ZT values). Accordingly, the atomic and weight compositions of the two nanopowder classes are calculated and the outcomes are summarized in Table 3.2.

Table 3.2 The Atomic Composition, Mass Composition, and Elemental Weight for Specimens Preparations

Element	at. %	wt. %	g
Specimens Class (1): Pristine Bi <sub>0.4</sub> Sb <sub>1.6</sub> Te <sub>3</sub> Nanopowders			
Bismuth (Bi)	8.0000	12.643	0.7585
Antimony (Sb)	32.000	29.464	1.7678
Tellurium (Te)	60.000	57.894	3.4736
Total	100.00	100.00	6.0000

Element	at. %	wt. %	g
Specimens Class (2): Bi <sub>0.4</sub> Sb <sub>1.6</sub> Te <sub>3</sub> /Graphene Nanocomposites			
Bismuth (Bi)	8.0000	12.636	0.7582
Antimony (Sb)	32.000	29.449	1.7669
Tellurium (Te)	60.000	57.865	3.4719
Graphene	-	0.0500	0.0030
Total	100.00	100.00	6.0000

### 3.2 Thesis Research: Processing Methods

#### 3.2.1 TE Nanopowder Synthesis Method: High-Energy Ball Milling (HE-BM)

This TE nanopowder synthesis method was initiated with weighting the elemental weights of the raw powders, as displayed in Table 3.2. The weights were taken in the Glovebox laboratory equipment over an analytical balance for precise and accurate weights, as shown in Figures 3.1 (a) and (c), respectively. Then loaded into a well pre-cleaned and dried Stainless-Steel vial (SS-vial) and Stainless-Steel balls (SS-balls). This milling set is made up of hardened 440C stainless steel to avoid their degradation in the high energy milling process.

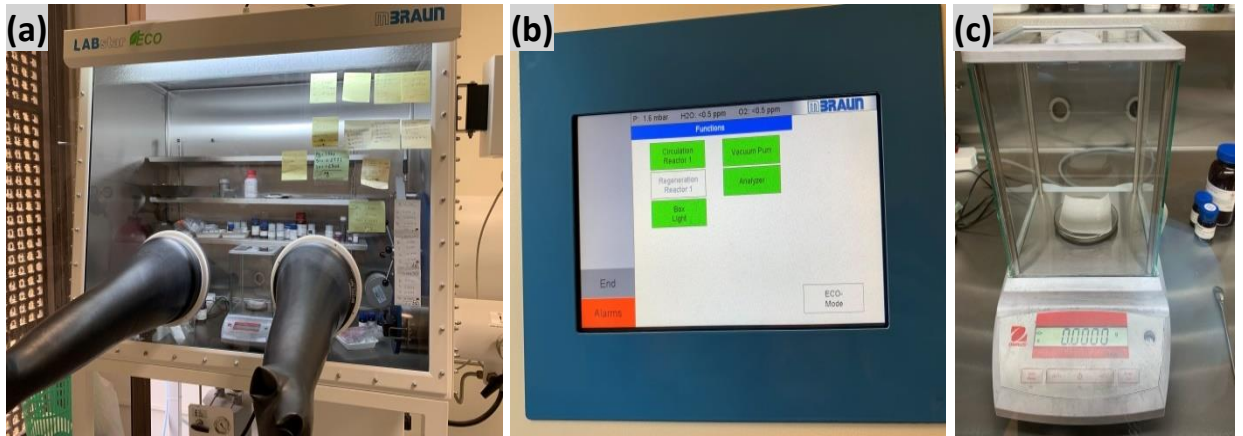


Figure 3.1 The mBRAUN-LABstar Glovebox workstation (a) and its touch panel (b) along with Ohaus balance weighing equipment (c).

Additionally, the Ball to Powder Weight Ratio (BPR) was kept at 10:1 via loading SS-balls with a total weight of 50g and weighted total powder of 6g into 65mL SS-vial. The used SS-balls are in two different sizes of 5/16in (7.94mm) and 1/4in (6.35mm) with an equal number of 16 SS-balls for each size, hence a total of 32 SS-balls. Then the SS-vial was tightly closed under dry and high purity Argon (Ar) atmosphere in the Glovebox with oxygen ( $\text{O}_2$ ) and moisture ( $\text{H}_2\text{O}$ ) contents of  $<0.5\text{ppm}$  as continuously monitored via the touch panel of Glovebox, as displayed in Figure 3.1 (b). This is to avoid impurities contamination and nanopowder oxidation during the long milling times. Then each of the specimens undergoes continuous milling on fixed milling conditions as shown in Table 3.3.

Table 3.3 The Common Conditions of High-Energy Ball Milling Adopted for Specimens Preparations

Milling atmosphere	Under dry and pure Ar atmosphere	
Milling temperature	~25°C	
Milling speed	1080cycle/min	
Ball to Powder Weight Ratio (BPR)	10:1	
Milling Type	High-Energy Shaker Mill	
Specimens Class (1): Pristine Bi <sub>0.4</sub> Sb <sub>1.6</sub> Te <sub>3</sub> Nanopowders		
Milling Times	4hrs	
	8hrs	
	12hrs	
	16hrs	
	20hrs	
Specimens Class (2): 0.05wt% Graphene/Bi <sub>0.4</sub> Sb <sub>1.6</sub> Te <sub>3</sub> Nanocomposites		
Specimen Code	Milling Times	
	Before Graphene Addition (hr/min)	After Graphene Addition (hr/min)
Full time	0/0	16/960
Half time	8/480	8/480
Last 1hr	15/900	1/60
Last 5min	15.92/955	0.083/5.00

Thereafter, the tightened closure SS-vial, which contains the SS-balls and specimen pre-weighed powder was loaded into the 8000M Mixer/Mills to undergo the high-energy ball milling process for nanopowder synthesis. This efficient laboratory mixer/mills shake sufficiently the SS-vial in complex motion combining back and forth swings with short lateral movements in approximately 1080cycle/min (60Hz). In each

swing, the SS-balls impact against one end of SS-vial for simultaneous milling of specimen powder and blending it, as illustrated in Figure 3.2 (d). It's worth mentioning that each of the SS-balls develops fairly high centrifugal forces in the SS-vial due to the efficient clamp's velocity and amplitude [126]. This vigorous motion of clamp pulverizes effectively the micro-sized raw powder into the desired nano-size powder, as well as, even blending of powder elements for their homogenous mixing and uniform distribution [126].

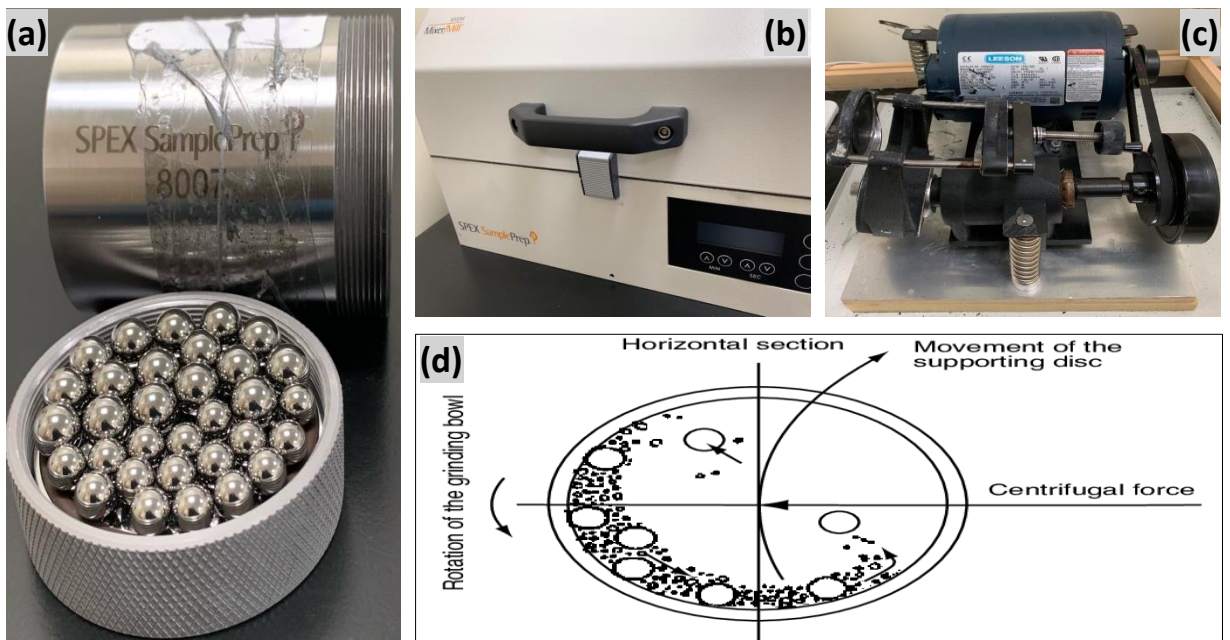


Figure 3.2 The SPEX SamplePrep 8007 Stainless Steel grinding vial set including a screw-on cap with O-ring and stainless-steel balls (a). The SPEX SamplePrep 8000-series Mixer/Mills (b) with single-clamp (c) and schematic of its high-energy ball milling process (d) [126].

### 3.2.2 TE Nanopowder Sintering Method: FAST/SPS Sintering Press (DSP-510)

The synthesized nanopowder using HE-BM method will undergo the sintering process to convert it into bulk nanomaterial for the measurements of its TE parameters ( $k$ ,  $\sigma$ ,  $S$ ,  $PF$ , and  $ZT$  values). This sintering process was accomplished using the advanced FAST/SPS Sintering Press in its model of DSP-510, as shown in Figure 3.3 (a). It sintered the nanopowder in 4 main repeated steps, which are: vaporization and solidification, volume diffusion, surface diffusion, and grain boundary diffusion, as clearly illustrated in Figure 3.3 (c) [127]. The effectiveness of these steps is dependent on its operating parameters. These parameters are also critical in thermal stabilization of nanopowders' microstructure, which will affect their TE performance in energy conversion. This is due to its main dependence on uniform temperature and uniaxial pressure in sintering TE nanopowders, hence rising possibilities for initiation of grains growth. Thus, the nanopowder of each specimen was loaded separately into a Graphite die in certain weights based on the rule of mixture calculations. These weights match precisely the volume of the target disc with 12.7mm in diameter and 3.5mm in thickness for its dense compaction, as displayed in Figure 3.3 (e).



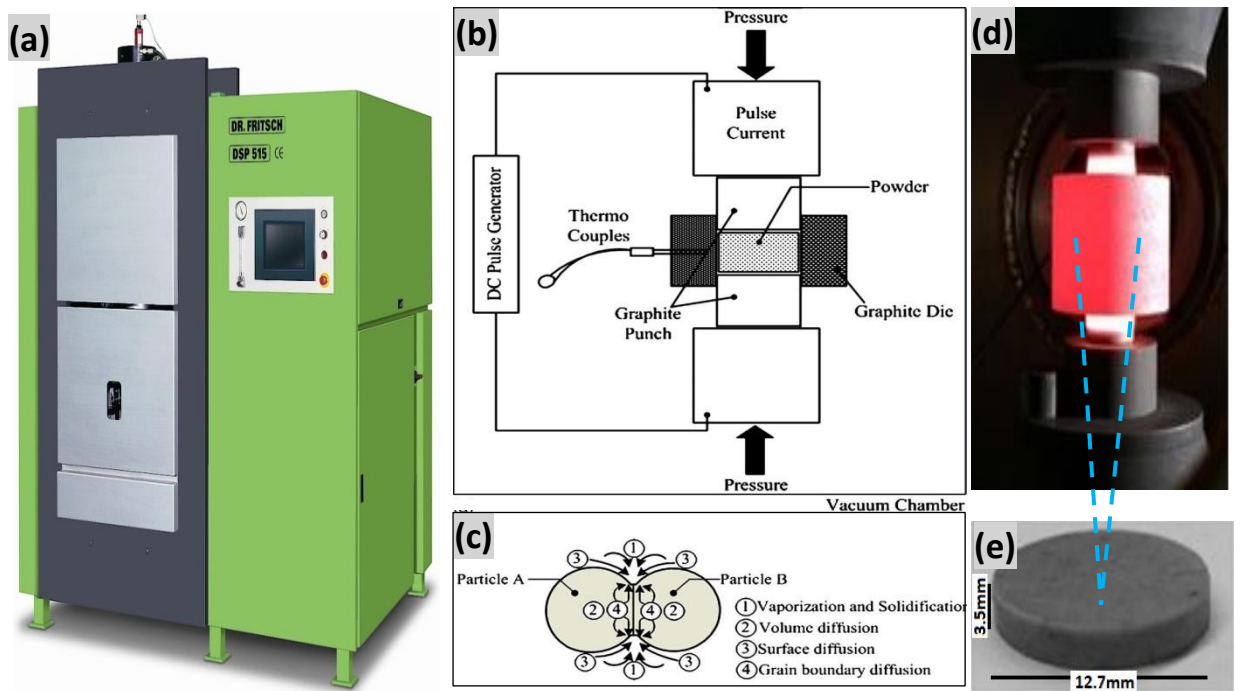


Figure 3.3 The FAST/SPS Sintering Press (DSP-510) (a) and schematics of its internal parts (b) and sintering process (c) for uniaxial consolidation (d) of nanopowder into a dense disc with the target dimensions (e) [127].

Thereafter, the filled graphite die was connected to thermocouples for precise temperature measurements to avoid ineffective pulsing of current and its over-heating consequences during the sintering process, hence it is an energy-saving technique [128]. Then it was loaded in between upper and lower graphite punches and each of them relates to a graphite spacer that's connected to graphite electrical electrode to control its displacement, as demonstrated in Figure 3.3 (b). The repeated use of graphite in internal parts of this sintering press is due to its low cost, high thermal and electrical conductivities [128]. After that, the DC power generator connected to the sintering press was turned on to allow the direct current (DC) flowing directly through the graphite sintering mold and specimen as both are made up of electrically conductive

materials. However, the presence of electrical resistance within the mold and specimen will speed up their sintering process due to an activation of the Joule's heating effect, as displayed in Figure 3.3 (d).

Thus, the temperature will be generated only if indeed and the sintering duration will be around 10min, as shown in Table 3.4. This short sintering duration is referred to the short sinter cycles due to the occurrence of the sintering process in an evacuated chamber (fine vacuum atmosphere of ~5Pa) followed by rapid cooling using an inert gas (Ar), which produces high-quality specimens. These short sinter cycles also benefit in minimizing grains growth, maximizing densities of compaction, improving microstructure, increasing productivity, and lowering their production costs compared to traditional HP [128]. Thus, conserving the nanostructure of TE synthesized nanopowder during its sintering process to attain the desired bulk nanomaterial with high thermal stability for efficient and reliable service. Accordingly, Dr.Fritsch FAST/SPS sintering press is the world market leader sintering technology for many applications, particularly in the TE industry [128].

Table 3.4 The Common Conditions of FAST/SPS Sintering Press (DSP-510) Adopted for Consolidating the Pre-Synthesized Nanopowder Specimens

FAST/SPS sintering pressure	45MPa		
FAST/SPS sintering temperature	280°C		
FAST/SPS sintering time	10min		
Dimensions of Graphite die	Diameter	Thickness	Volume
	12.7mm	3.5mm	443.4mm <sup>3</sup>
Powder weight loaded into Graphite die	Pristine Bi <sub>0.4</sub> Sb <sub>1.6</sub> Te <sub>3</sub>	Bi <sub>0.4</sub> Sb <sub>1.6</sub> Te <sub>3</sub> /Graphene	
	Nanopowder	Nanocomposites	

### **3.3 Thesis Research: Characterization Techniques**

#### **3.3.1 Structural Characterization Techniques**

The structural characterization of TE materials is crucial as it will reflect on their TE performance. Thus, several advanced structural characterization techniques have been utilized to investigate the specimens' microstructure, defects, average grain size and distribution, number of graphene layers, intermetallic compound phases, and lattice strain.

##### **3.3.1.1 X-Ray Diffractometer (XRD) Instrument**

The X-Ray Diffractometer (XRD) is a non-destructive analytical technique for investigating the crystal structures, intermetallic compound phases, average grain size, and lattice strain for the pre-synthesized nanopowder specimens [129]. This technique was conducted using the EMPYREAN model of PANalytical XRD instrument, as shown in Figure 3.4 (a). This instrument consists primary of an X-ray tube, which radiates X-rays using alpha Copper (Cu  $K\alpha_1$ ) anode with an average wavelength ( $\lambda$ ) of 1.5406Å and high intensity for excellent resolution, as illustrated in Figure 3.4 (b). It also consists of the sample holder to hold the nanopowder specimens and an X-ray detector (PIXcel model) to count and detect the diffracted x-rays in order to generate the XRD diffractogram of the specimen, as displayed in Figures 3.4 (d) and (b), respectively.

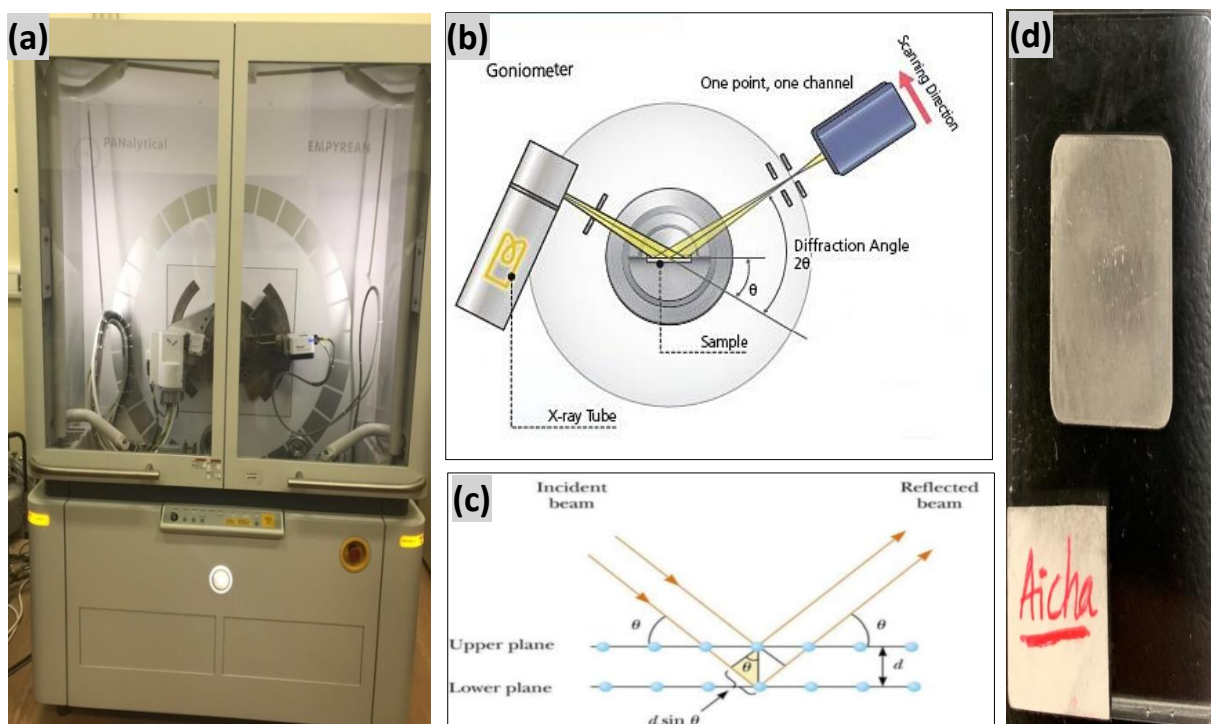


Figure 3.4 The PANalytical X-Ray Diffractometer (XRD) instrument of EMPYREAN model (a) and schematics diagrams for its operating principle (b) and Bragg's law parameters (c) along with the used sample holder for nanopowder specimens (d) [129].

Accordingly, this XRD instrument was powered on at 45kV and 40mA, as displayed in Table 3.5. Then the electrical current was flowing across the x-ray tube causing the excitation of its anode material, which is the Cu  $K\alpha_1$ . This excitation resulted in ejecting the electrons in inner energy levels of Cu by a beam of electrons from the supplied electric current (i.e. flow of electrons per unit time). Now, the electrons in the outer energy levels of Cu will fall into the vacant inner energy levels through radiating their extra energy in the form of electromagnetic waves (X-rays) in order to fit the energy of new levels and return the Cu atoms to their stable state. These waves have a constant wavelength of  $1.5406\text{\AA}$  and will pass through filters consisting

of thin foils in order to generate monochromatic radiation containing mostly Cu K $\alpha$  (i.e. electrons falling from L- to K- shells), which are filtered from the Cu K $\beta$  (i.e. electrons falling from M- to K- shells) [130].

This monochromatic radiation will pass through a collimator to be collimated (for shaping the x-ray beam) to concentrate it on the nanopowder specimen. These collimated x-rays will be directed onto the crystalline nanopowder and the intensity of the reflected x-rays will be detected and counted by a detector that's connected to a computer in order to monitor the displayed diffractogram of the specimen. The goniometer is used to rotate the sample holder in the direction of incident collimated x-rays and control its rotation angle ( $\theta$ ). It is also used to rotate the mounted detector at an angle of  $2\theta$  to collect the diffracted x-rays from the sample. The data of all tested specimens were collected based on a continuous scan on the scan-axis of  $2\theta$  to  $\theta$  at scan range of  $2\theta$  from  $\sim 10^\circ$  to  $\sim 100^\circ$  with a scan rate of  $0.000246^\circ/\text{sec}$ , as summarized in Table 3.5.

Table 3.5 The Uniform Operating Conditions of PANalytical XRD Instrument (EMPYREAN model) on the Pre-Synthesized Nanopowder Specimens

Anode material	Cu K $\alpha$ 1	$\lambda = 1.5406\text{\AA}$	
$2\theta$ Scanning range		10-100 $^\circ$	
Step size		0.01313 $^\circ$	
Scan rate		0.000246 $^\circ/\text{sec}$	
Operating conditions	45kV	40mA	25 $^\circ\text{C}$

Additionally, the intensity peaks in the obtained diffractograms of the tested nanopowder specimens have resulted from the occurrence of constructive interference

that indicates the satisfaction of Bragg's law at these peaks. This originates from the incident monochromatic x-rays beam, which has an incident angle ( $\theta$ ) between the sample and x-ray source, whereas, the reflected beam has a diffracted angle ( $2\theta$ ) between the detector and incident beam. The detector angle ( $2\theta$ ) is always twice the incident angle ( $\theta$ ). In case the path difference between the adjacent crystal planes ( $2d \cdot \sin\theta$ ) equals an integer ( $n$ ) multiplied with the x-ray constant wavelength ( $\lambda$ ), then the constructive interference will occur and the Bragg's law will be satisfied, as demonstrated in Figure 3.4 (c) [131]. In such law, the wavelength ( $\lambda$ ) of electromagnetic radiation is related to both the lattice spacing ( $d$ ) and diffractive angle ( $\theta$ ) of the crystalline nanopowder, as shown in Equation (3.1) [131]. The only variable in this law is  $d$ , which refers to the spacing between the crystal planes and provides a fingerprint of elements and intermetallic phases within the tested specimen.

$$n * \lambda = 2 * d * \sin\theta \quad (3.1)$$

Furthermore, the broadening of peaks within XRD diffractogram could be related to the average grains size and lattice strain within the tested nanopowder specimens. Thus, an integral breadth analysis was carried out to quantify these parameters using 3 different methods namely: Scherrer, Williamson-Hall, and Warren-Averbach methods [132]. The Scherrer method calculates only the average grain size, while Williamson-Hall fails at very small grain sizes [132]. Consequently, the outcomes of the Warren-Averbach method are the most reliable as frequently reported and will be compared with TEM average grains distribution for its confirmation [133]. This reliable method was conducted based on Equation (3.2) and its outcomes will be displayed and discussed in chapter (4) [134].

$$\frac{\beta^2}{\tan^2\theta_0} = \frac{\lambda}{d} \left( \frac{\beta}{\tan\theta_0 \sin\theta_0} \right) + 25(e^2) \quad (3.2)$$

Where,  $d$  is the average grains size,  $e$  is the lattice strain,  $\theta_0$  is the diffraction angle of

peak in radian,  $\beta$  is equivalent to FWHM in radian, which was obtained for each peak by plotting it separately and fitting it using the Gaussian Fit in the OriginPro software, and  $\lambda$  is the constant wavelength of x-rays produced by cathode ray tube and equivalent to 0.15406nm.

### **3.3.1.2 Transmission Electron Microscope (TEM)**

The Transmission Electron Microscope (TEM) is an innovative analytical instrument that provides rapid and accurate imaging in sub-Angstrom resolution. This crucial structural characterization technique was utilized to investigate the topography (surface features), morphology (shape and size of particles), composition (existing elements and compounds), and crystallographic information (atoms arrangements) of specimens [135]. These structural outcomes are in high significance as it is in direct relation to the properties of the specimens, particularly mechanical (e.g. hardness), electrical (e.g.  $\sigma$ ), thermal (e.g.  $k$ ), and thermoelectric (e.g. PF and ZT) properties. Thus, the Thermo Scientific Talos F200C TEM instrument was used to image the pristine BiSbTe and its nanocomposites with 0.05wt.% graphene, as shown in Figure 3.5 (a). This TEM's model has a constant-power and C-TWIN lens for outstanding optical performance to ensure optimal balance between contrast and resolution [135]. This innovative design increases its imaging stability, throughput, and easiness in use.

Accordingly, its outstanding performance in imaging is a consequence of its advancing working principle. This principle is based on the use of highly energetic electrons forming a beam that will transmit through the specimen to image it on a very fine scale (nm), hence yielding the valuable structural outcomes. This first launched type of electron microscopes has a similar pattern to the light microscope except that it uses focused electrons beam instead of light to image the specimen[136]. This electrons beam has been used to overcome the limited resolution (~200nm) of optical

microscopes in imaging the nanostructured specimens. This insufficient resolution is due to the presence of nano-sized particles, which are much smaller than the wavelength of the incident light.

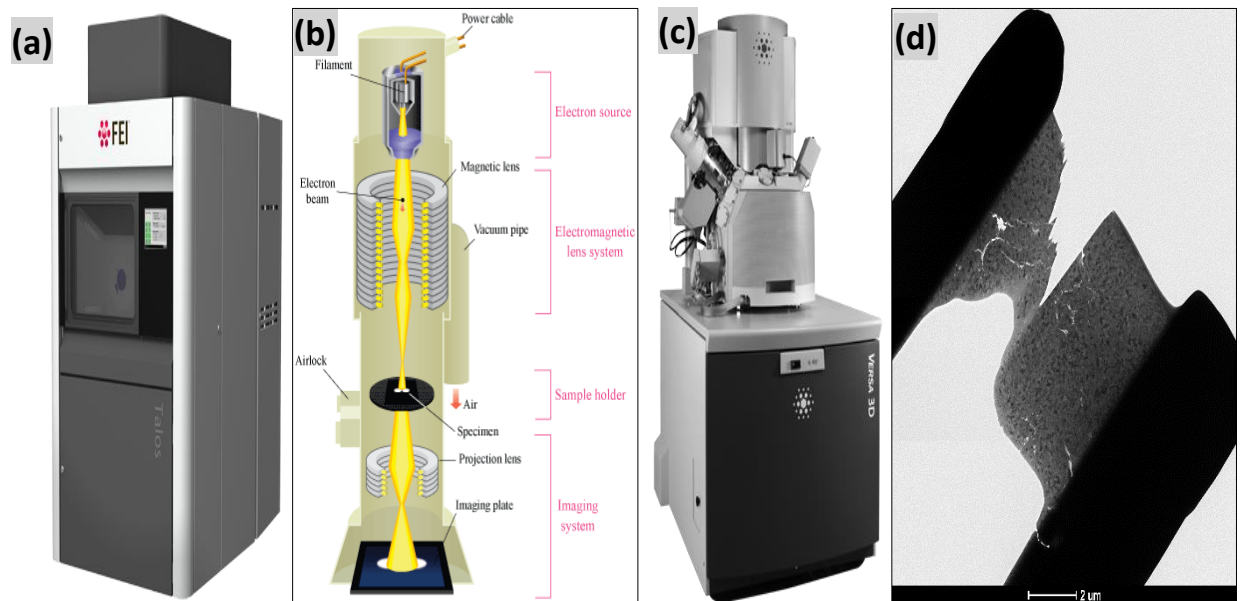


Figure 3.5 The Thermo Scientific High-Resolution Transmission Electron Microscope (HR-TEM) instrument of Talos F200C model (a) and schematic diagram for its electron column (b) along with the used FEI Versa 3D Dual Beam FIB/SEM instrument (c) for specimens thinning (d) [137].

Therefore, its electron column is designed with an electron source/gun including filament, electromagnetic lens system including condenser lens with aperture, sample holder, and imaging system including objective lens with aperture, projector lens, imaging grid/plate, and fluorescent screen, respectively, as clearly demonstrated in Figure 3.5 (b). The imaging was initiated with turning its power on ( $\sim 200\text{kV}$ ) to



allow the emitted monochromatic and coherent electrons beam with uniform current density from the Talos field emission gun to illuminate the specimen through an electromagnetic condenser lens and aperture in the vacuum electron column. Then the condensed electrons have an incident in parallel beam onto the specimen and resulted in a number of interactions with its atoms, which could result in elastic and inelastic scatterings [137].

This has raised various signals that are detectable using a fully integrated 16MPixel CMOS detector for faster imaging and improved reliability. The volume of these interactions increases with increasing acceleration voltage, while decreases with the increasing atomic number [138]. Then the objective lens provided the information on the specimen from these interactions either in the form of TEM bright/dark field image or diffraction pattern displayed on the image grid. The distribution intensity of transmitted electrons is further magnified with the projector lens to be viewed on a fluorescent screen at the bottom of the column.

Additionally, the specimen should be ultrathin ( $<0.5\mu\text{m}$ ) for transmitting the electron beam and forming the TEM images in good contrast. Thus, the Fischione double-jet electropolishing (model 110) and Ultramicrotomy on cold-pressed discs with 3mm in diameter and 1mm in thickness were used for specimens thinning but neither of the techniques worked and ended up with fractured thin layers. Thus, all the tested TEM specimens were soaked with low viscosity epoxy resin ( $\sim 250\text{cPa}$ ) under vacuum ( $\sim 0.1\text{-}0.15\text{mbar}$ ) for  $\sim 15\text{min}$  to mechanically stabilize the specimens. Then a cross-sectional of TEM lamella (ultrathin layer) was prepared using Focused Ion Beam (FIB) for specimens thinning via FEI Versa 3D Dual Beam FIB/SEM instrument, as displayed in Figure 3.5 (c). This powerful instrument is based on dual beam of electrons and ions that intersected the specimen surface at a coincident point with an angle of  $\sim 52^\circ$ . This

allowed the direct imaging of FIB-modified surface in high resolution using SEM for nanometer precision. This unique system with complementary imaging and beam chemistry capabilities has success in specimens thinning to ~35nm with the precise control of energy and intensity of incident ion beam, as shown in Figure 3.5 (d).

Consequently, the TEM mode was conducted to obtain the typical Bright Field (BF), Dark Field (DF), and Distribution of Particles (DP) TEM images along with diffraction patterns (e.g. Selected Area Diffraction (SAD)). Whereas, the Scanning Transmission Electron Microscopy (STEM) mode was used for qualitative elemental mapping via High-Angle Annular Dark-Field (HAADF) detector in conjunction with FEI Energy Dispersive X-ray (EDX) detector that count, and sort characteristic X-rays based on their energy. The main difference between these modes is that the focused electron beam in STEM is in a raster pattern to scan the specimen, which gives high spatial resolution compared to conventional SEM [139]. In this mode, the transmitted e-beam has been scattered in a large angle and then was detected by HAADF detector.

Therefore, the TEM outcomes will be utilized in investigating the average grain size and their distribution, as well as, type of defects presents in the specimens such as dislocations, twin boundaries, and stacking faults. It is worth mentioning, that such outcomes are not obtainable via another electron microscopy, particularly Scanning Electron Microscopy (SEM). This is because it is based on scattering electrons rather than transmitting them, hence used to investigate the 3D surface morphology in resolution of nm rather than 2D imaging of internal structures including: tiny precipitates, grain boundaries, dislocations, and defect structures in polycrystalline solid specimens, which are accomplished in much higher resolution ( $\text{\AA}$ ) via TEM [140].

### **3.3.1.3 Raman Microscope**

The Raman microscope is an advanced, reliable, and non-destructive analytical

microscope to characterize the crystal structure of different novel materials. Thus, the Thermo Scientific DXR Raman microscope has been utilized for the structural characterization of the embedded graphene nanoplatelets, which are used as fillers into the metallic matrix of BiSbTe, as shown in Figure 3.6 (a). In this vibrational technique, the specimen was irradiated with a laser beam emitted from the light source. This has resulted in the generation of an infinitesimal amount of Raman scattered lights, which were detected using a CCD camera to obtain the desired Raman spectrum [141]. This spectrum is the characteristic fingerprint pattern of Raman microscope and then it has been utilized in identifying the presence of graphene, evaluating its crystallinity and layers thickness.

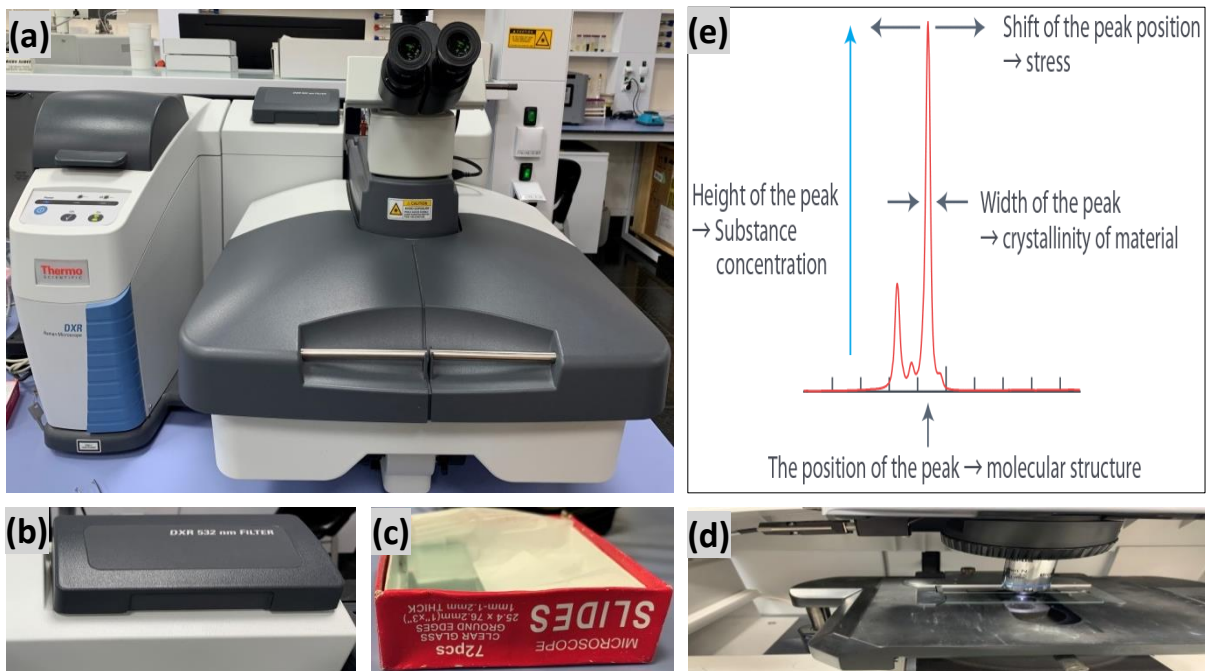


Figure 3.6 The Thermo Scientific DXR Raman microscope instrument (a) and the used DXR 532nm FILTER for laser excitation (b) of specimens placed over clear glass microscope slides (c) under Raman microscope (d) to obtain their Raman spectrum (e) [141].

This is accomplished via monitoring the peaks position and intensity in the Raman spectrum. For instance, the intensity of peak within the Raman spectrum has resulted from symmetric lattice vibrations that induce many distortions of e-cloud surrounding the molecules within the specimen [142]. This could be utilized in tracking changes in crystallinity and the 2D structure of reinforced filler (graphene nanoplatelets) in the metallic matrix (BiSbTe) of synthesized nanocomposite specimens. On the other hand, the peak position shows the specific vibrational mode of the present molecular functional groups within the specimen and any shift in their position is due to residual stresses from nearby surrounding functional groups, as illustrated in Figure 3.6 (e). Thus, the Raman spectrum is crucial in proving the molecular fingerprint of synthesized nanocomposites, as well as, its filler.

Additionally, this characterizing technique is based on the Raman Effect in which the interaction of incident light with the molecules within the specimen results in polarizing them via distorting their e-cloud to non-equilibrium state, hence immediate radiation of the absorbed photon as scattered light [142]. This scattered light arises from the molecular vibrations and could be resulted either from elastic or inelastic scatterings. The elastic scatterings are known as Rayleigh scatterings where there is no change in the energy of incident light beam (i.e.  $\lambda_{\text{incident light}} = \lambda_{\text{scattered light}}$ ) [143]. Whereas, the inelastic scatterings lead to the energy change between the incident light and scattered light (i.e.  $\lambda_{\text{incident light}} \neq \lambda_{\text{scattered light}}$ ) [143]. This was observed experimentally in 1928 by Chandrasekhara Raman, hence known as Raman scatterings (Raman Effect) [143].

In this Raman instrument, only Raman scattered lights were recorded, while the Rayleigh scattered lights were rejected using a filter for simplicity in interpreting the Raman spectrum. This spectrum is in a form of the intensity of Raman scattered

light versus Raman shift or Wavenumber, which is a reciprocal of the wavelength. The advantage of representing the Raman spectrum in terms of wavenumber is that the obtained spectrum will be independent on the wavelength of the used laser excitation due to the linear proportionality of wavenumber with photons energy [144]. Thus, all the specimens were tested using the same laser excitation with a fixed wavelength of 532nm, as displayed in Figure 3.6 (b). These nanopowder specimens were placed over clear glass (SiO<sub>2</sub>) microscope slides prior to being tested under Raman microscope, as shown in Figures 3.6 (c) a (d), respectively. The uniform operating conditions of structural characterization conducted via the DXR Raman microscope is summarized in Table 3.6. It's worth mentioning that graphene exhibits fluorescence with Near Infra-Red (NIR) lasers (e.g.  $\lambda_{\text{laser}}= 785\text{nm}$  or  $780\text{nm}$ ), hence the nanocomposite specimens have been deposited on the SiO<sub>2</sub> microscope slides along with the use of visible lasers (e.g.  $\lambda_{\text{laser}}= 633\text{nm}$  or  $532\text{nm}$ ) [144].

Table 3.6 The Uniform Operating Conditions of DXR Raman Microscope Instrument on the Pre-Synthesized Nanopowder Specimens

Laser excitation	DXR 532nm Laser
Microscope substrate	Clear glass (SiO <sub>2</sub> )

### 3.3.2 Mechanical Characterization Techniques

#### 3.3.2.1 Vickers Micro-Hardness Tester Instrument

The Vickers micro-hardness tester is a standard, reliable, and advanced instrument to investigate the mechanical properties of TE specimens, particularly Vickers hardness ( $H_v$ ). In prior to the hardness testing, the nanopowder specimens have

to undergo sequenced preparation operations for smooth and precise hardness testing. Thus, they have undergone hydraulic press to be transformed into compact discs with 3.0mm in diameter and 1.0mm in thickness using the Carver Hydraulic Laboratory Press instrument, as shown in Figure 3.7 (a).

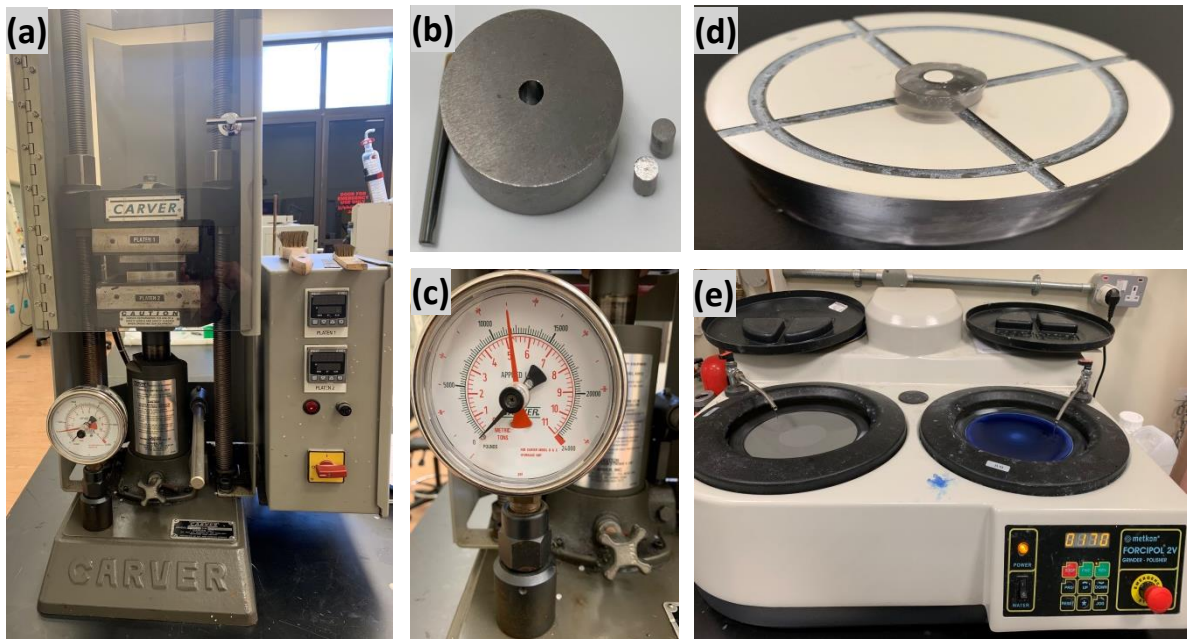


Figure 3.7 The Carver Hydraulic Laboratory Press instrument of 4386 Model (a) with the used Tungsten Carbide die and rods (b) along with its gauge reads (c). The compacted discs placed over quartz cylinder in specimen holder (d) prior being grinded/polished using Metkon Grinder/Polisher automatic machine with double wheels and FORCIPOL-2V model (e).

The nanopowders' weight for compaction was around 16mg based on the rule of mixture calculations, as summarized in Table 3.7. This weighted powder was loaded into a Tungsten Carbide (WC) die and the WC rods were used for cold compression of

the powder under compaction load of a 0.72metric ton (mt), which was monitored via gauge readers, as displayed in Figures 3.7 (b) and (c). Then the cold-compacted discs were glued over the quartz cylinder and placed in the specimen holder to easiness their grinding and polishing using Metkon Grinder/Polisher automatic machine with double wheels, as shown in Figures 3.7 (d) and (e), respectively.

Table 3.7 The Uniform Operating Conditions of Carver Hydraulic Laboratory Press Instrument for Cold compaction of the Pre-Synthesized Nanopowder Specimens

Compaction load	0.72mt		
Compaction temperature	25°C		
Compaction time	2min		
Dimensions of WC die	Diameter	Thickness	Volume
	3.0mm	1.0mm	7.07mm <sup>3</sup>
Powder weight loaded into WC die	Pristine Bi <sub>0.4</sub> Sb <sub>1.6</sub> Te <sub>3</sub> Nanopowders	Bi <sub>0.4</sub> Sb <sub>1.6</sub> Te <sub>3</sub> /Graphene Nanocomposites	
	15.739mg	15.742mg	

In the grinding operation, the emery (sand) paper was used as a coarse abrasive with a grit size of P1200. The specimens were rotated several times in 90° with sustaining an equal pressure on them to ensure a uniform grinding, eliminate completely the surface scratches, and attain a specimen surface that's ground flat with enough smoothness. Then the specimens were polished on a polishing cloth that was inserted into the rotating wheel. This polishing cloth was lubricated with a small amount of Metkon Alumina (Al<sub>2</sub>O<sub>3</sub>) suspension (0.05µm) used as a fine abrasive material that's capable to well polish the hard surface of the specimen by rubbing. In a similar manner

to grinding, the polishing was also done under moderately flowing water and  $90^\circ$  specimen rotation to ensure even polishing until the specimen surface becomes glossy as a mirror. At the end of polishing, the specimen was rinsed with water and well dried to ensure the removal of any suspended alumina particles on its surface prior to its hardness testing.

Thereafter, the hardness test was conducted on the polished discs using the Micro-Hardness Tester instrument and model of FM-ARS9000 that uses a range of micro-indentation testing methods based on the indenter size to measure the resistance to the localized surface deformation, as shown in Figures 3.8 (a) and (b). The used diamond indenter has intersected with the surface of the underneath specimen in an angle of  $\sim 136^\circ$  between the faces to form a clear square-based pyramid with diagonals of  $d_1$  and  $d_2$ , as demonstrated in Figure 3.8 (c).

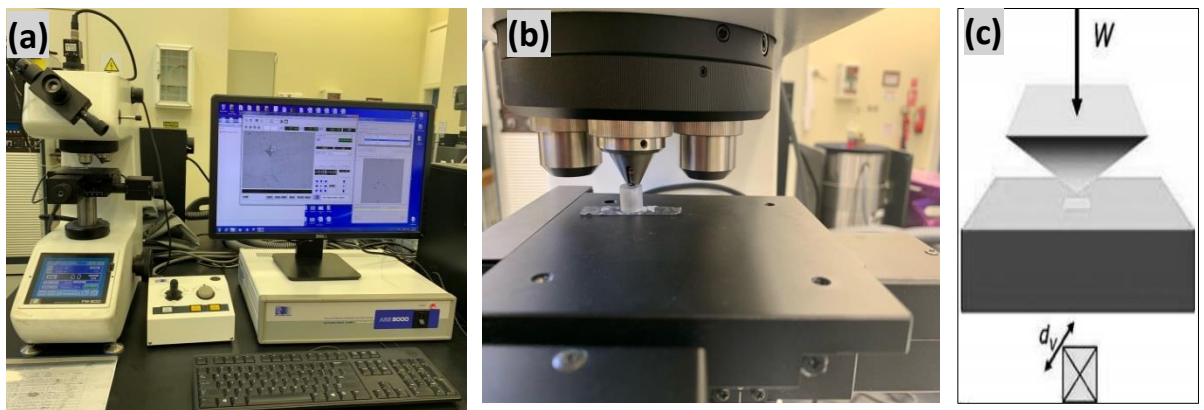


Figure 3.8 The Future Tech. Vickers Micro-hardness Tester instrument of FM-ARS9000 model (a) with diamond indenter placed above-tested specimen (b) and schematic diagram for the resulted Vickers diamond square-based pyramid (c) [145].



Accordingly, this tester was operated at the Vickers Hardness ( $H_V$ ) scale in which a very small diamond indenter with pyramidal geometry is forced onto the TE specimen surface at a test load of 25gf (0.245N) for a dwell time of 10sec, as displayed in Table 3.8. The resulting micro-indentation is observed under a microscope and measured by software attached to this instrument. This measurement was converted into a hardness number using Equation (3.3) and its outcomes will be discussed in chapter 4 [145].

$$H_V = 1.854 * \frac{W}{d_v^2} \quad (3.3)$$

Where the  $H_V$  is the Vickers hardness (or hardness number) in MPa,  $W$  is the applied weight/load in N, and  $d_v$  is the average diagonal length of square-based pyramid indentation in m, as illustrated in Figure 3.8 (c).

Table 3.8 The Uniform Operating Conditions of Vickers Micro-hardness Tester Instrument on the Cold-Compacted Specimens

Hardness scale	HV
Applied test load/force	25gf (0.245N)
Dwell time	10sec
Object lens	Lens x50
No. of indentations per specimen	5

### 3.3.3 Thermal Characterization Techniques

#### 3.3.3.1 Differential Scanning Calorimeter (DSC) Instrument

The Differential Scanning Calorimeter (DSC) is a flexible, easy-to-use, and powerful thermal analysis technique, particularly its Q2000 model. This model is the

world leader in the thermal analysis due to its proven superior performance in sensitivity, precision, resolution, and baseline flatness, as shown in Figure 3.9 (a). Thus, it has been utilized in investigating the thermal behavior of TE specimens including their phase transition temperatures (melting and crystallization temperatures), enthalpies (heat content), crystalline behavior, and eutectic transitions. These values will be utilized in identifying the proper sintering temperature of TE specimens to avoid their nanograins growth and decay in TE performance, which will, in turn, stabilize further their TE structure and performance for reliable service.

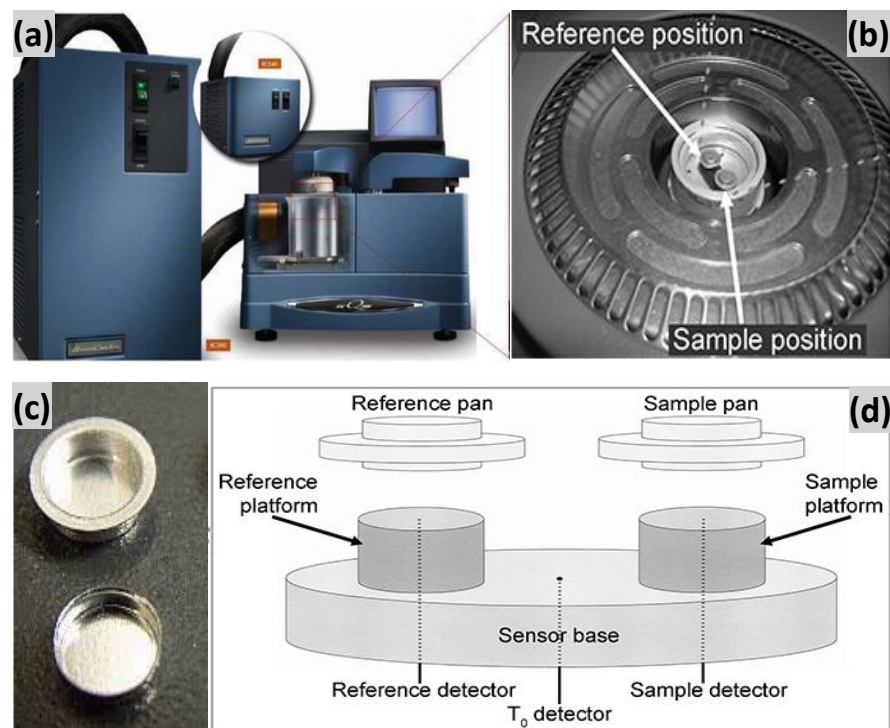


Figure 3.9 The TA Differential Scanning Calorimeter (DSC) instrument of Q2000 model (a) with its DSC cell containing the reference and sample pans (b) made up of Tzero Aluminum (c) along with schematic diagram on its DSC cell arrangements (d) [146].

Accordingly, this well-equipped DSC instrument consists mainly of an external cooling unit, purge gas unit, DSC main unit, DSC cell, DSC cell controller, and Tzero Aluminum pans to satisfy the top DSC operating conditions, as displayed in Figures 3.9 (a), (b), and (c). The DSC cell has an inner two adjacent raised platforms on a sensor base located at bottom of its enclosure and connected to different detectors. The sensor base is made up of silver for optimum thermal conduction to the upper reference and sample pans. These pans are made up of Tzero Aluminum and it is crucial to always place them on their corresponding platforms for proper DSC operation, as demonstrated in Figure 3.9 (d) [146]. Thus, all the TE specimens were placed in the Tzero Aluminum pan and placed over the sample platform is adjacent to an empty reference pan into the Q2000-DSC instrument for their thermal analysis. This instrument was connected to computer software to monitor the pans temperatures via the attached cooling unit and regulate its heat flows via the purge gas unit.

The attached cooling unit to DSC Q2000 provides heating/cooling to the DSC cell to control precisely its operating temperature in range of -90 to 550°C, while the purge gas unit is used to continuously purge the DSC cell at constant flow rates to ensure efficient heat transfer across the unit via removing moisture, off-gases, and hot spots. The used purge gas in this DSC model was Argon as it is easily available, low thermal conductivity, inert, and inexpensive gas. This purge gas where heated sufficiently before entering the DSC cell to ensure equilibrating its temperature with the temperature of the entire DSC cell without interfering with the heat measurements. Then both pans were heated spontaneously from room temperature to maximum temperature in the DSC instrument at a linear and constant heating rate, as shown in Table 3.9. The differences in temperature records of each pan measured by its corresponding thermocouple have resulted in detecting sample thermal critical points.

Table 3.9 The Uniform Operating Conditions of Q-2000 Differential Scanning Calorimetry (DSC) Instrument on the Nanopowder Specimens

Powder weight loaded into pan	~5.20mg
Purge gas flow rate	Argon in 20ml/min
Pan	Tzero Aluminum
Temperature range	30-430°C
Heating rate	10°C/min
Operating steps	<ol style="list-style-type: none"> <li>1. Equilibrate at 30°C</li> <li>2. Isothermal for 5min</li> <li>3. Ramp 10°C/min to 430°C</li> <li>4. Isothermal for 1min</li> <li>5. Ramp 10°C/min to 30°C</li> <li>6. Ramp 10°C/min to 430°C</li> <li>7. Isothermal for 1min</li> <li>8. Ramp 10°C/min to 30°C</li> </ol>

### 3.3.4 Thermoelectric Characterization Techniques

#### 3.3.4.1 NETZSCH SBA-458 Nemesis® Instrument

The NETZSCH SBA-458 instrument is based on a new, innovative, and practical design for simultaneous measurements of Seebeck coefficient ( $S$ ) and electrical conductivity ( $\sigma$ ) for TE samples in temperature ranges of RT to 1100°C, as shown in Figure 3.10 (a). This is referred to its novel setup that has resulted in precise and reliable measurements of thermophysical properties ( $S$  and  $\sigma$ ) under identical conditions, as displayed in Figures 3.10 (b) and (c). This setup is based on thermocouples and current pins placed on the lower surface of the sample to measure its  $\sigma$  via the 4-point method, as demonstrated in Figure 3.10 (d) [147]. Whereas, the micro-heaters, which operate in alteration are placed below the 2-edges of the sample

to create a cyclic heating environment with a uniform temperature gradient ( $\Delta T$ ) in both sample directions (from left to right or right to left of the sample). This has resulted in the generation of thermal voltage ( $\Delta V = V_A - V_B$ ) across TE sample, as demonstrated in Figure 3.10 (e). This voltage is measured via thermocouple wires and used in calculations of  $S$ , which is a ratio of  $\Delta V$  to  $\Delta T$ , as pre-discussed in section 2.3.1.

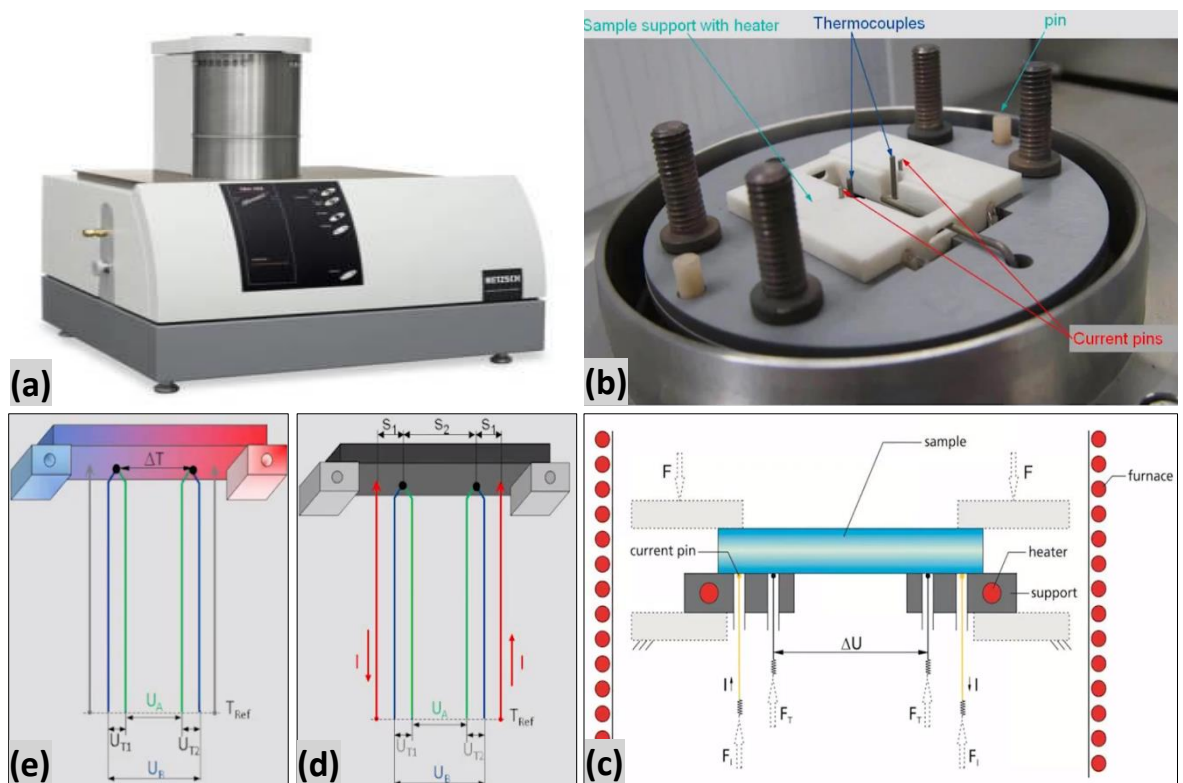


Figure 3.10 The NETZSCH SBA-458 Nemesis<sup>®</sup> instrument (a) and the entire sample setup (b) along with its schematic diagrams for sample setup (c), measurements of electrical conductivity (d), and Seebeck coefficient (e) [147].

Additionally, its plug-and-measure feature offers the ability to measure  $S$  and  $\sigma$  for unlimited sample geometries in different dimensions [147]. This is due to

eliminating the distance determination between the mechanically fixed thermocouples, hence easy, rapid, and accurate thermophysical properties measurements. These thermocouples are Inconel<sup>®</sup> sheathed with type K (NiCr/NiAl) to avoid either adhesion or chemical contamination between sample and thermocouple for homogenous thermal and electrical contacts. It has also a valuable integrated quality check feature to record the  $S$  and  $\sigma$  values either prior to or while it is in progress. This has enabled the precise characterization of thermophysical properties for the pre-consolidated TE specimens in optimized testing times, as summarized in Table 3.10.

Table 3.10 The Uniform Operating Conditions of NETZSCH SBA-458 Nemesis<sup>®</sup> Instrument on the Pre-Consolidated Nanopowder Specimens

Sample geometry	Round disc	
Sample dimensions	Diameter	Thickness
	12.7mm	3.5mm
Temperature ranges	323-425K	
Heating rate	200K/min	
Purge gas flow rate	Inert Argon in 50ml/min	
Operating conditions	Pins Current	Heaters Voltage
	0.05A	8V

#### 3.3.4.2 NETZSCH LFA-467 HyperFlash-Light Flash Apparatus

The NETZSCH LFA-467 instrument offers a fast data acquisition, high sample throughput, wide temperature range (-100 to 500°C), and accurate measurements, as shown in Figures 3.11 (a) and (b). This is referred to its analyzer that simplifies and fastens the measurements of specific heat ( $C_p$ ), thermal diffusivity ( $a$ ), bulk density ( $\rho$ ),

and thermal conductivity ( $k$ ) as functions of temperature. This is attained via the adopted Light Flash (LFA) technique in its working principle, which is a non-contact, non-destructive, fast, and absolute method to determine various thermal properties [148]. Accordingly, this efficient method has been utilized in the measurements of  $k$  for the pre-consolidated TE specimens in conjunction with  $S$  and  $\sigma$  values obtained from SBA-458 towards PF and ZT values using Equations (2.17) and (2.18), respectively. Additionally, a light pulse with short energy was used to heat the front surface of the TE samples, which resulted in temperature deviation of its rear face to radiate Infra-Red energy that was measured by the IR detector, as demonstrated in Figures 3.11 (c) and (d).

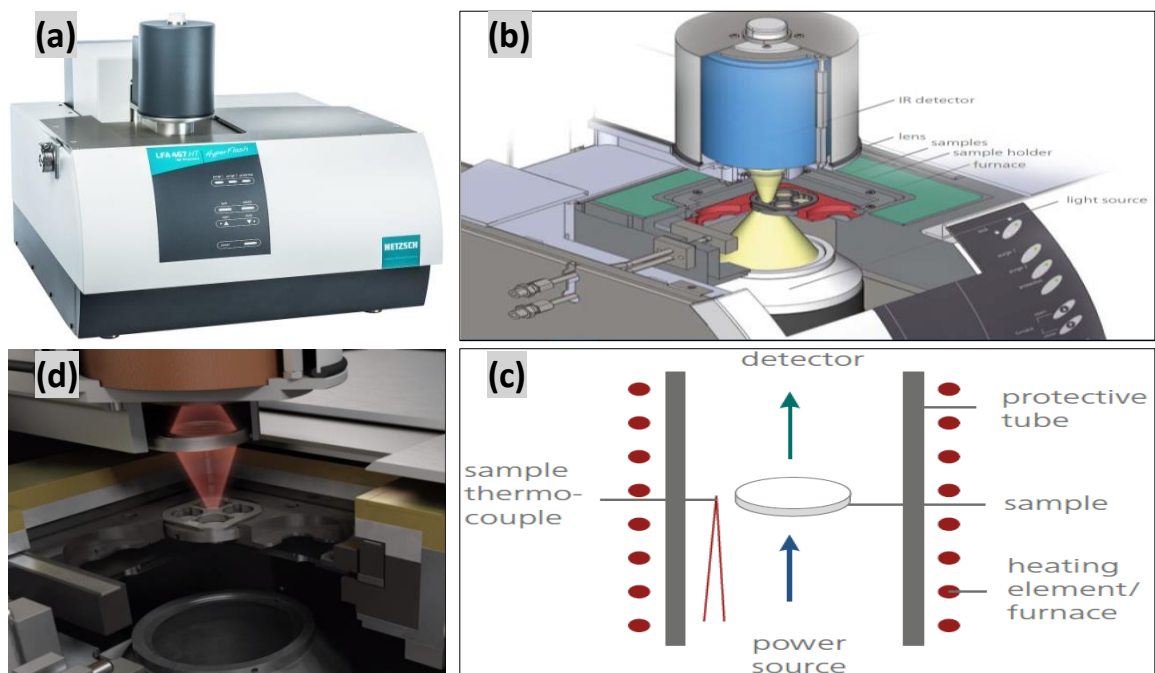


Figure 3.11 The NETZSCH LFA-467 HyperFlash-Light Flash Apparatus (a) and the entire sample setup (b) along with its schematic diagram for sample setup (c) and light flash technique (d) [148].

The k measurements via LFA-467 were conducted in homogenous temperature distribution and under the inert Argon atmosphere in the vertical system due to the sensitivity of TE samples to oxygen, as displayed in Table 3.11. This system is designed with an IR detector at the top, TE sample at the center, and Xeon lamp, which serves as a flash source at the bottom [148]. This innovative design has enabled its thermal coupling to various cooling devices, which raised its heating rates to 50K/min, reduced its measurement times, and maintained its excellent thermal stability. It's worth mentioning that the LFA-467 design includes a stepper-motor-actuated lens inserted between TE sample and IR detector to optimize the field of view by software control, which prevents the measuring artifacts due to the presence of aperture stop that delays the IR signal, hence precise measurements [148].

Table 3.11 The Uniform Operating Conditions of NETZSCH LFA-467 Instrument on the Pre-Consolidated Nanopowder Specimens

Sample geometry	Round disc	
Sample dimensions	Diameter	Thickness
	12.7mm	3.0mm
Temperature ranges	323-425K	
Heating rate	5K/min	
Purge gas flow rate	Inert Argon in 50ml/min	



## Chapter 4: RESEARCH RESULTS & DISCUSSIONS

### 4.1 Structural Characterization

#### 4.1.1 X-ray Diffraction Analysis of the Pristine $\text{Bi}_{0.4}\text{Sb}_{1.6}\text{Te}_3$ Nanopowders

The evolution of the nanocrystals structure of this promising TE performance system for low-temperature applications has been analyzed via a set of structural characterization techniques including XRD and TEM. The XRD patterns of nanocomposites matrix show the formation of single-phase  $\text{Bi}_{0.4}\text{Sb}_{1.6}\text{Te}_3$  nanocrystals at different mechanical milling times, as displayed in Figure 4.1 (a). The characteristic peaks of these XRD patterns are consistent with the standard peaks of rhombohedral  $\text{Bi}_{0.4}\text{Sb}_{1.6}\text{Te}_3$  intermetallic compound phase in the Inorganic Crystal Structure Database (ICSD 98-002-0071) [149].

This good agreement in peaks positions and intensities prove the uniform crystallographic structure and atomic composition of synthesized BiSbTe nanocrystals, as illustrated with diffraction lines in Figure 4.1. (a). This figure shows also the appearance of Bragg's fundamental peak for this crystalline metallic matrix with indexed crystal plane of (015) at low Bragg's angle ( $2\theta$ ) of  $28.01^\circ$  in very strong intensity. It appears at narrow angular range of  $2\theta$  with FWHM value of  $<0.5$  indicating the high crystallinity and long-range order of synthesized nanocrystals in comparison to the extremely broad peaks that appear as hump over wide angular range of  $\sim 10^\circ$  in typical diffraction patterns of amorphous materials [150].

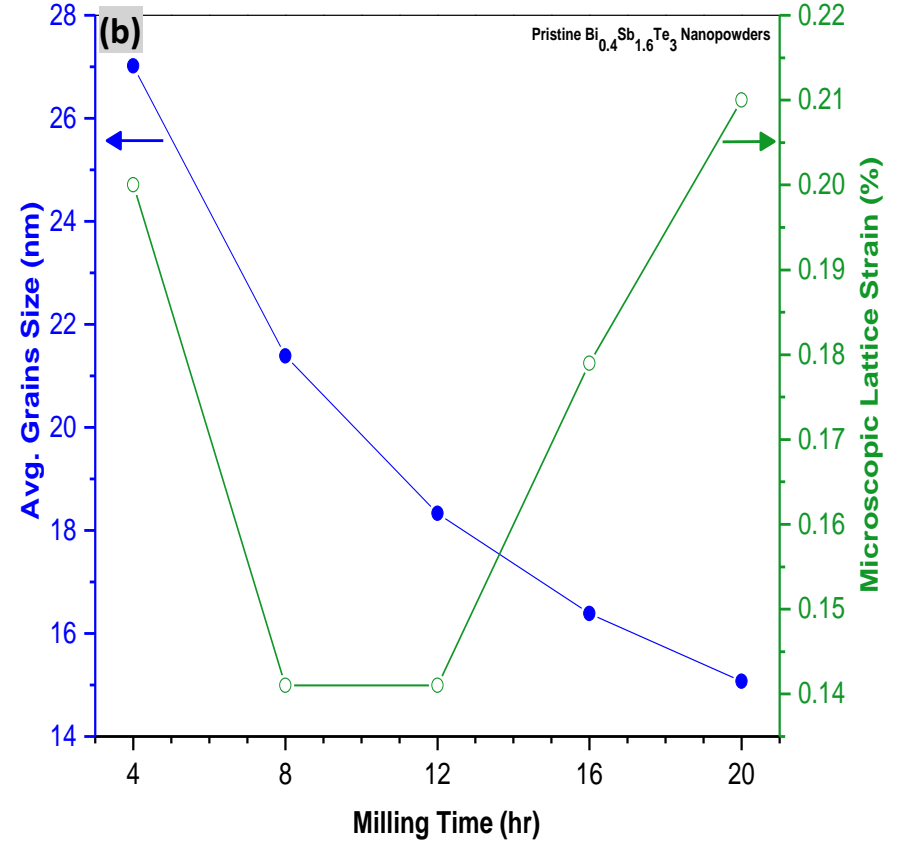
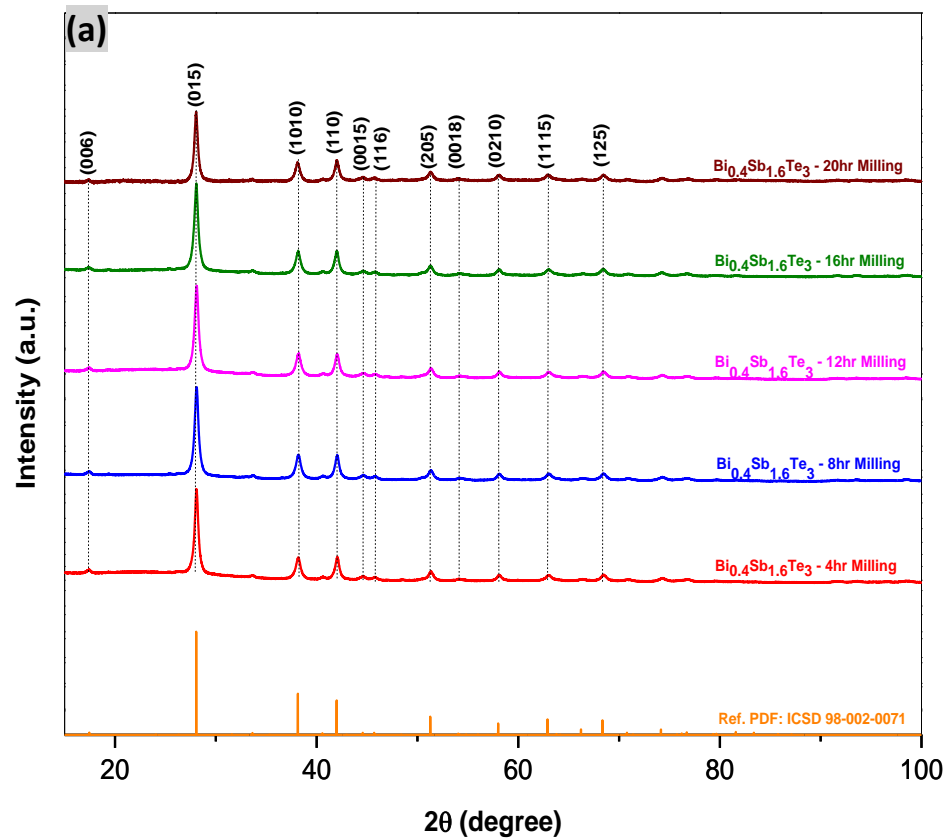


Figure 4.1 The XRD patterns of the pristine  $\text{Bi}_{0.4}\text{Sb}_{1.6}\text{Te}_3$  nanopowders (a) milled at 4, 8, 12, 16, and 20 hours. The Effect of milling time on average grains size (in blue) and microscopic lattice strain (in green) of pristine  $\text{Bi}_{0.4}\text{Sb}_{1.6}\text{Te}_3$  nanopowders (b) based on the integral breadth analysis on their XRD patterns using Warren-Averbach method.

Additionally, the broadening in the observed XRD peaks profile of synthesized BiSbTe nanopowders gives a reliable insight on their average crystallites size and residual lattice strains, which have been quantified using Warren-Averbach method (see section 3.3.1.1 in chapter 3 for details), as displayed in Figure 4.1 (b). This figure shows that the average grain size of synthesized BiSbTe nanocrystals gradually decreases with increasing milling time. The synthesized nanocrystals have undergone a smooth reduction in their size with the incremental of the mechanical milling time by a factor of 4hrs. This reduction in grain size has reached its plateau stage after 16hrs of milling and turns to a negligible difference of 1nm at 20hrs, as shown in Figure 4.1 (b). This indicated that the 16hrs of mechanical milling is enough for synthesizing a single-phase intermetallic compound of  $\text{Bi}_{0.4}\text{Sb}_{1.6}\text{Te}_3$  with an average grain size of 16nm and lattice strain of 0.18%. Thus, the composition milled for 16hr is adopted in this thesis to be suitable for synthesizing the desired nanostructure of BiSbTe.

On the other hand, the residual microscopic lattice strains in the milled BiSbTe nanopowders have not exceeded 0.21% after 20hrs of milling, as displayed in Figure 4.1 (b). These microstrains are distinguishable from macrostrains due to the absence of positions shift in any of the diffraction peaks in the XRD patterns of nanopowders [151]. This indicates the presence of microstresses in nanocrystals lattice, which could contribute to the broadening of diffraction peaks. The lattice strains could mainly microstresses resulted from some imperfections in nanocrystals lattice such as stacking faults, vacancies, lattice dislocations, grain boundaries, shear planes, and solid solution inhomogeneity [152]. These lattice imperfections are frequently observed in nanosized crystallites (grain size <100nm) and could affect the structure-sensitive properties of BiSbTe/Graphene nanocomposites such as electrical conductivity and fracture strength [153]. However, their contribution could be inadequate and then retaining the

refinement in grain size of BiSbTe nanocrystals, as observed from the broadening profile of XRD peaks in Figure 4.1 (a).

#### ***4.1.2 X-ray Diffraction Analysis of the Graphene/Bi<sub>0.4</sub>Sb<sub>1.6</sub>Te<sub>3</sub> Nanocomposites***

The graphene nanoplatelets have been added in 0.05wt% to the pre-synthesized single-phase Bi<sub>0.4</sub>Sb<sub>1.6</sub>Te<sub>3</sub> nanocrystals milled for 16hrs. The low contents of graphene particularly near 0.05wt% has proven its well and even dispersion in the nanostructured BiSbTe matrices, as pre-shown in Figures 2.16 and 2.17 [112]. This will facilitate its charge carrier transfer, strengthen its doping effect, and raise its interfaces densities for effective phonons scattering. The graphene was added to the p-type nanopowder at different times of milling, as pre-displayed in Table 3.3. The resultant BiSbTe/Graphene nanocomposites XRD profiles match the pre-selected pristine BiSbTe nanopowder milled to 16hr, as presented in Figure 4.2 (a). This figure investigates the influence of milling time to the graphene distribution and integrity in the p-type BiSbTe matrix.

Additionally, the diffraction pattern of graphene shows the presence of its Bragg's fundamental peak at 26.35° in very strong intensity, narrow angular range, and FWHM value of <0.5. This diffraction peak is indexed with a crystal plane of (002) at low Bragg's angle and considered as a fingerprint of 2D nanostructure for graphene nanoplatelets [154]. However, this peak did not appear in the diffraction pattern of synthesized BiSbTe/Graphene nanocomposites, as shown in Figure 4.2 (a). This could be attributed to the small amount of the added graphene (0.05wt.%).

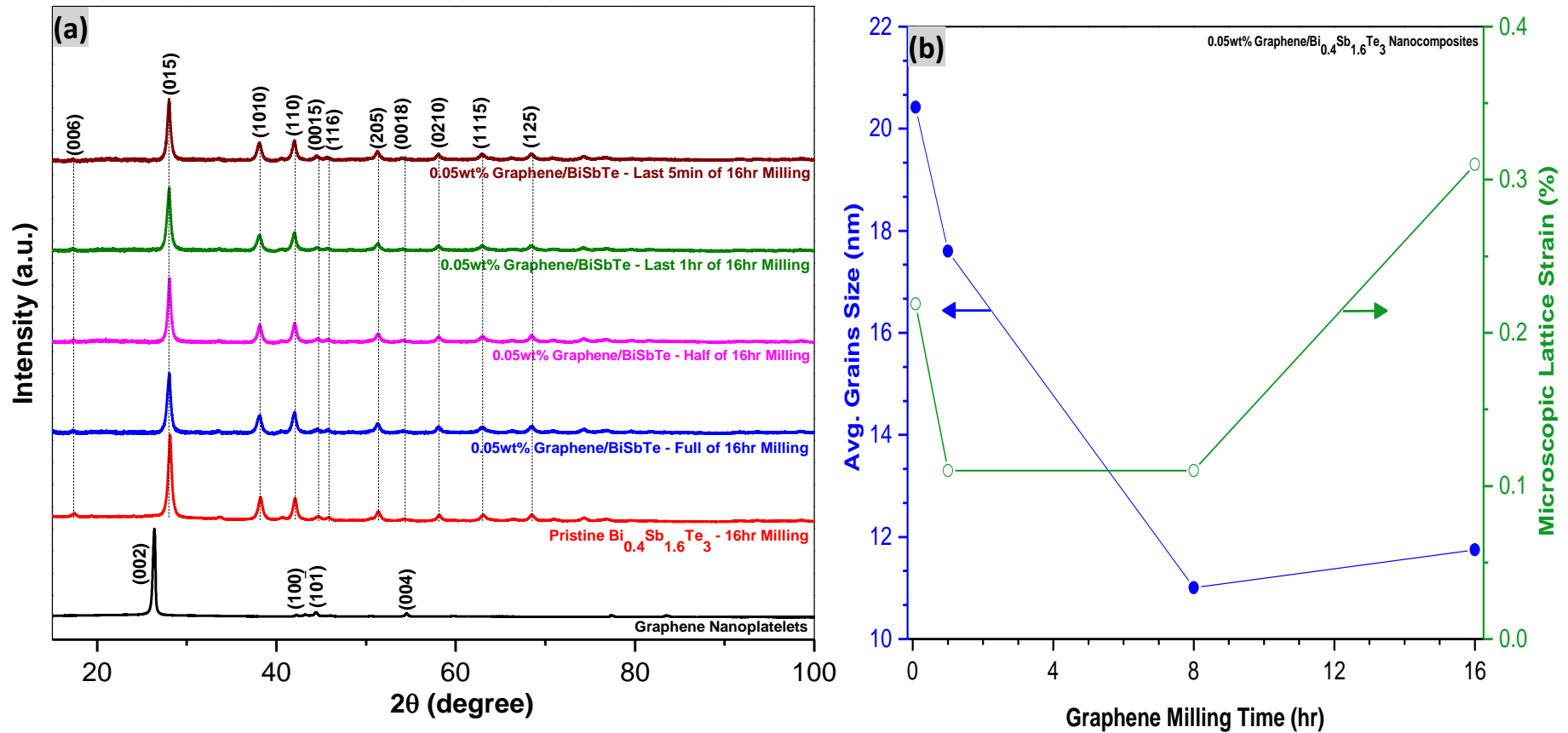


Figure 4.2 The XRD patterns of the Graphene nanoplatelets alone and 0.05wt% Graphene/Bi<sub>0.4</sub>Sb<sub>1.6</sub>Te<sub>3</sub> nanocomposites (a) milled at full time, half time, last 1hr, and last 5min of overall 16hr. The Effect of graphene milling time on average grains size (in blue) and microscopic lattice strain (in green) of 0.05wt% Graphene/Bi<sub>0.4</sub>Sb<sub>1.6</sub>Te<sub>3</sub> nanocomposites (b) based on the integral breadth analysis on their XRD patterns using Warren-Averbach method.

Moreover, Figure 4.2 (b) shows the calculated average grain size and lattice strain for the nanocomposite BiSbTe/graphene as a function of milling time. There is a clear growth in grains size appears gradually as the addition of graphene filler is delayed to short milling times, particularly at the last 1hr and 5mins of overall 16hr of milling with BiSbTe matrix. Interestingly, this resulted in the initiation of structural formation of BiSbTe/Graphene nanocomposites, as observed from Figure 4.2 (b). Thus, the average grains size of the nanocomposite where the graphene was added in the last 5mins is 20nm, which is between the 16nm for BiSbTe matrix and 27nm for graphene filler. Whereas, the grains size of the nanocomposite when the graphene is added for 16hr is 12nm with the highest lattice strain of 0.31% indicating the low crystallinity, high imperfections, and destruction of nanocomposite constituent's nanostructure.

It's worth mentioning that the Warren-Averbach method shows the best-fitting linear regression model to all of the recognized diffraction peaks in XRD patterns of either BiSbTe nanopowders or BiSbTe/Graphene nanocomposites, as illustrated in Figure 4.3. This resulted in higher  $R^2$  values of their linear trendlines to be always around 1, which confirms the precision of the drawn and reported conclusions on average grains size and microscopic lattice strains of synthesized specimens.

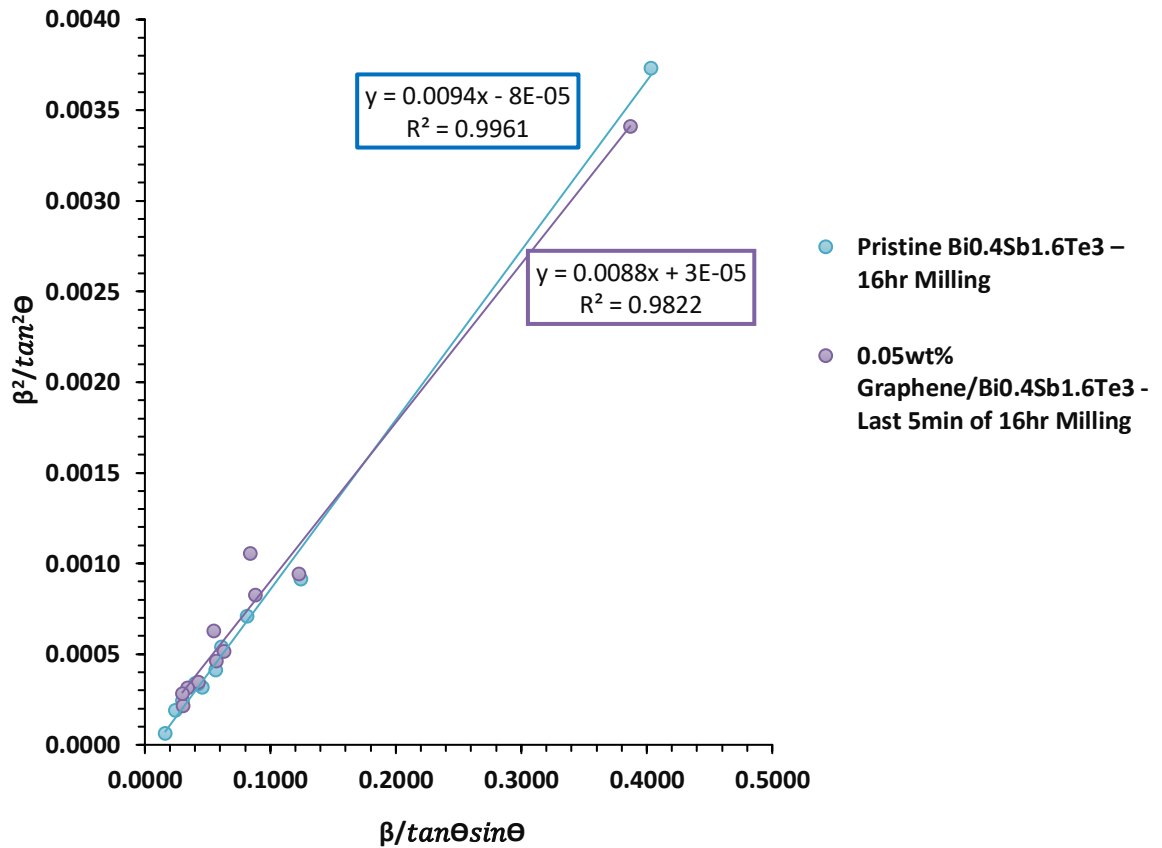


Figure 4.3 The Comparative linear regressions on the pristine BiSbTe at 16hr milling and the 5mins milled nanocomposite based on the integral breadth analysis on their XRD patterns using the Warren-Averbach method for precise calculations of their grain size and lattice strain.

#### 4.1.3 TEM Analysis of the Pristine and the Nanocomposites Samples

The TEM analysis shows the formation of homogenous elemental distributions within the synthesized single phase in 16hr milled Bi<sub>0.4</sub>Sb<sub>1.6</sub>Te<sub>3</sub> nanopowder and 5mins milled Bi<sub>0.4</sub>Sb<sub>1.6</sub>Te<sub>3</sub>/Graphene nanocomposite, as displayed in Figures 4.5 (b) and (e), respectively. These figures represent their high-resolution dark-field (DF) TEM micrographs in which it is clearly observable that there are uniform grain size and distribution without noticing the presence of agglomerated nanocrystallites. This

confirms the homogenous solubility of BiSbTe during the milling process without undergoing welding, which is the main drawback of mechanical milling technique in synthesizing nanostructured materials [157].

Interestingly, the statistical analysis on DF-TEM micrographs confirms the agreement of the average grain size for the pristine BiSbTe nanopowder at 16hrs of milling and the 5min BiSbTe/Graphene nanocomposite with their XRD outcomes, as displayed in Figures 4.5 (c) and (f), respectively. The average grain size in the pristine BiSbTe nanopowder is found to be 18nm calculated from 413grains. Whereas, for the 5mins nanocomposite, the average grain size calculated from 255 grains is 32nm. It is noticeable from the Selected Area Diffraction Pattern (SADP) that the observed nanograins in the high-resolution bright-field (BF) TEM micrographs appear to be equiaxed in random orientations, which match their diffraction profile in the XRD patterns, as illustrated in the upper right insets of Figures 4.5 (a) and (d).



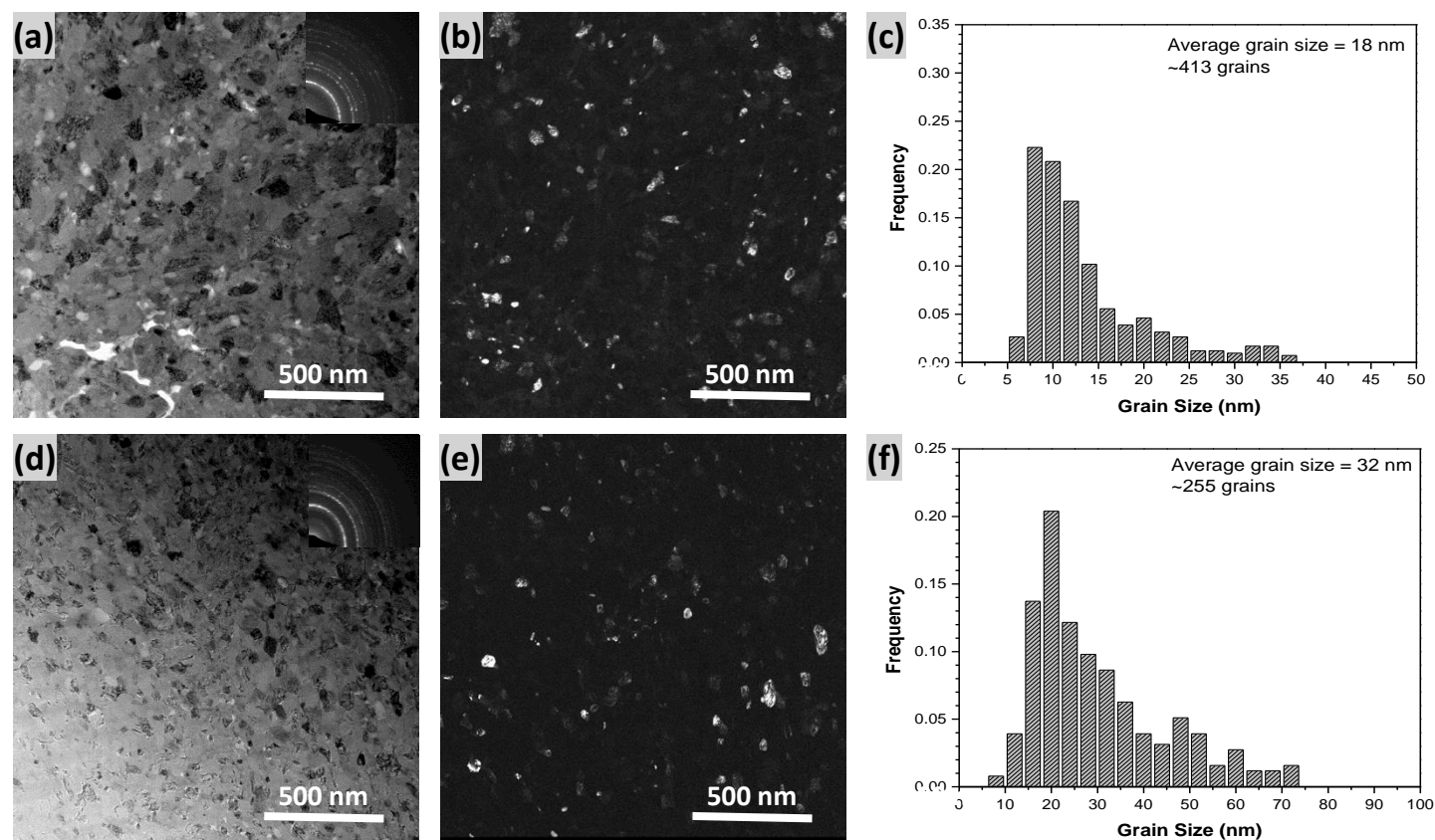


Figure 4.4 The HR-TEM observations of typical nanostructures in pristine  $\text{Bi}_{0.4}\text{Sb}_{1.6}\text{Te}_3$  nanopowder synthesized at 16hr of milling via its bright (a) and dark (b) field TEM micrographs. The upper right inset in (a) is the SADP and shows the equiaxed nanograins in random orientations. A similar nanostructure is observed in 0.05wt% Graphene/BiSbTe nanocomposite synthesized at last 5min of overall 16hr milling as shown in its bright (d) and dark (e) field TEM micrographs and upper right inset in (d) is its SADP. The statistical grain size distribution plots of pristine BiSbTe nanopowder and 0.05wt% Graphene/BiSbTe nanocomposite are shown in (e) and (f), respectively.

Furthermore, it is recognized and reported for the first time (to the best of our knowledge) the presence of a twinning interfacial defect in the BiSbTe/Graphene nanocomposites, as illustrated in Figure 4.6 (b). This figure represents the SADP of the selected area shown in the high-magnification BF-TEM micrograph of the pre-synthesized 5mins nanocomposite, as displayed in Figure 4.6 (a). This diffraction pattern demonstrates evidently the lattice symmetry of its nanocrystals, which appear as mirror reflections to each other, hence matching the nanostructure of the twinning [158]. These atomic reflections are due to the atomic displacements in the  $\text{Bi}_{0.4}\text{Sb}_{1.6}\text{Te}_3$  nanocrystals across a common twinning plane. In such displacements, there is no resultant disorder in the atomic arrangements across the twinning boundary that separates the twinned nanocrystals, which distinguish it from the other 2D planar defects, particularly grain boundaries [158].

Additionally, this interfacial planar defect has probably resulted from the shear deformation during the mechanical milling process of the pre-synthesized nanocomposite [158]. The magnitude of atomic displacements during this deformation is proportional to the distance of the atom from the twinning plane [158]. The presence of twinning could affect the electrical conductivity and mechanical strength of the synthesized TE specimens, as frequently reported [159]. Thus, it must be taken into considerations during the analysis of TE performance for the synthesized nanocomposites.

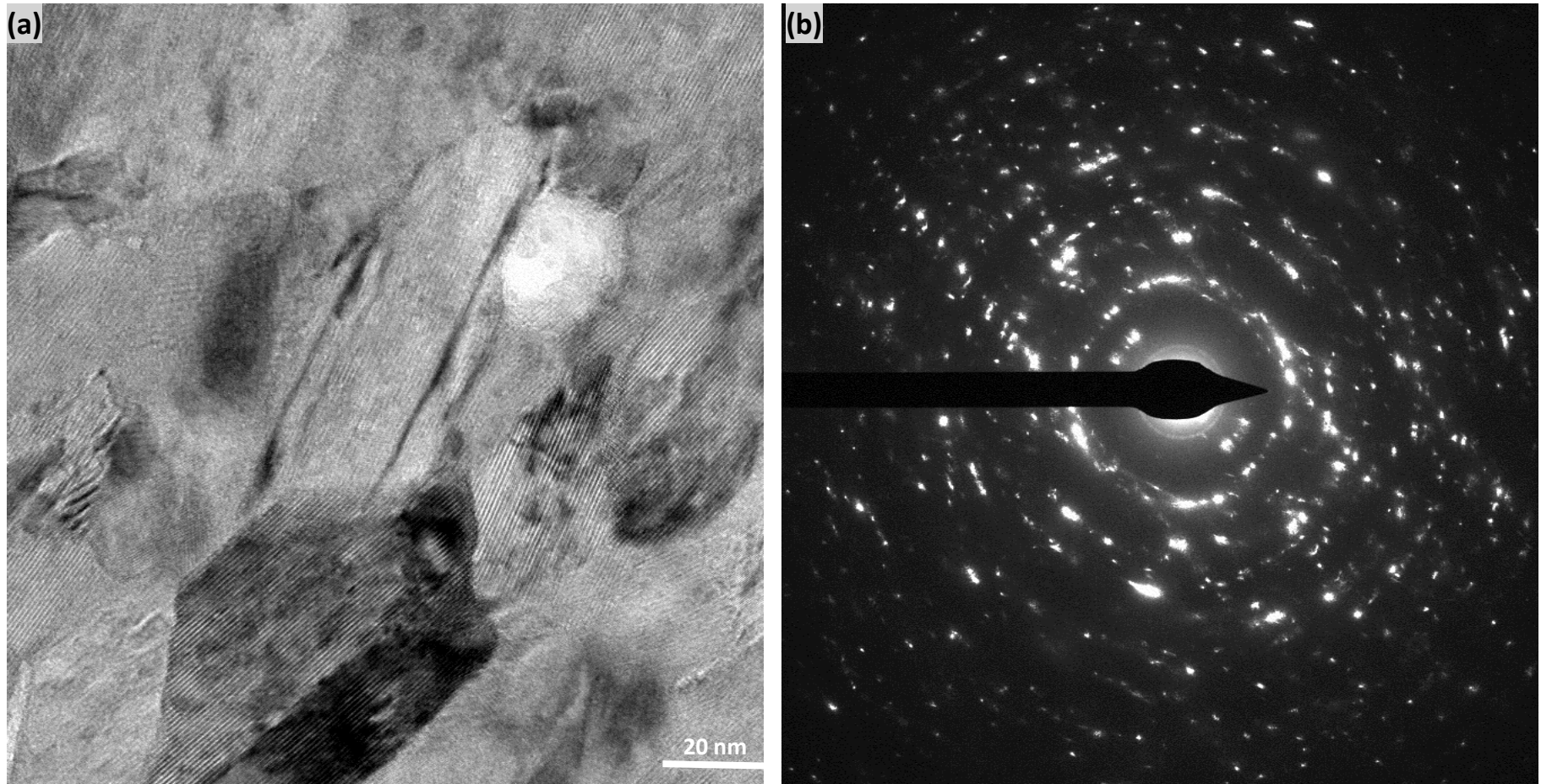


Figure 4.5 The Recognition of twinning interfacial defect in the 0.05wt% Graphene/Bi<sub>0.4</sub>Sb<sub>1.6</sub>Te<sub>3</sub> nanocomposite synthesized at the last 5min of overall 16hr milling as illustrated in its high-magnification bright-field TEM micrograph (a) and SADP (b). It is clear in the SADP (b) that the nanocrystals on either side are the mirror images of the other side.

## 4.2 SPS Consolidation

### 4.2.1 Thermal Analysis of the Pristine and the Nanocomposites Samples

The thermal behavior of the synthesized TE specimens has been studied via the DSC analysis. This powerful thermal analysis technique has inspected precisely their thermodynamic parameters including the phase transition temperatures, enthalpies, and eutectic transitions. These key parameters play a crucial role in identifying the proper sintering temperature to avoid grain growth of the nanostructures, which lead to deteriorations of mechanical properties and TE performance. The drop of grain boundaries, which act as barriers for dislocations motion will lower the hardness of bulk TE pellets leading to lower reliability and shorter service time. This could also result in the increase of thermoelectrical conductivity; as it relies on grain boundaries to increase the phonon-boundary scattering mechanism in nanostructured TE modules.

The procedure of the DSC analysis of the synthesized nanopowders has undergone two continuous heating and cooling cycles at a constant heating rate of 10°C/min in a temperature range of 30-430°C under inert Argon atmosphere. The resultant heat flow curves of these samples are shown in Figure 4.11 (a). As can be seen from this figure, only an endothermic peak was observed for all samples with an onset temperature of 414°C. This phase transformation peak represents the melting of the eutectic phase Bi<sub>2</sub>Te<sub>3</sub> [166]. The formation of this second phase proves the conversion of Bi<sub>0.4</sub>Sb<sub>1.6</sub>Te<sub>3</sub> intermetallic compound into a mixture of two distinct phases, hence the sintering temperature was kept at a lower temperature of 280°C. However, the absence of any other peaks indicates the negligible nanograin growth and insufficient phase separation during the two continuous heating cycles of TE specimens in high-temperature ranges (300-700K) beyond their operating temperature ranges (<400K), which gives an extra advantage of safe in operation.

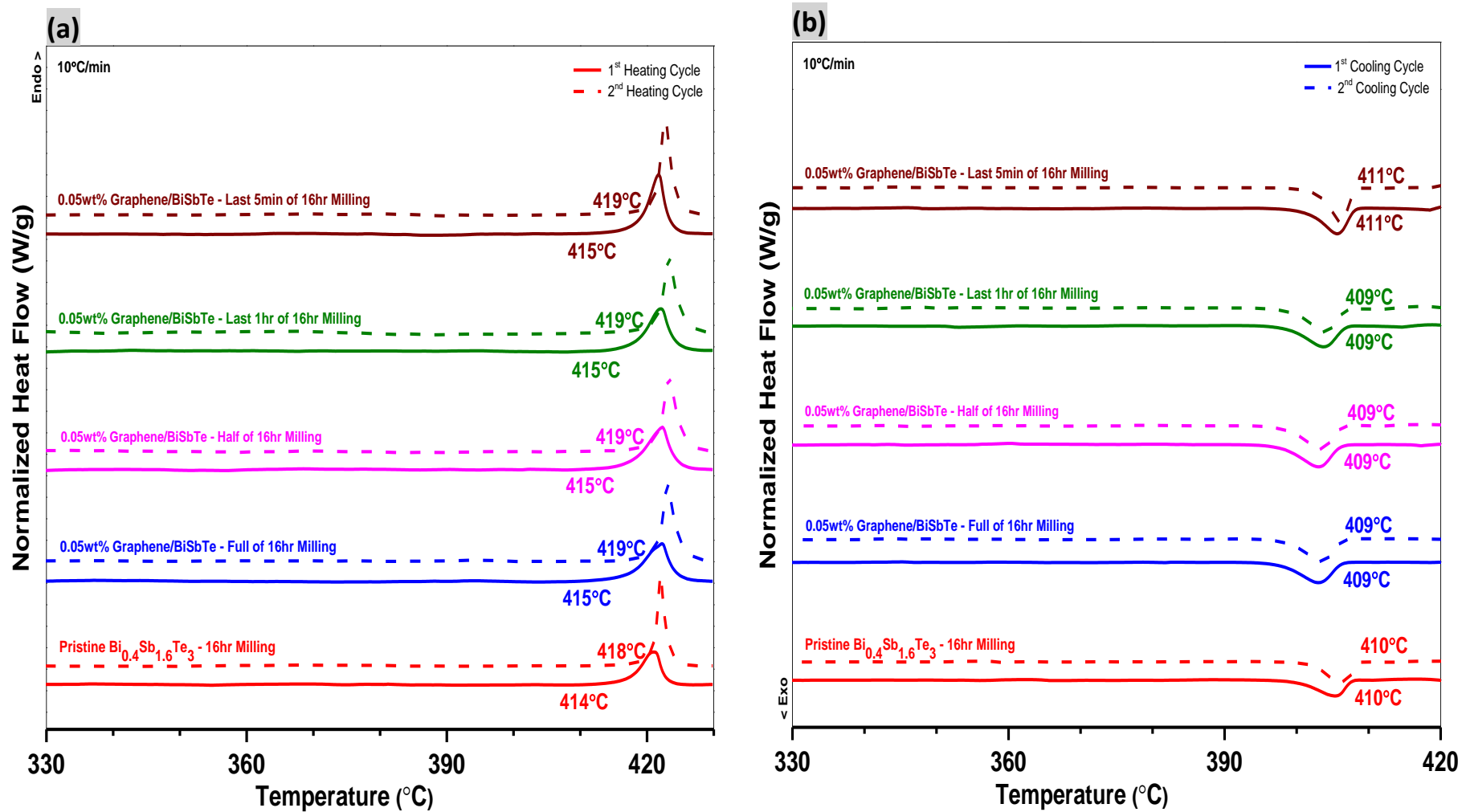


Figure 4.6 The DSC heating curves (a) and cooling curves (b) with the onset temperatures for melting and crystallization peaks for two continuous thermal cycles conducted at a constant heating rate of  $10^\circ\text{C}/\text{min}$  on the pristine  $\text{Bi}_{0.4}\text{Sb}_{1.6}\text{Te}_3$  nanopowder at 16hr milling and 0.05wt% Graphene/ $\text{Bi}_{0.4}\text{Sb}_{1.6}\text{Te}_3$  nanocomposites.

Additionally, the second heating cycle shows a slight shift of  $\pm 5^\circ\text{C}$  on the onset temperatures of the pristine  $\text{Bi}_{0.4}\text{Sb}_{1.6}\text{Te}_3$  and 0.05wt% Graphene/ $\text{Bi}_{0.4}\text{Sb}_{1.6}\text{Te}_3$  nanocomposites. This narrow difference in initiating the endothermic phase transformation could indicate the high thermal stability of synthesized TE specimens under multiple heating cycles. This fulfills the adopted design criteria in this research towards synthesizing advanced TE modules for reliable service, safe operation, and sustainable TE energy. On the other hand, the first and second cooling cycles show similar onset temperatures for an exothermic phase transformation of the molten nanopowders at  $\sim 410^\circ\text{C}$ , as demonstrated in Figure 4.11 (b). This onset temperature of the crystallization process is closer to their onset temperatures of melting in the heating cycles with a minor difference of  $\pm 5^\circ\text{C}$ .

The pristine  $\text{Bi}_{0.4}\text{Sb}_{1.6}\text{Te}_3$  and 0.05wt% Graphene/ $\text{Bi}_{0.4}\text{Sb}_{1.6}\text{Te}_3$  nanocomposites have similar thermal behavior and matching onset temperatures, as shown in Figures 4.11 (a) and (b). This is due to the small content of graphene (0.05wt%) to avoid the effect of its high thermal conductivity on the thermal stability of the multicomponent nanocomposites. This coincides also with their homogenous elemental distribution and stable single phase of  $\text{Bi}_{0.4}\text{Sb}_{1.6}\text{Te}_3$ , which is verified from their HAADF-STEM images and EDS elemental mapping analysis, as shown in Figure 4.12. This could maximize the isotropic performance of synthesized TE modules towards efficient TE energy conversion [167].

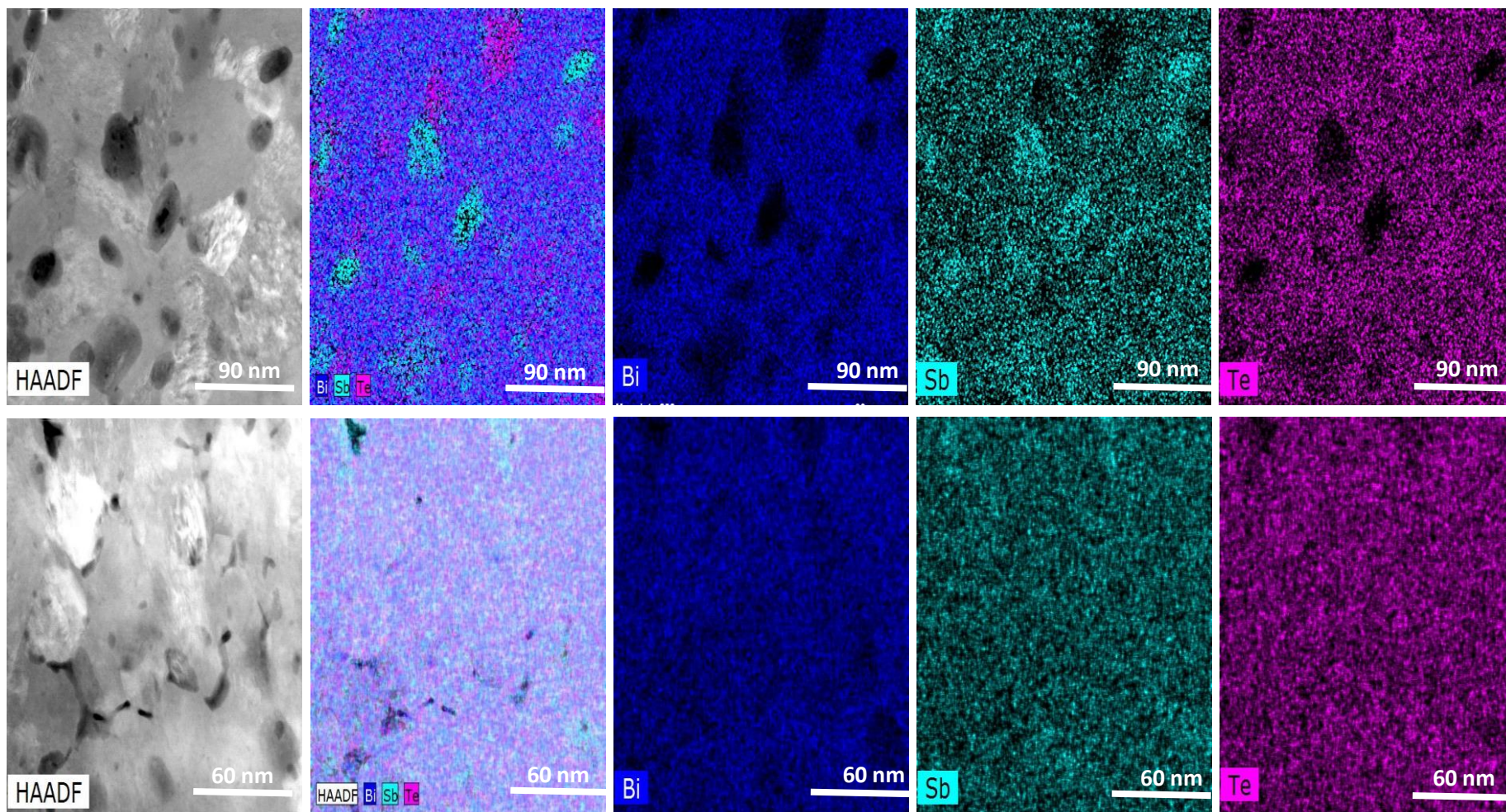


Figure 4.7 The HAADF-STEM images and their corresponding EDS elemental mapping analysis on Bismuth (Bi), Antimony (Sb), and Tellurium (Te) atoms distribution in the pristine  $\text{Bi}_{0.4}\text{Sb}_{1.6}\text{Te}_3$  nanopowder synthesized at 16hr of milling (top row) and 0.05wt% Graphene/ $\text{Bi}_{0.4}\text{Sb}_{1.6}\text{Te}_3$  nanocomposite synthesized at the last 5min of overall 16hr milling (bottom row).

However, the thermal decomposition of  $\text{Bi}_{0.4}\text{Sb}_{1.6}\text{Te}_3$  at  $414^\circ\text{C}$  has destroyed the homogeneity of the elemental distributions in TE specimens. Thus, stimulating the formation of second phase rich in Te, which in turn varied the normalized heating and cooling enthalpies for first and second heating cycles, as displayed in Figure 4.13. These variations are negligible as it is in narrow ranges of  $\pm 0.5\text{J/g}$  and referred to the small volume fraction of the formed second phase from Te-phase separation in the first heating cycle. This small rise in the enthalpies of the second heating and cooling cycles indicates the high strength of  $\text{Bi}_{0.4}\text{Sb}_{1.6}\text{Te}_3$  atomic interactions and their remarkable thermal stability.

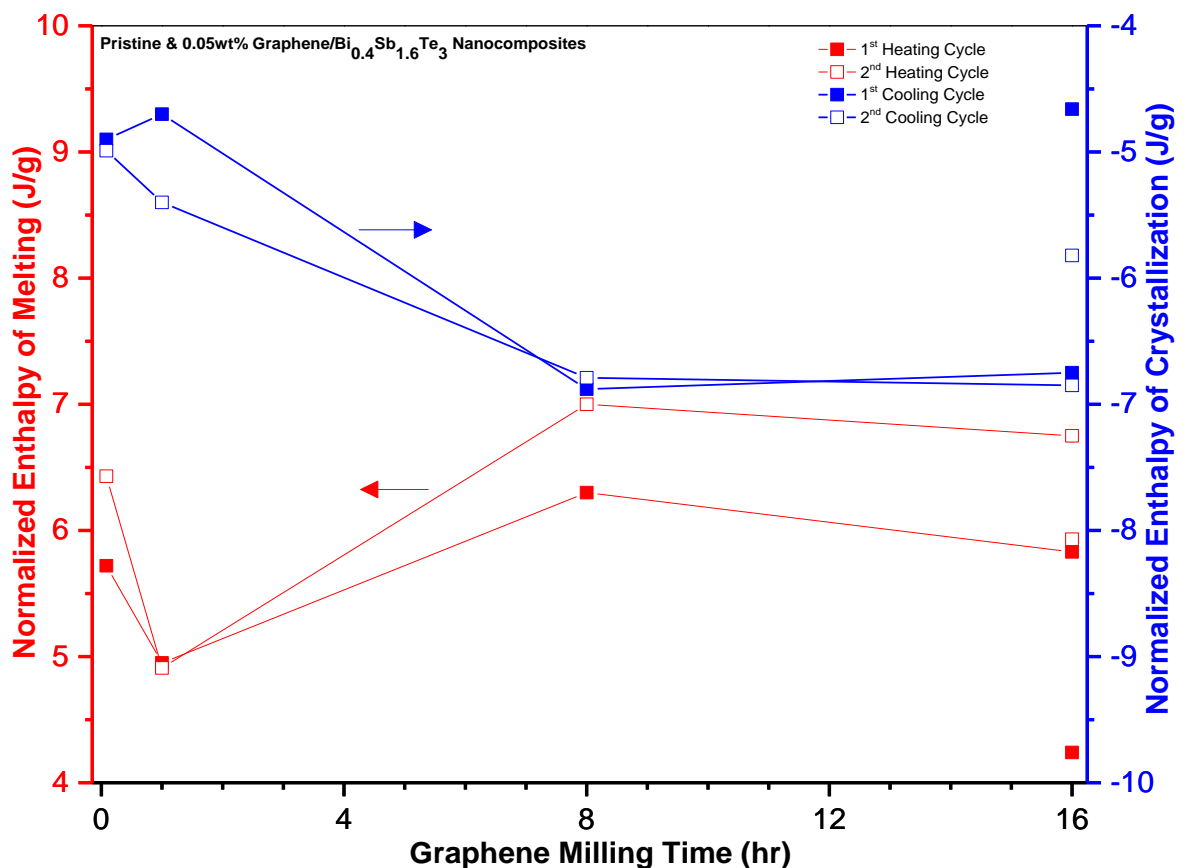


Figure 4.8 The Effect of graphene milling time on the normalized enthalpies of melting (in red) and crystallization (in blue) for two continuous thermal cycles



conducted at a constant heating rate of 10°C/min on pristine Bi<sub>0.4</sub>Sb<sub>1.6</sub>Te<sub>3</sub> nanopowder at 16hr milling (non-linked squares) and 0.05wt% Graphene/Bi<sub>0.4</sub>Sb<sub>1.6</sub>Te<sub>3</sub> nanocomposites (linked squares).

#### **4.2.2 Structural Analysis of the Consolidated Samples**

The XRD analysis has been conducted on the sintered pellets of the pre-synthesized pristine BiSbTe at 16hrs of milling and BiSbTe/Graphene nanocomposites, as illustrated in Figure 4.4 (a). This figure shows their match-up in diffraction profiles with the appearance of a couple of new and low-intensity peaks recognized at  $2\theta$  of 26.23°, 33.56°, and 40.44° corresponding to the indexed crystal planes of (009), (018), and (0111), respectively. The presence of the diffraction plane indexed with (009) is a fingerprint in the XRD patterns of artifact-free bulk nanostructured pellets of BiSbTe and graphene [155]. This diffraction peak appears in low intensity of 1.96% in all the synthesized nanocomposites except the 5mins nanocomposite. In which it is well observable in a higher intensity of 5.68% and in an equivalent diffraction angle to graphene nanoplatelets at the plane of (002), as shown in Figure 4.4 (a). This quite small intensity is a resultant of the small filler content of 0.05wt.% being composited with the BiSbTe nanocrystals.

It is worth mentioning that the appearance of these new diffraction peaks is a common consequence of nanopowder consolidation via the SPS technique, as frequently reported [156]. This is referred to the growth of grains and reduction of the residual strains during the sintering of the nanopowders at relatively high temperatures of 280°C [156]. However, this sintering process has not affected considerably grain growth in the SPS pellets due to the absence of high residual strains in their

nanopowders. Thus, the average grains size and microscopic lattice strains of the SPS pellets have not dramatically varied from their nanopowders, as displayed in Figure 4.4 (b). This figure indicates the gradual decrease in the grain size of bulk nanocomposites from 30nm to 22nm for full time and last 5mins milled nanocomposites, respectively. It is noticed also that the grain growth in the 5mins milled nanocomposite is just 1nm, hence sustaining the grain size refinement. Whereas, the full-time milled nanocomposite shows 18nm growth in its average grain size due to the initially high residual strains of 0.31% in its nanopowder.

On the other hand, there is a parallel decrease in the microscopic lattice strain to the average grain size, as illustrated in Figure 4.4 (b). This trend confirms the successfulness in synthesizing artifact-free bulk nanocrystalline BiSbTe composited with 0.05wt.% Graphene at the last 5mins of the overall 16hrs of continuous mechanical milling. The resultant sintered pellet shows a drop of its residual strain from 0.22% to 0.14%, while retaining the grain size refinement of 22nm.

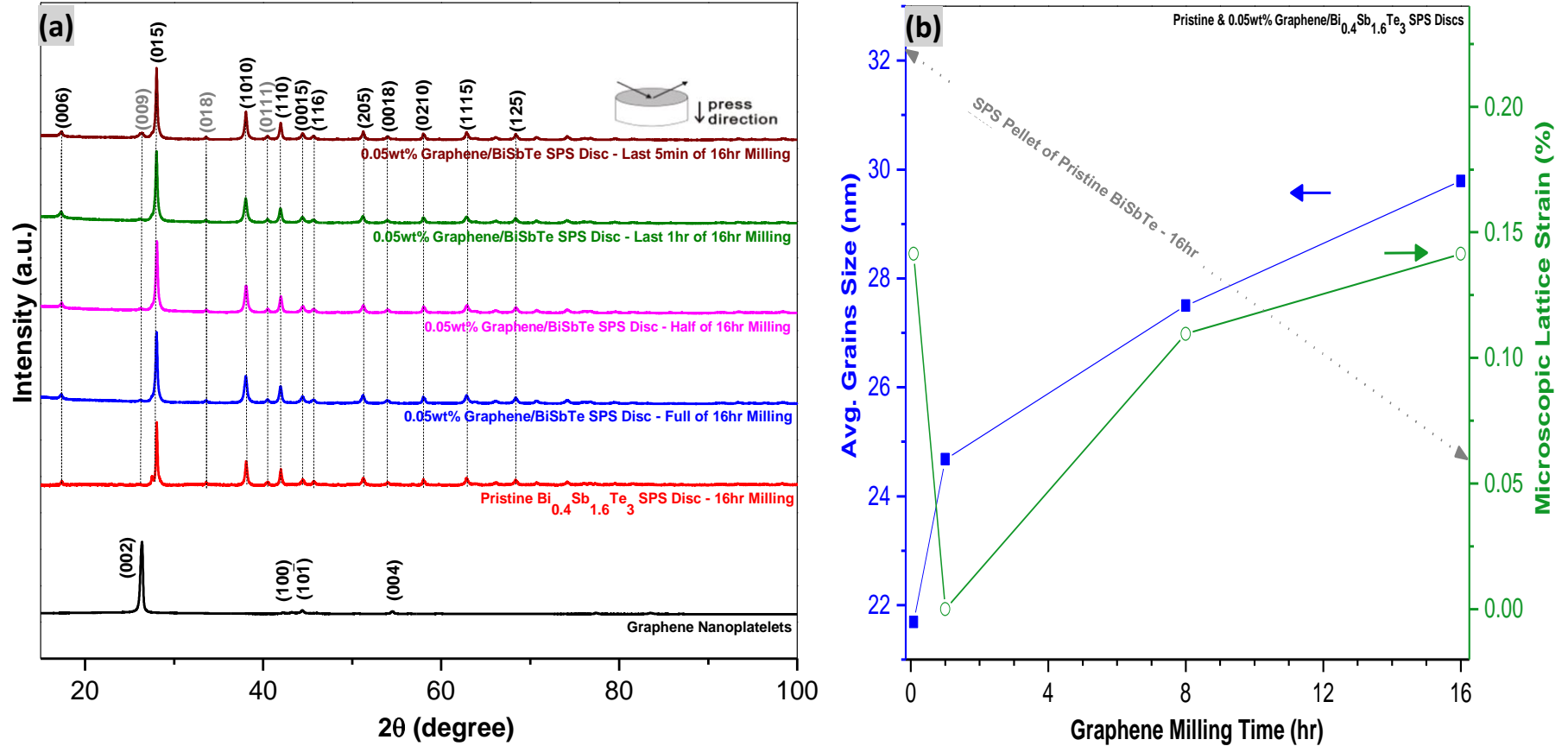


Figure 4.9 The XRD patterns of sintered pellets for pristine BiSbTe and 0.05wt% Graphene/BiSbTe nanocomposites (a) milled at full time, half time, last 1hr, and last 5min of overall 16hr. The top inset shows in-plane surface of as-pressed disc perpendicular to its SPS pressing. The Effect of graphene milling time on average grains size (in blue) and microscopic lattice strain (in green) of sintered pellets for pristine and nanocomposites (b) based on integral breadth analysis on their XRD patterns using Warren-Averbach method.

### 4.3 Mechanical Characterization

#### 4.3.1 Mechanical Properties of the Pristine $\text{Bi}_{0.4}\text{Sb}_{1.6}\text{Te}_3$ Nanopowders

The mechanical behavior of the synthesized  $\text{Bi}_{0.4}\text{Sb}_{1.6}\text{Te}_3$  nanocrystals has been analyzed using the Vickers micro-hardness tester. This advanced technology characterizes precisely the resistance of synthesized specimens to localized surface deformation in terms of Vickers micro-hardness ( $H_v$ ) [159]. This characterization is crucial for TE device integrity and reliable operation to withstands the mechanical stresses [159]. Accordingly, the synthesized nanocrystals show a gradual increment in their average Vickers micro-hardness values with prolonging the milling times, as displayed in Figure 4.7. This mechanical behavior is consistent with the Hall-Petch (H-P) relationship in which the nanostructured materials are characterized with multiple grain boundaries that obstruct the dislocations motion and then hardening the material [160]. Thus, the synthesized  $\text{Bi}_{0.4}\text{Sb}_{1.6}\text{Te}_3$  nanocrystals have reached an ultrahigh hardness value of 1.30GPa with an ultralow average grains size of 16nm after 16hrs of high energy milling, as shown in Figure 4.7.

This hardness value is the highest reported to our knowledge for such TE system and denotes the effectiveness of synthesizing the intermetallic  $\text{Bi}_{0.4}\text{Sb}_{1.6}\text{Te}_3$  with ultrafine nanostructure at optimized synthesizes conditions using the mechanical milling process. However, the initiation of the plateau region in the average micro-hardness values is observed for excessive milling times exceeding the 16hrs, as shown in Figure 4.7. This further confirms that 16hrs of milling is enough for synthesizing  $\text{Bi}_{0.4}\text{Sb}_{1.6}\text{Te}_3$  nanocrystals with exceptional hardness and nanostructure.

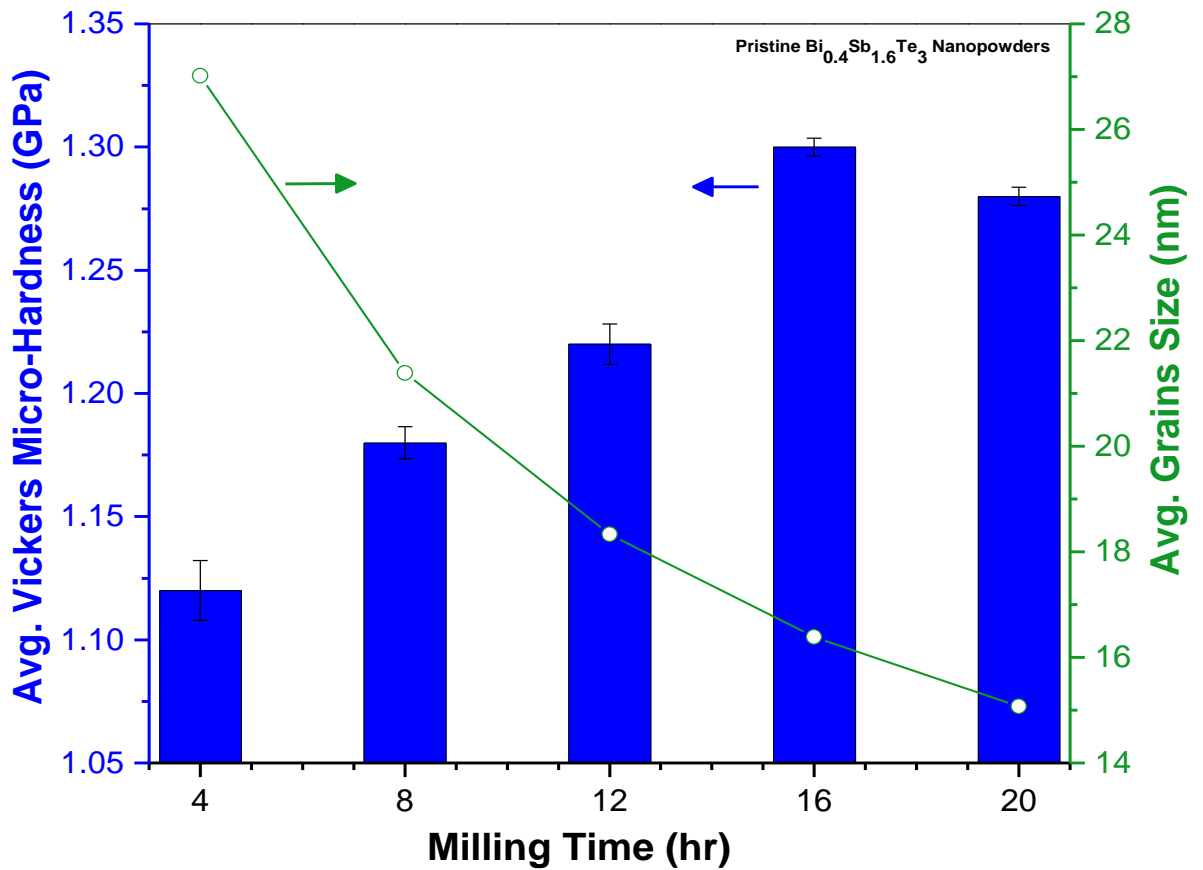


Figure 4.10 The Effect of milling time on the average Vickers micro-hardness (in blue) and average grain size (in green) of pristine  $\text{Bi}_{0.4}\text{Sb}_{1.6}\text{Te}_3$  nanopowders.

#### 4.3.2 Mechanical Properties of the Graphene/ $\text{Bi}_{0.4}\text{Sb}_{1.6}\text{Te}_3$ Nanocomposites

The mechanical behavior of the pre-synthesized  $\text{Bi}_{0.4}\text{Sb}_{1.6}\text{Te}_3$  nanocrystals has undergone remarkable improvements after compositing with graphene nanoplatelets. This is referred to the unique 2D nanostructure of graphene nanoplatelets, which resulted in its ultimate hardness of 6.80GPa [162]. Consequently, the average micro-hardness values of the synthesized nanocomposites have overcome the pristine  $\text{Bi}_{0.4}\text{Sb}_{1.6}\text{Te}_3$  nanopowder synthesized at 16hrs of milling, as shown in Figure 4.8. This enhancement is optimum in the 5mins nanocomposite with the uppermost hardness of 1.78GPa at an average grains size of 20nm. This achievement is much higher than the

hardness values of single and ingot  $\text{Bi}_{0.4}\text{Sb}_{1.6}\text{Te}_3$ , which are in the average of 0.60GPa and 0.57GPa, respectively [163,164]. This is due to the fine grain structure of the synthesized 5min nanocomposite, which is in good agreement to the pre-observed evolutions in its crystallinity and nanostructure. However, increasing the graphene content beyond 0.05wt% will enhance further the hardness of Graphene/ $\text{Bi}_{0.4}\text{Sb}_{1.6}\text{Te}_3$  nanocomposite. This enhancement is a trade-off approach in which the ZT values will be lowered dramatically due to the high thermal conductivity of graphene, hence contradicting the design standards of TE modules (see section 2.5.1 in chapter 2 for details).

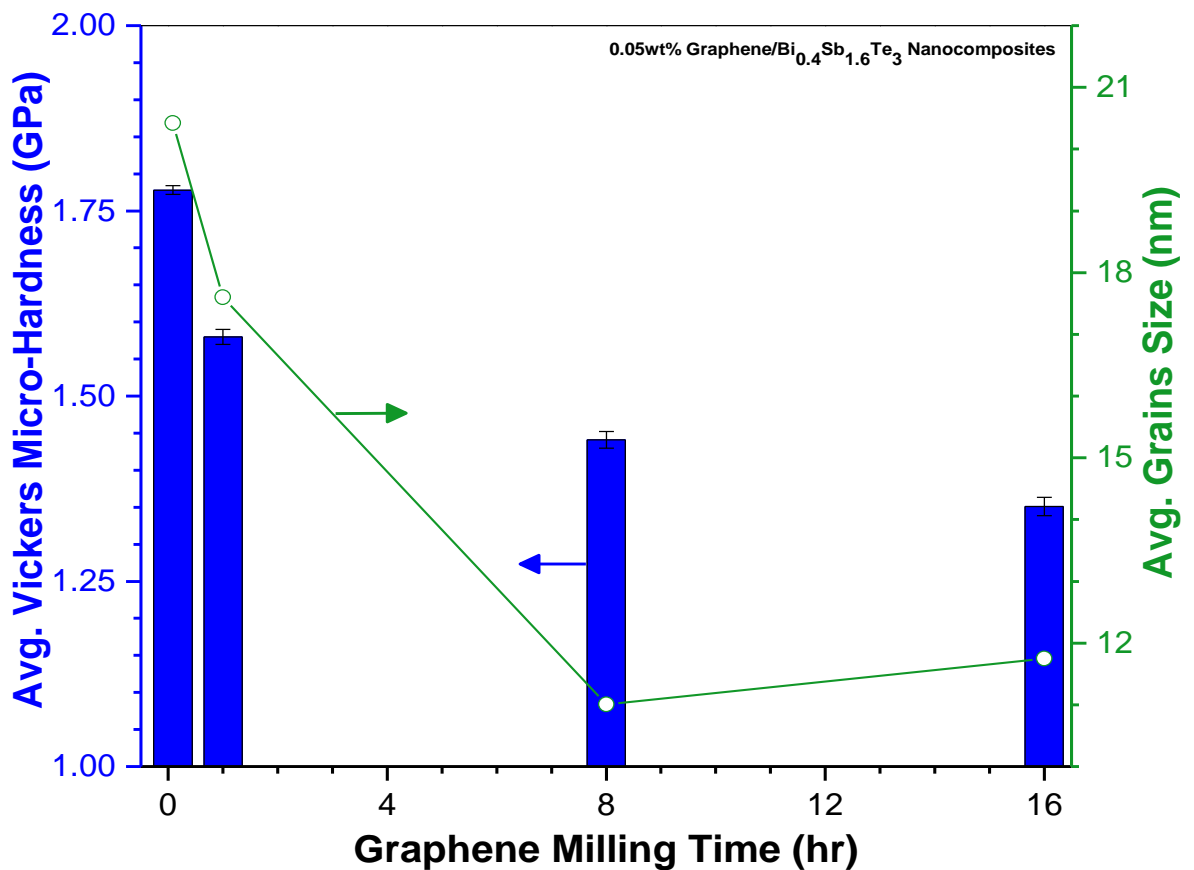


Figure 4.11 The Effect of graphene milling time on average Vickers micro-hardness (in blue) and average grain size (in green) of Graphene/ $\text{BiSbTe}$  nanocomposites.

The outstanding mechanical behavior of the synthesized nanocomposites is consistent with the nanostructure evolution of graphene nanoplatelets, as displayed in Figure 4.9 (a). This figure shows the Raman spectra at standard DXR laser excitation of 532nm to investigate the morphology of graphene in the reference powder (raw graphene nanoplatelets) and synthesized nanocomposites. This investigation is quantified in a reliable manner based on calculations of the intensity ratio between the 2D band to G band ( $I_{2D}/I_G$  ratio) from their Raman spectra. The outcomes of  $I_{2D}/I_G$  ratio calculations confirm the crucial role of graphene addition time on its structure, as well as, the morphology and mechanical behavior of the synthesized nanocomposites, as shown in Figure 4.9 (b). This figure demonstrates the gradual transition trend in number of graphene layers from multi-, few-, to the single-layered structure. The multi-layered graphene appears in full-time (added initially and undergone 16hrs of milling) and half-time (added after 8hrs and undergone 8hrs of milling) nanocomposites. This multi-layered structure is referred to the excessive milling of graphene due to its addition at early milling times, which in return affected its unique 2D integrity.

The addition of graphene into the last hour of the overall 16hrs milling time resulted in few-layered graphene. This structural transition has also shifted to single layered graphene after its addition at the last 5mins of the overall 16hrs milling time [165]. This could be the reason for the exceptional mechanical behavior and nanostructure of the synthesized 5mins nanocomposite. The delayed addition times of graphene to  $\text{Bi}_{0.4}\text{Sb}_{1.6}\text{Te}_3$  nanopowder is favored as it shortens its milling duration, hence preserving its 2D nanostructure and advantaging its exceptional properties. It is worth pointing out that this is the first time (to the best of our knowledge) to observe and report the transition trend in graphene layered structure to its milling duration in promising TE system as  $\text{Bi}_{0.4}\text{Sb}_{1.6}\text{Te}_3$ .

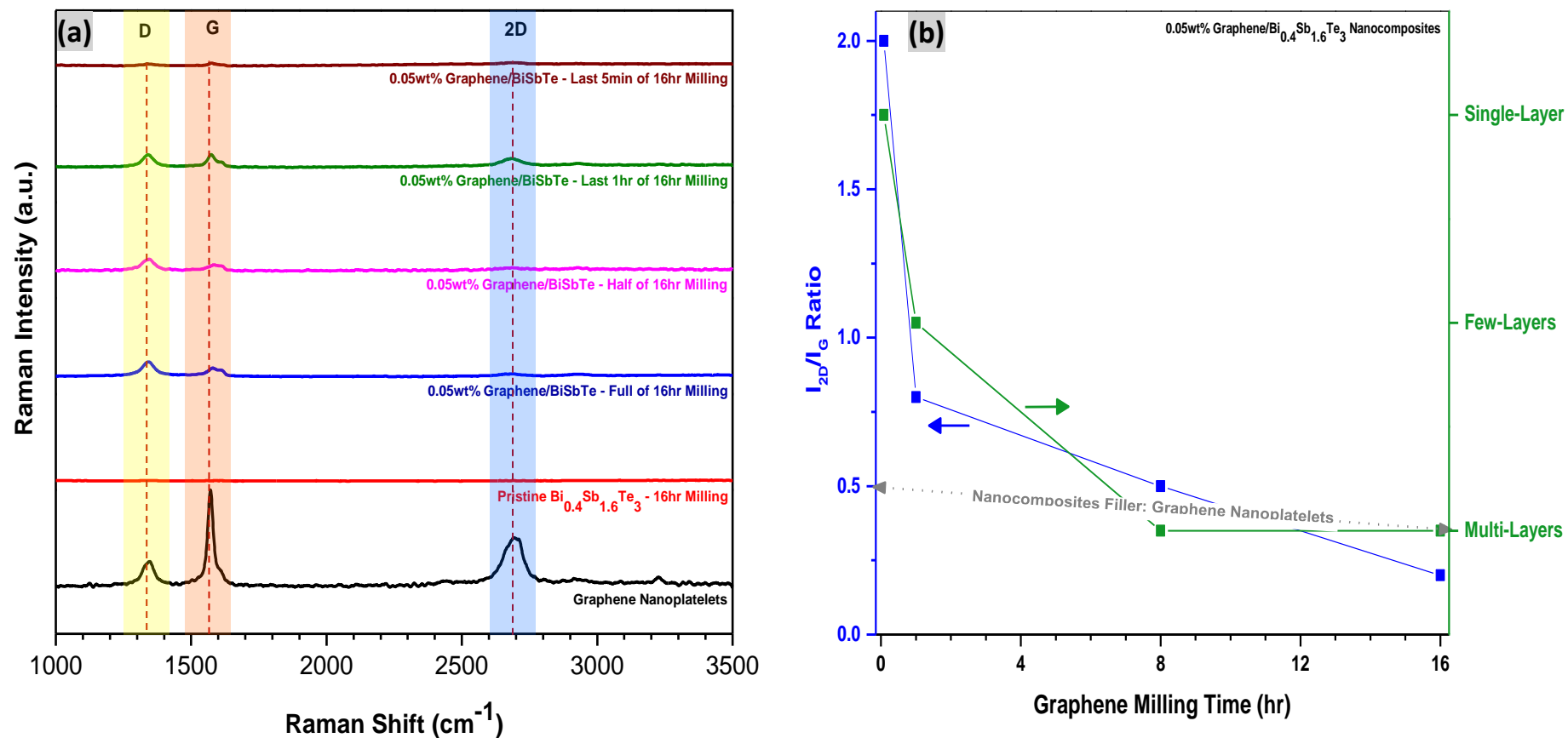


Figure 4.12 The Raman spectra of the reference graphene nanoplatelets, 16hr milled pristine Bi<sub>0.4</sub>Sb<sub>1.6</sub>Te<sub>3</sub> nanopowder, and 0.05wt% Graphene/Bi<sub>0.4</sub>Sb<sub>1.6</sub>Te<sub>3</sub> nanocomposites (a) at DXR laser excitation of 532nm. The Effect of graphene milling time on the 2D band intensity to G band intensity ratio (I<sub>2D</sub>/I<sub>G</sub> ratio) (in blue) indicates the dramatic change in the number of graphene layers (in green) present in the synthesized 0.05wt% Graphene/Bi<sub>0.4</sub>Sb<sub>1.6</sub>Te<sub>3</sub> nanocomposites (b).



The evolution of Raman spectra including the positions and intensities of G, D, 2D, and D+G bands has been utilized in differentiating graphene from its carbon allotropes (e.g. graphite and carbon nanotubes). Figure 4.10 shows the prominent Raman features of the monolayered graphene sheet in the synthesized 5mins nanocomposite. The Raman profile of this sample reveals distinguishable peaks at around 1345, 1579, and 2692  $\text{cm}^{-1}$  for D, G, and 2D bands, respectively. These peaks are positioned with slight blueshifts of only 3, 8, and 2  $\text{cm}^{-1}$  from the corresponding ones in the reference graphene. However, these shifts are dramatical in the remained nanocomposites, which are pre-characterized with multi- or few-layered graphene. It is also worth noting that a sharp D+G combination peak appears at 2919, 2932, and 2933  $\text{cm}^{-1}$  in the full-time, half-time, and last-1hr milled nanocomposites, respectively. This additional peak denotes the presence of high disorder in the graphene structure and confirms the stacking of its 2D monolayer into other carbon allotropes, particularly the 3D graphite. This coincides with the pre-observations on the number of graphene layers in the synthesized nanocomposites based on their  $I_{2D}/I_G$  ratios.

Additionally, the D-mode signal, which is induced via defects or disorder appears in the lowest intensity in the 5mins nanocomposite [165]. This indicates the high crystallinity of graphene filler and the absence of new structural defects throughout compositing process with  $\text{Bi}_{0.4}\text{Sb}_{1.6}\text{Te}_3$  nanopowder using the ball milling technique. This allows to preserve the large surface area of the monolayer graphene and then strengthens its interfacial interactions with  $\text{Bi}_{0.4}\text{Sb}_{1.6}\text{Te}_3$  nanopowder, which in turn resulted in a stabilized TE nanocomposite with enhanced mechanical behavior for reliable service.

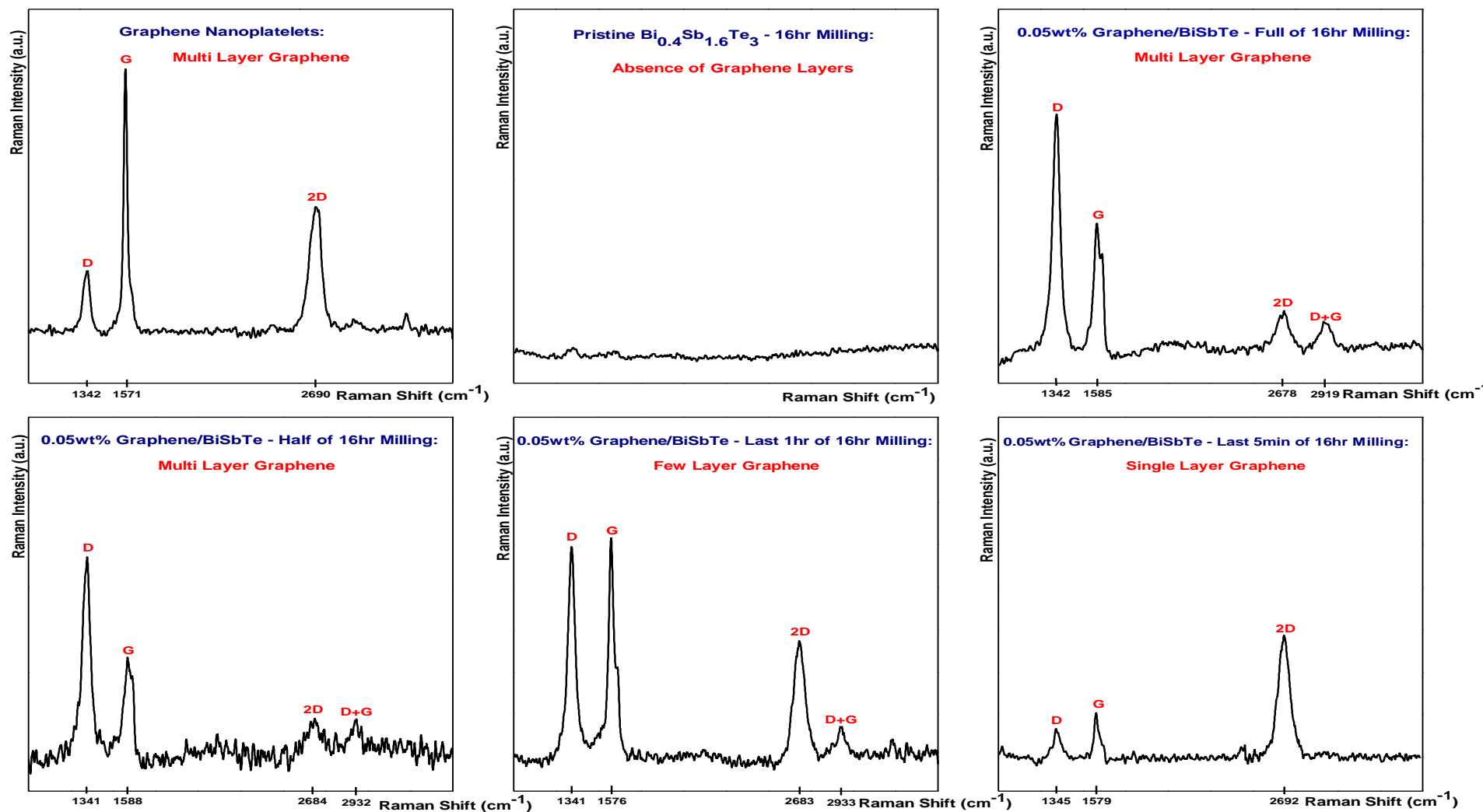


Figure 4.13 The Evolutions of D, G, 2D, and D+G bands in the Raman spectra of the reference graphene nanoplatelets, 16hr milled pristine Bi<sub>0.4</sub>Sb<sub>1.6</sub>Te<sub>3</sub> nanopowder, and 0.05wt% Graphene/Bi<sub>0.4</sub>Sb<sub>1.6</sub>Te<sub>3</sub> nanocomposites at DXR laser excitation of 532nm.

#### 4.4 Thermoelectric Properties

The thermoelectric performance of the synthesized TE specimens has been tested via the SBA-458 and LFA-467 instruments. The practical design of the SBA-458 has permitted simultaneous measurements of the electrical conductivity ( $\sigma$ ) and Seebeck coefficient (S) in the temperature ranges from 323K to 425K, as displayed in Figures 4.14 (a) and (b), respectively. The electrical conductivity of the tested SPS pellets for pristine  $\text{Bi}_{0.4}\text{Sb}_{1.6}\text{Te}_3$  and 0.05wt% graphene/ $\text{Bi}_{0.4}\text{Sb}_{1.6}\text{Te}_3$  nanocomposites show a linear decrease with increasing the temperature. Their common behavior matches the metallic behavior at elevated temperatures due to the increased thermal excitations of lattice vibrations [168]. The lattice vibration increases scattering rates via collisions with crystallographic defects, which in turn obstruct the flow of charge carriers, decrease their mean free path, and reduce their mobility [168]. However, this drop in electrical conductivity is not very sharp as it decreases from 231S/cm at 323K to 209S/cm at 420K for the pristine BiSbTe, as shown in Figure 4.14 (a).

The addition of graphene to the p-type BiSbTe has impressed the electrical conductivity for all samples at different conditions, as shown in Figure 4.14 (a). It is worth mentioning that the electrical conductivity of pristine  $\text{Bi}_{0.4}\text{Sb}_{1.6}\text{Te}_3$  has considerably improved from 231S/cm to 344S/cm at 322K after compositing it with graphene nanoplatelets. This refers to its high charge carrier density and mobility due to owning a unique 2D nanostructure that offers additional charge transmission channels [169].

On the other hand, the positive values of Seebeck coefficient confirm the effectiveness in resonant level doping of Bi-Te system with Sb dopant to form the desired p-type  $\text{Bi}_{0.4}\text{Sb}_{1.6}\text{Te}_3$ , as presented in Figure 4.14 (b). This p-type semiconductor

shows an exponential decay in its Seebeck values as the temperature increases from 323K to 425K. The pristine  $\text{Bi}_{0.4}\text{Sb}_{1.6}\text{Te}_3$  pellet shows the highest Seebeck coefficient values in reverse to its behavior in electrical conductivity. This is due to the inverse and strong interdependence of electrical conductivity and Seebeck coefficient on charge carrier's density as pre-shown in Equations (2.19) and (2.20), respectively.

Accordingly, the power factor ( $S^2\sigma$ ), which is derived from structure-sensitive properties, namely the Seebeck coefficient and electrical conductivity shows a linear temperature dependence, as displayed in Figure 4.14 (c). This figure confirms that the 5mins nanocomposite has the highest power factor of  $1.73\text{mW}/\text{m}\cdot\text{K}^2$  at 324K, which slowly decreased to  $1.40\text{mW}/\text{m}\cdot\text{K}^2$  at 422K. These values are the highest reported (to our knowledge) and overcomes the solution-derived BiSbTe with a maximum of  $9.0\mu\text{W}/\text{cm}\cdot\text{K}^2$  and ternary alloy ingot of  $18.0\mu\text{W}/\text{cm}\cdot\text{K}^2$  [169,170]. This high power factor coincides with its exceptional mechanical behavior. The grain boundaries in its nanostructure have strengthened the energy filtering of minority carriers with low energy. Thus, maximizing its Seebeck coefficient to reach  $225\mu\text{V}/\text{K}$  at 376K, which is higher than that reported for  $\text{Bi}_{0.5}\text{Sb}_{1.5}\text{Te}_3$  pellet produced from solution route ( $168\mu\text{V}/\text{K}$  at 375K) [171]. Additionally, its preserved 2D nanostructure of graphene nanoplatelets due to its shortened milling durations has maximized its electrical conductivity to  $313\text{S}/\text{cm}$  at 376K.

Moreover, the measured thermal conductivity of synthesized SPS pellets shows a linear increase with temperature, as displayed in Figure 4.14 (d). This thermal conductivity is lowest at the 5mins nanocomposite, which increase from  $0.723\text{W}/\text{m}\cdot\text{K}$  at 323K to  $0.815\text{W}/\text{m}\cdot\text{K}$  at 423K. This negligible change in its thermal conductivity over a wide temperature range indicates the influence of graphene in improving its

phonons scatterings. These scatterings occur primarily at nanograins boundaries of the  $\text{Bi}_{0.4}\text{Sb}_{1.6}\text{Te}_3$  and nanointerfaces of the preserved 2D graphene nanoplatelets.

It is worth pointing out that the thermal conductivity values in Figure 4.14 (d) is the total contributions of phonons (lattice thermal conductivity) and charge carriers (electronic thermal conductivity). The phonon contribution is dominant in the degenerated semiconductors and has been quantified via subtracting the measured total thermal conductivity from the calculated electronic conductivity using Wiedemann-Franz law, as pre-shown in Equations (2.10) and (2.12). Consequently, the phonons contribution has been diminished extremely in the 5mins nanocomposite and reached a value of  $0.598\text{W/m.K}$  at  $423\text{K}$ , as displayed in Figure 4.14 (e). This much smaller than the  $0.705\text{W/m.K}$  at  $423\text{K}$  in the pristine  $\text{Bi}_{0.4}\text{Sb}_{1.6}\text{Te}_3$  pellet and confirms the advantage of graphene nanocompositing in providing additional interfaces for maximizing phonons scattering.

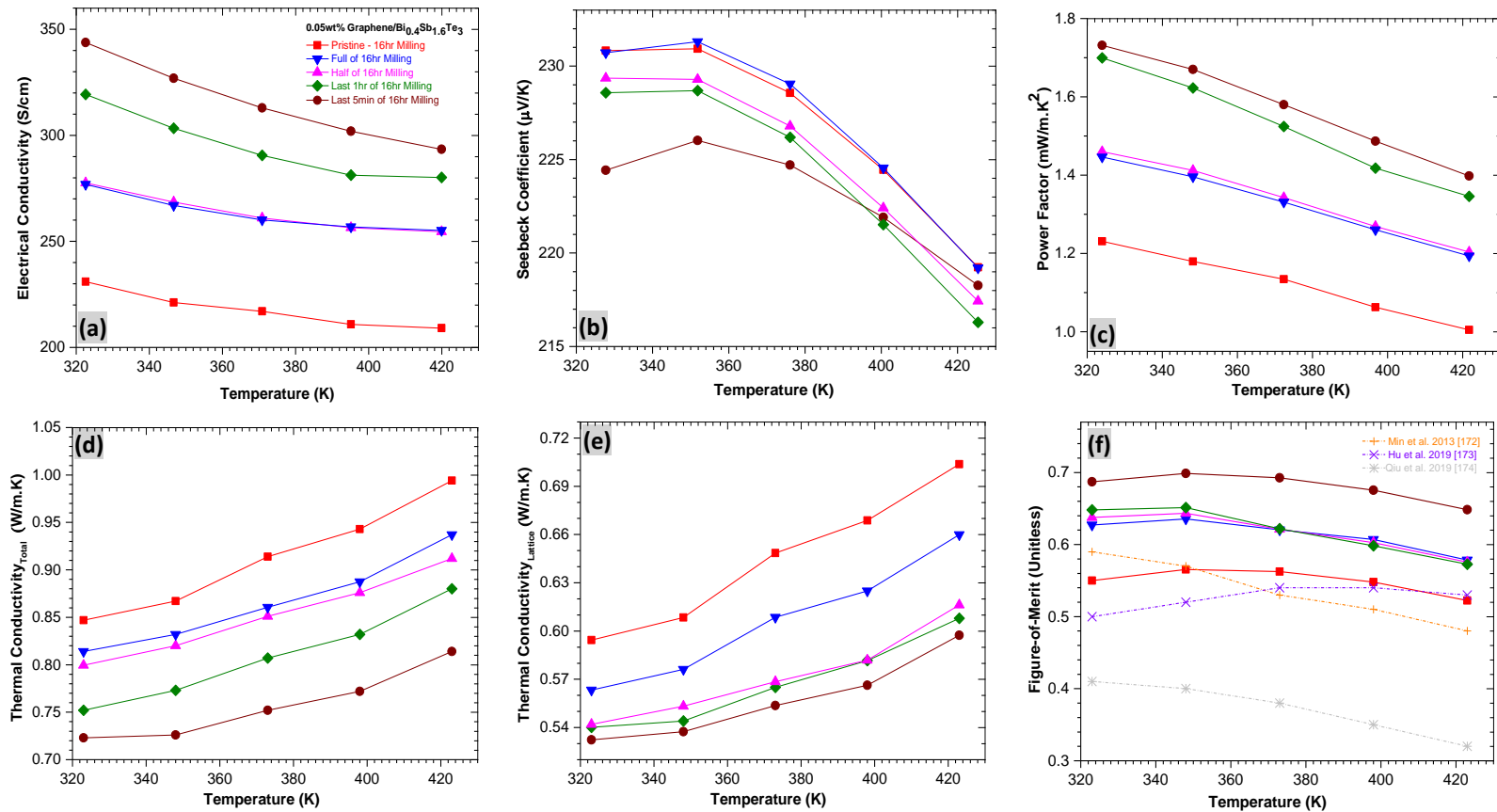


Figure 4.14 The Temperature dependence of thermoelectric parameters: Electrical conductivity (a), Seebeck coefficient (b), Power factor (c), Total thermal conductivity (d), Lattice thermal conductivity (e), and Figure-of-Merit (f) for SPS pellets of the pristine  $\text{Bi}_{0.4}\text{Sb}_{1.6}\text{Te}_3$  at 16hr milling and 0.05wt% Graphene/ $\text{Bi}_{0.4}\text{Sb}_{1.6}\text{Te}_3$  nanocomposites.

As a result, the Figure-of-Merit (ZT) shows a temperature-dependence profile, which has been derived via dividing the power factor of the SPS pellets by their total thermal conductivity using Equation (2.18). Interestingly, the ZT profile shows a considerable enhancement in thermoelectric energy conversion of the 5mins nanocomposite that achieved 0.70 at 323K till 398K, as presented in Figure 4.14 (f). This shows a 25% of improvements to the pristine BiSbTe pellet and 68% to other literatures, particularly at 324K. This TE performance is highly beneficial for several TE applications in Qatar, as the typical room temperatures at its summer weather is near 324K (51°C). This achievement proves also its ability in attaining an isotropic thermoelectric performance over a wide temperature range. This coincides with the pre-observations on its homogenous elemental distribution and stable single phase of its  $\text{Bi}_{0.4}\text{Sb}_{1.6}\text{Te}_3$  matrix. This matching the thesis objectives in sufficiently stabilizing the TE performance of synthesized nanocomposites for reliable service and sustainable energy conversion.

Additionally, the unique electrical and mechanical properties of 2D graphene nanoplatelets have been effectively utilized in upgrading the TE performance of pristine BiSbTe via tuning its addition time to the milling process, as shown in Figure 4.14 (f). Thus, resulting in comparable TE performance to other p-type Bi-Te based TE materials synthesized via different techniques such as laser 3D printing, chemical reactions, and ingot vibration crashing, as displayed in Figure 4.14 (f) [172–174]. This confirms also the optimized processing conditions of the high-energy milling and SPS in synthesizing artifact-free nanostructured bulk BiSbTe/Graphene nanocomposites with isotropic TE performance.

## Chapter 5: CONCLUSIONS & RECOMMENDATIONS

### 5.1 Thesis Research: Conclusions

The effectiveness in the adopted hypothesis of this thesis research towards achieving its objectives on optimizing and stabilizing the p-type BiSbTe/Graphene nanocomposites for efficient TE energy conversion is remarked in the following conclusions:

- The combination of High-Energy Ball Milling and FAST/SPS Sintering Press showed a reliable and cost-effective synthesis approach for artifact-free nanostructured bulk BiSbTe/Graphene nanocomposites.
- The XRD patterns of nanocomposites matrix show the coinciding of synthesized single-phase rhombohedral  $\text{Bi}_{0.4}\text{Sb}_{1.6}\text{Te}_3$  nanocrystals with its standard peaks in the ICSD.
- The 16hrs of mechanical milling is optimum for synthesizing a single-phase intermetallic compound of  $\text{Bi}_{0.4}\text{Sb}_{1.6}\text{Te}_3$  into extremely small nanocrystals size of 16nm and lattice strain of 0.18%.
- The successfulness in synthesizing artifact-free bulk nanocrystalline BiSbTe composited with 0.05wt.% Graphene at the last 5mins of the overall 16hrs of continuous mechanical milling.
- The sintered pellet of 5mins nanocomposite shows a lowering in its residual strain from 0.22% to 0.14%, while retaining the grain size refinement of 22nm instead of 20nm in its nanopowder form.
- The high-resolution DF-TEM micrographs confirm the formation of a homogenous elemental distribution within the synthesized single



phase in the 16hr milled  $\text{Bi}_{0.4}\text{Sb}_{1.6}\text{Te}_3$  nanopowder and the 5mins milled  $\text{Bi}_{0.4}\text{Sb}_{1.6}\text{Te}_3$ /Graphene nanocomposite.

- The statistical analysis on DF-TEM micrographs confirms the agreement of the average grain size for the pristine BiSbTe nanopowder at 16hrs of milling and the 5min BiSbTe/Graphene nanocomposite with their XRD outcomes.
- The HAADF-STEM images and EDS elemental mapping analysis verifies the homogenous elemental distribution and stable single phase of  $\text{Bi}_{0.4}\text{Sb}_{1.6}\text{Te}_3$  either in the pristine nanopowder or the multicomponent nanocomposites.
- The recognition and reporting for the first time the presence of a twinning interfacial defect in the BiSbTe/Graphene nanocomposites.
- The synthesized  $\text{Bi}_{0.4}\text{Sb}_{1.6}\text{Te}_3$  nanocrystals have reached an ultrahigh hardness value of 1.30GPa with an ultralow average grains size of 16nm after 16hrs of high energy milling, which is the highest reported for such TE system.
- The mechanical behavior of the  $\text{Bi}_{0.4}\text{Sb}_{1.6}\text{Te}_3$  nanocrystals has undergone remarkable improvements after compositing with graphene nanoplatelets resulting in the uppermost hardness of 1.78GPa at an average grains size of 20nm in the 5mins nanocomposite.
- The outcomes of  $I_{2D}/I_G$  ratio calculations confirm the crucial role of graphene addition time on its structure, as well as, the morphology, mechanical behavior, and thermoelectric performance of the synthesized nanocomposites.

- This is the first time observed and evidently reported such transition trend in graphene layered structure to its milling duration in a promising TE system such as  $\text{Bi}_{0.4}\text{Sb}_{1.6}\text{Te}_3$ .
- The structural transition has shifted to graphene with a single layer after its addition at the last 5mins of the overall 16hrs milling.
- The exceptional mechanical behavior and nanostructure of the synthesized 5mins nanocomposite confirm that the delayed addition times of graphene to  $\text{Bi}_{0.4}\text{Sb}_{1.6}\text{Te}_3$  nanopowder are favored; as it will shorten its milling duration to preserve its 2D nanostructure and advantage its exceptional properties.
- The pristine  $\text{Bi}_{0.4}\text{Sb}_{1.6}\text{Te}_3$  and 0.05wt% Graphene/ $\text{Bi}_{0.4}\text{Sb}_{1.6}\text{Te}_3$  nanocomposites have similar thermal behavior and matching onset temperatures; due to the small filler content of only 0.05wt% to avoid the effect of its high thermal conductivity on thermal stability of the multicomponent nanocomposites.
- The resultant heat flow curves confirm the high thermal stability of synthesized TE specimens from the room temperature until  $414^\circ\text{C}$ , at which the  $\text{Bi}_{0.4}\text{Sb}_{1.6}\text{Te}_3$  intermetallic converts into a mixture of two distinct phases.
- The narrow difference in initiating the endothermic phase transformation in the 2<sup>nd</sup> heating cycle confirms the remarkable thermal stability of synthesized TE specimens under multiple heating cycles, which gives an extra advantage of safety in operation.
- The variations in the normalized heating and cooling enthalpies for

first and second heating cycles are negligible as it is in narrow ranges of  $\pm 0.5\text{J/g}$ , which refers to the small volume fraction of the formed second phase from Te-phase separation in the first heating cycle.

- The electrical conductivity of pristine  $\text{Bi}_{0.4}\text{Sb}_{1.6}\text{Te}_3$  has considerably improved from  $231\text{S/cm}$  to  $344\text{S/cm}$  at  $322\text{K}$  after compositing it with graphene nanoplatelets owing to its high charge carrier density and mobility.
- The positive values of Seebeck coefficient confirm the effectiveness of resonant level doping of Bi-Te system with the Sb dopant to form the desired p-type  $\text{Bi}_{0.4}\text{Sb}_{1.6}\text{Te}_3$ .
- The maximizing of Seebeck coefficient in 5mins nanocomposite resulted in  $225\mu\text{V/K}$  at  $376\text{K}$ , which is comparable to  $168\mu\text{V/K}$  at  $375\text{K}$  for  $\text{Bi}_{0.5}\text{Sb}_{1.5}\text{Te}_3$  pellet derived from solution route; due to its preserved 2D nanostructure of graphene nanoplatelets.
- The 5mins nanocomposite has the highest power factor of  $1.73\text{mW/m.K}^2$  at  $324\text{K}$ , which slowly decreased to  $1.40\text{mW/m.K}^2$  at  $422\text{K}$  to overcome the solution derived BiSbTe and ternary alloy ingot; hence the highest values reported at the present.
- The thermal conductivity is lowest in the 5mins nanocomposite with  $0.723\text{W/m.K}$  at  $323\text{K}$  and  $0.815\text{W/m.K}$  at  $423\text{K}$ . This negligible change in its thermal conductivity over a wide temperature range indicates the strengthening of its phonon scatterings.
- The phonons contribution has been diminished extremely in the 5mins nanocomposite and not exceeding  $0.598\text{W/m.K}$  at  $423\text{K}$ , which

confirms the advantage of graphene nanocompositing in providing additional interfaces for maximizing phonons scattering.

- The 5mins nanocomposite achieved the optimum thermoelectric energy conversion of 0.70 at 323K till 398K with an isotropic thermoelectric performance over a wide temperature range and 25% improvements to the pristine BiSbTe.

## **5.2 Thesis Research: Recommendations**

The above conclusions give an accredited novelty to this thesis research on BiSbTe/Graphene nanocomposites and for further breakthroughs in TE field it is recommended to:

- Use elemental raw powders with uniform particle size for homogenous elemental distributions and uniform nanograins size across TE specimens.
- Characterize the chemical composition of elements within TE specimens for verification of impurities absence using an Inductive Coupled Plasma (ICP).
- Utilize the structural characterization techniques such as SEM or TEM on SPS pellets to investigate further their bulk nanostructured evolutions.
- Characterize the types, density, and location of the possible dislocations and twinning across TE specimens.
- Examine the micro-hardness values of bulk nanostructured BiSbTe/Graphene nanocomposites after their consolidating via SPS, which have a crucial rule on their nanostructure evolutions.

- Characterize the morphology of the indented surfaces of TE specimens using SEM-EDS to identify their failure mechanism and degree of reorientation.
- Evaluate the cracks propagation mechanism during the micro-indentation of TE specimens to upgrade further their hardness values.
- Identify the proper etching solution for metallurgical examination of eutectic layered microstructure in TE specimens towards confirming further their average grains size and phases distribution with TEM and XRD outcomes.
- Identify the lamellar structure of the metallurgically treated SPS pellets using SEM-EDS and investigate the mechanism of eutectic phase transformation and its influences on ZT parameters.
- Derive a ternary phase diagram for the BiSbTe system based on the obtained thermodynamic data on TE specimens.
- Conduct the transport measurements on the hole concentration and mobility in the designed operating temperatures of TE specimens using the Hall probe.
- Investigate the morphology, localization, and distribution of graphene nanoplatelets across TE specimens via detailed spectral mapping and chemical imaging of TE nanopowders using 3D Confocal Raman Microscopy (CRM).
- Evaluate the effect of replacing 0.05wt% graphene nanoplatelets with its carbon allotropes, especially the Single-Walled Carbon Nanotubes (SWCNTs) on TE performance of synthesized specimens.

- Evaluate the difference between the in-plane and out-of-plane thermal conductivity on the isotropic TE performance of synthesized TE nanocomposites.
- Conduct post-heat treatment on TE specimens for additional nanostructure stabilization and elimination of randomly distributed internal stresses in TE pellets via dislocations annihilation.
- Investigate the advantage of adding process control agents such as Ethanol and Stearic Acid on eliminating the welding of TE nanopowders during the mechanical milling process.
- Study the electrical and phonon transport mechanisms across TE specimens for comprehensive TE advancements.

## REFERENCES

- [1] W. Liu, J. Hu, S. Zhang, M. Deng, C.G. Han, Y. Liu, New trends, strategies and opportunities in thermoelectric materials: A perspective, *Mater. Today Phys.* 1 (2017) 50–60. doi:10.1016/j.mtphys.2017.06.001.
- [2] Z.H. Ge, Y.H. Ji, Y. Qiu, X. Chong, J. Feng, J. He, Enhanced thermoelectric properties of bismuth telluride bulk achieved by telluride-spilling during the spark plasma sintering process, *Scr. Mater.* 143 (2018) 90–93. doi:10.1016/j.scriptamat.2017.09.020.
- [3] A. Dey, O.P. Bajpai, A.K. Sikder, S. Chattopadhyay, M.A. Shafeeuulla Khan, Recent advances in CNT/graphene based thermoelectric polymer nanocomposite: A proficient move towards waste energy harvesting, *Renew. Sustain. Energy Rev.* 53 (2016) 653–671. doi:10.1016/j.rser.2015.09.004.
- [4] S. LeBlanc, Thermoelectric generators: Linking material properties and systems engineering for waste heat recovery applications, *Sustain. Mater. Technol.* 1 (2014) 26–35. doi:10.1016/j.susmat.2014.11.002.
- [5] A. Weidenkaff, Thermoelectricity for future sustainable energy, 00010 (2017) 1–11. doi:10.1051/epjconf/201714800010.
- [6] Y. Lan, A.J. Minnich, G. Chen, Z. Ren, Enhancement of thermoelectric figure-of-merit by a bulk nanostructuring approach, *Adv. Funct. Mater.* 20 (2010) 357–376. doi:10.1002/adfm.200901512.
- [7] F. Bonaccorso, L. Colombo, G. Yu, M. Stoller, V. Tozzini, A.C. Ferrari, R.S. Ruoff, V. Pellegrini, Graphene, related two-dimensional crystals, and hybrid systems for energy conversion and storage, *Science* (80-. ). 347 (2015). doi:10.1126/science.1246501.

- [8] “ S.Ragavendra, Lingaraju, P Balachandra Shetty, PG Mukunda, Mechanical Properties of short banana fibre reinforced natural rubber composites”, IJRSET, Vol. 2, Issue 5, pp 1652-1655, Elsevier. 3 (n.d.) 665. doi:10.1017/CBO9781107415324.004.
- [9] M.G. Kanatzidis, Nanostructured thermoelectrics: The new paradigm?, Chem. Mater. 22 (2010) 648–659. doi:10.1021/cm902195j.
- [10] J. Bludská, I. Jakubec, Č. Drašar, P. Lošťák, J. Horák, Structural defects in Cu-doped Bi<sub>2</sub>Te<sub>3</sub> single crystals, Philos. Mag. 87 (2007) 325–335. doi:10.1080/14786430600990337.
- [11] A. Muto, A. Minnich, B. Poudel, B. Yu, D. Vashaee, D. Wang, G. Chen, J. Liu, M.S. Dresselhaus, Q. Hao, X. Yan, X. Chen, Y. Ma, Y. Lan, Z. Ren, High-Thermoelectric Performance of Nanostructured Bismuth Antimony Telluride Bulk Alloys, Science (80-. ). 320 (2008) 634–638. doi:10.1126/science.1156446.
- [12] L.D. Hicks, The effect of quantum-well superlattices on the thermo-electric figure of merit, 281 (1996) 821–826.
- [13] S. Fan, J. Zhao, J. Guo, Q. Yan, J. Ma, H.H. Hng, P-type Bi<sub>0.4</sub>Sb<sub>1.6</sub>Te<sub>3</sub> nanocomposites with enhanced figure of merit, Appl. Phys. Lett. 96 (2010) 18–21. doi:10.1063/1.3427427.
- [14] A. Kommini, The Impact of Quantum Size Effects on Thermoelectric Performance in Semiconductor Nanostructures, (2017).
- [15] S. Fan, J. Zhao, Q. Yan, J. Ma, H.H. Hng, Influence of nanoinclusions on thermoelectric properties of n-type Bi<sub>2</sub>Te<sub>3</sub> nanocomposites, J. Electron. Mater. 40 (2011) 1018–1023. doi:10.1007/s11664-010-1487-7.
- [16] R.J. Mehta, Y. Zhang, C. Karthik, B. Singh, R.W. Siegel, T. Borca-Tasciuc, G.



- Ramanath, A new class of doped nanobulk high-figure-of-merit thermoelectrics by scalable bottom-up assembly, *Nat. Mater.* 11 (2012) 233–240. doi:10.1038/nmat3213.
- [17] R. Ahiska, H. Mamur, A review: Thermoelectric generators in renewable energy, *Int. J. Renew. Energy Res.* 4 (2014) 128–136. doi:10.1016/j.prevetmed.2004.11.005.
- [18] B.B. Liang, Y. Li, L.L. Xu, L.J. Wang, W. Jiang, Synthesis of Bi<sub>0.5</sub>Sb<sub>1.5</sub>Te<sub>3</sub>/Graphene Composite Powders, *Energy Environ. Mater.* 743–744 (2013) 83–87. doi:10.4028/www.scientific.net/MSF.743-744.83.
- [19] D.C. Cho, C.H. Lim, D.M. Lee, S.Y. Shin, C.H. Lee, Effect of Oxygen Content on Thermoelectric Properties of Sintered Bi-Te Based Compounds, *Mater. Sci. Forum.* 449–452 (2004) 905–908. doi:10.4028/www.scientific.net/MSF.449-452.905.
- [20] R. Orrù, R. Licheri, A.M. Locci, A. Cincotti, G. Cao, Consolidation/synthesis of materials by electric current activated/assisted sintering, *Mater. Sci. Eng. R Reports.* 63 (2009) 127–287. doi:10.1016/j.mser.2008.09.003.
- [21] M. Hamid Elsheikh, D.A. Shnawah, M.F.M. Sabri, S.B.M. Said, M. Haji Hassan, M.B. Ali Bashir, M. Mohamad, A review on thermoelectric renewable energy: Principle parameters that affect their performance, *Renew. Sustain. Energy Rev.* 30 (2014) 337–355. doi:10.1016/j.rser.2013.10.027.
- [22] O.H.A. Junior, N.H. Calderon, S. Silva De Souza, Characterization of a thermoelectric generator (TEG) system for waste heat recovery, *Energies.* 11 (2018). doi:10.3390/en11061555.
- [23] G.S. Nolas, J. Poon, M.G. Kanatzidis, Recent Developments Thermoelectric

- Materials, MRS Bull. 31 (2006) 199–205.
- [24] M. Saleemi, 2014-Nano-Engineered Thermoelectric Materials for Waste Heat Recovery - Mohsin Saleemi.pdf, (2014).
- [25] A.J. Minnich, M.S. Dresselhaus, Z.F. Ren, G. Chen, Bulk nanostructured thermoelectric materials: Current research and future prospects, *Energy Environ. Sci.* 2 (2009) 466–479. doi:10.1039/b822664b.
- [26] J. Androulakis, K.F. Hsu, R. Pcionek, H. Kong, C. Uher, J.J. D'Angelo, A. Downey, T. Hogan, M.G. Kanatzidis, Nanostructuring and high thermoelectric efficiency in p-type  $\text{Ag}(\text{Pb}_{1-y}\text{Sn}_y)\text{mSbTe}_{2+m}$ , *Adv. Mater.* 18 (2006) 1170–1173. doi:10.1002/adma.200502770.
- [27] X. Zhang, L.D. Zhao, Thermoelectric materials: Energy conversion between heat and electricity, *J. Mater.* 1 (2015) 92–105. doi:10.1016/j.jmat.2015.01.001.
- [28] D. Dragoman, M. Dragoman, Giant thermoelectric effect in graphene, *Appl. Phys. Lett.* 91 (2007) 23–26. doi:10.1063/1.2814080.
- [29] B. Liang, Z. Song, M. Wang, L. Wang, W. Jiang, Fabrication and thermoelectric properties of graphene/ $\text{Bi}_2\text{Te}_3$  composite materials, *J. Nanomater.* 2013 (2013). doi:10.1155/2013/210767.
- [30] L. Shi, Thermal and thermoelectric transport in nanostructures and low-dimensional systems, *Nanoscale Microscale Thermophys. Eng.* 16 (2012) 79–116. doi:10.1080/15567265.2012.667514.
- [31] X.H. An, S.D. Wu, Z.F. Zhang, R.B. Figueiredo, N. Gao, T.G. Langdon, Enhanced strength – ductility synergy in nanostructured Cu and Cu – Al alloys processed by high-pressure torsion and subsequent annealing, 66 (2012) 227–230. doi:10.1016/j.scriptamat.2011.10.043.

- [32] D.T. Morelli, G.A. Slack, High Lattice Thermal Conductivity Solids BT - High Thermal Conductivity Materials, (2006) 37–68. doi:10.1007/0-387-25100-6\_2.
- [33] C.H. Champness, P.T. Chiang, P. Parekh, THERMOELECTRIC PROPERTIES OF Bi<sub>2</sub>Te<sub>3</sub>–Sb<sub>2</sub>Te<sub>3</sub> ALLOYS, *Can. J. Phys.* 43 (1965) 653–669. doi:10.1139/p65-060.
- [34] D.A. Coronel, A.F.Z. de Azevedo, A.C. Campos, Política industrial e desenvolvimento econômico: a reatualização de um debate histórico, *Rev. Econ. Política.* 34 (2014) 103–119. doi:10.1016/j.applthermaleng.2014.01.074.
- [35] H. Alam, S. Ramakrishna, A review on the enhancement of figure of merit from bulk to nano-thermoelectric materials, *Nano Energy.* 2 (2013) 190–212. doi:10.1016/j.nanoen.2012.10.005.
- [36] S.A. Awadalla, A.W. Hunt, K.G. Lynn, H. Glass, C. Szeles, S.H. Wei, Isoelectronic oxygen-related defect in CdTe crystals investigated using thermoelectric effect spectroscopy, *Phys. Rev. B - Condens. Matter Mater. Phys.* 69 (2004) 1–4. doi:10.1063/1.2972017.
- [37] L. Su, Y. Gan, Advances in thermoelectric energy conversion nanocomposites, *Adv. Compos. Mater. Med. ....* 2 (2011). [http://cdn.intechopen.com/pdfs/14597/InTech-Advances\\_in\\_thermoelectric\\_energy\\_conversion\\_nanocomposites.pdf](http://cdn.intechopen.com/pdfs/14597/InTech-Advances_in_thermoelectric_energy_conversion_nanocomposites.pdf).
- [38] N.M. Alsaleh, E. Shoko, M. Arsalan, U. Schwingenschlögl, Thermoelectric Materials Under Pressure, *Phys. Status Solidi - Rapid Res. Lett.* 12 (2018) 1–8. doi:10.1002/pssr.201800083.
- [39] C. O'Dwyer, R. Chen, J.-H. He, J. Lee, K.M. Razeeb, Scientific and Technical Challenges in Thermal Transport and Thermoelectric Materials and Devices,

- ECS J. Solid State Sci. Technol. 6 (2017) N3058–N3064.  
doi:10.1149/2.0091703jss.
- [40] K. Agarwal, V. Kaushik, D. Varandani, A. Dhar, B.R. Mehta, Nanoscale thermoelectric properties of Bi<sub>2</sub>Te<sub>3</sub> - Graphene nanocomposites: Conducting atomic force, scanning thermal and kelvin probe microscopy studies, *J. Alloys Compd.* 681 (2016) 394–401. doi:10.1016/j.jallcom.2016.04.161.
- [41] K. Ahmad, C. Wan, M.A. Al-Eshaikh, A.N. Kadachi, Enhanced thermoelectric performance of Bi<sub>2</sub>Te<sub>3</sub> based graphene nanocomposites, *Appl. Surf. Sci.* (2018). doi:10.1016/j.apsusc.2018.10.163.
- [42] B. Crockford, F. Yildiz, K. Coogler, An Applied Comparison Study: Solar Energy vs . Thermoelectric Energy, 120th Am. Soc. Eng. Educ. Annu. Conf. Expo. (2013).
- [43] C.P. Bankston, T. Cole, R. Jones, R. Ewell, Experimental and systems studies of the alkali metal thermoelectric converter for aerospace power, *J. Energy.* 7 (1983) 442–448. doi:10.2514/3.62676.
- [44] S. Ortega, M. Ibáñez, Y. Liu, Y. Zhang, M. V. Kovalenko, D. Cadavid, A. Cabot, Bottom-up engineering of thermoelectric nanomaterials and devices from solution-processed nanoparticle building blocks, *Chem. Soc. Rev.* 46 (2017) 3510–3528. doi:10.1039/c6cs00567e.
- [45] H. Bark, J.S. Kim, H. Kim, J.H. Yim, H. Lee, Effect of multiwalled carbon nanotubes on the thermoelectric properties of a bismuth telluride matrix, *Curr. Appl. Phys.* 13 (2013) 1–4. doi:10.1016/j.cap.2013.01.019.
- [46] T. Caillat, M. Carle, D. Perrin, H. Scherrer, S. Scherrer, Study of the Bi-Sb-Te ternary phase diagram, *J. Phys. Chem. Solids.* 53 (1992) 227–232.

doi:10.1016/0022-3697(92)90049-J.

- [47] V. Tomashik, P. Perrot, Bismuth – Antimony – Tellurium, (1958) 242–254.
- [48] K. Biswas, J. He, I.D. Blum, C.I. Wu, T.P. Hogan, D.N. Seidman, V.P. Dravid, M.G. Kanatzidis, High-performance bulk thermoelectrics with all-scale hierarchical architectures, *Nature*. 489 (2012) 414–418. doi:10.1038/nature11439.
- [49] V. Viswanathan, T. Laha, K. Balani, A. Agarwal, S. Seal, Challenges and advances in nanocomposite processing techniques, *Mater. Sci. Eng. R Reports*. 54 (2006) 121–285. doi:10.1016/j.mser.2006.11.002.
- [50] B.A. Cook, J.L. Haringa, S.H. Han, B.J. Beaudry, Parasitic effects of oxygen on the thermoelectric properties of Si<sub>80</sub>Ge<sub>20</sub>doped with GaP and P, *J. Appl. Phys.* 72 (1992) 1423–1428. doi:10.1063/1.351702.
- [51] C. Wan, Y. Wang, N. Wang, W. Norimatsu, M. Kusunoki, K. Koumoto, Development of novel thermoelectric materials by reduction of lattice thermal conductivity, *Sci. Technol. Adv. Mater.* 11 (2010). doi:10.1088/1468-6996/11/4/044306.
- [52] K. Huang, Y. Yan, B. Li, Y. Li, K. Li, J. Li, A Novel Design of Thermoelectric Generator for Automotive Waste Heat Recovery, *Automot. Innov.* 1 (2018) 54–61. doi:10.1007/s42154-018-0006-z.
- [53] B. Ismail, W. Ahmed, Thermoelectric Power Generation Using Waste-Heat Energy as an Alternative Green Technology, *Recent Patents Electr. Eng.* 2 (2009) 27–39. doi:10.2174/1874476110902010027.
- [54] X. Guo, X. Jia, K. Jie, H. Sun, Y. Zhang, B. Sun, H. Ma, Thermoelectric transport properties and crystal growth of BiSbTe  $\times 3$  bulk materials produced

- by a unique high-pressure synthesis, *CrystEngComm*. 15 (2013) 7236–7242.  
doi:10.1039/c3ce40780b.
- [55] D. Patel, P.S.B. Mehta, Review of Use of Thermoelectricity as Renewable Energy Source, 2 (2015) 835–839.
- [56] R. Verdejo, M.M. Bernal, L.J. Romasanta, M.A. Lopez-Manchado, Graphene filled polymer nanocomposites, *J. Mater. Chem.* 21 (2011) 3301–3310.  
doi:10.1039/c0jm02708a.
- [57] A. Polozine, S. Sirotinskaya, L. Schaeffer, History of development of thermoelectric materials for electric power generation and criteria of their quality, *Mater. Res.* 17 (2014) 1260–1267. doi:10.1590/1516-1439.272214.
- [58] D. Parker, D.J. Singh, Potential Thermoelectric Performance from Optimization of Hole-Doped Bi<sub>2</sub>Se<sub>3</sub>, *Phys. Rev. X*. 1 (2011) 1–9.  
doi:10.1103/PhysRevX.1.021005.
- [59] H. Pang, Y.Y. Piao, Y.Q. Tan, G.Y. Jiang, J.H. Wang, Z.M. Li, Thermoelectric behaviour of segregated conductive polymer composites with hybrid fillers of carbon nanotube and bismuth telluride, *Mater. Lett.* 107 (2013) 150–153.  
doi:10.1016/j.matlet.2013.06.008.
- [60] H. Schock, G. Brereton, E. Case, J. D'Angelo, T. Hogan, M. Lyle, R. Maloney, K. Moran, J. Novak, C. Nelson, A. Panayi, T. Ruckle, J. Sakamoto, T. Shih, E. Timm, L. Zhang, G. Zhu, Prospects for Implementation of Thermoelectric Generators as Waste Heat Recovery Systems in Class 8 Truck Applications, *J. Energy Resour. Technol.* 135 (2013) 022001. doi:10.1115/1.4023097.
- [61] M. Scheele, N. Oeschler, K. Meier, A. Kornowski, C. Klinke, H. Weller, Synthesis and thermoelectric characterization of Bi<sub>2</sub>Te<sub>3</sub>nanoparticles, *Adv.*

- Funct. Mater. 19 (2009) 3476–3483. doi:10.1002/adfm.200901261.
- [62] K.S. Bhargavi, S.S. Kubakaddi, Scattering mechanisms and diffusion thermopower in a bilayer graphene, *Phys. E Low-Dimensional Syst. Nanostructures*. 52 (2013) 116–121. doi:10.1016/j.physe.2013.03.026.
- [63] C. Rudradawong, C. Ruttanapun, Effect of excess oxygen for CuFeO<sub>2</sub> delafossite on thermoelectric and optical properties, *Phys. B Condens. Matter*. 526 (2017) 21–27. doi:10.1016/j.physb.2017.09.046.
- [64] S.B. Riffat, X. Ma, Thermoelectrics: A review of present and potential applications, *Appl. Therm. Eng.* 23 (2003) 913–935. doi:10.1016/S1359-4311(03)00012-7.
- [65] H. Mishra, B.A. Cola, V. Rawat, P.B. Amama, K.G. Biswas, X. Xu, T.S. Fisher, T.D. Sands, Thermomechanical and thermal contact characteristics of bismuth telluride films electrodeposited on carbon nanotube arrays, *Adv. Mater.* 21 (2009) 4280–4283. doi:10.1002/adma.200803705.
- [66] B. Madavali, H.S. Kim, K.H. Lee, S.J. Hong, Enhanced Seebeck coefficient by energy filtering in Bi-Sb-Te based composites with dispersed Y<sub>2</sub>O<sub>3</sub> nanoparticles, *Intermetallics*. 82 (2017) 68–75. doi:10.1016/j.intermet.2016.11.002.
- [67] Y. Luo, J. Yang, Q. Jiang, L. Fu, Y. Xiao, W.X. Li, D. Zhang, Z. Zhou, Y. Cheng, Melting and solidification of bismuth antimony telluride under a high magnetic field: A new route to high thermoelectric performance, *Nano Energy*. 15 (2015) 709–718. doi:10.1016/j.nanoen.2015.05.032.
- [68] Recent Progress in Nanostructured Thermoelectric Materials, (n.d.) 1–19.
- [69] M.A. Abaza, Properties and Thermal Stabilization of Nanocrystalline Copper

- Via Solute Additions of Niobium, (2017). doi:<http://hdl.handle.net/10576/5775>.
- [70] S.K. Bux, J.P. Fleurial, R.B. Kaner, Nanostructured materials for thermoelectric applications, *Chem. Commun.* 46 (2010) 8311–8324. doi:10.1039/c0cc02627a.
- [71] J.L. Vickery, A.J. Patil, S. Mann, Fabrication of graphene-polymer nanocomposites with higher-order three-dimensional architectures, *Adv. Mater.* 21 (2009) 2180–2184. doi:10.1002/adma.200803606.
- [72] J. Tervo, A. Manninen, R. Ilola, Thermoelectric Materials Introduction.Pdf, (n.d.).
- [73] W. Xie, J. He, H.J. Kang, X. Tang, S. Zhu, M. Laver, S. Wang, J.R.D. Copley, C.M. Brown, Q. Zhang, T.M. Tritt, Identifying the specific nanostructures responsible for the high thermoelectric performance of (Bi,Sb)<sub>2</sub>Te<sub>3</sub>nanocomposites, *Nano Lett.* 10 (2010) 3283–3289. doi:10.1021/nl100804a.
- [74] W.H. Shin, K. Ahn, M. Jeong, J.S. Yoon, J.M. Song, S. Lee, W.S. Seo, Y.S. Lim, Enhanced thermoelectric performance of reduced graphene oxide incorporated bismuth-antimony-telluride by lattice thermal conductivity reduction, *J. Alloys Compd.* 718 (2017) 342–348. doi:10.1016/j.jallcom.2017.05.204.
- [75] R. Shams, Thermoelectric Properties of Materials Based on Double Filled Type-I Clathrates, (2015).
- [76] D.A. Wright, Thermoelectric properties of bismuth telluride and its alloys [7], *Nature.* 181 (1958) 834. doi:10.1038/181834a0.
- [77] A. Mehdizadeh Dehkordi, M. Zebarjadi, J. He, T.M. Tritt, Thermoelectric power factor: Enhancement mechanisms and strategies for higher performance thermoelectric materials, *Mater. Sci. Eng. R Reports.* 97 (2015) 1–22.



doi:10.1016/j.mser.2015.08.001.

- [78] M.A. El Qader, Structural, Electrical and Thermoelectric Properties of CrSi<sub>2</sub> thin films, (2011) 114.
- [79] T. Hu, M. Hu, Z. Li, H. Zhang, C. Zhang, J. Wang, X. Wang, Interlayer coupling in two-dimensional titanium carbide MXenes, *Phys. Chem. Chem. Phys.* 18 (2016) 20256–20260. doi:10.1039/C6CP01699E.
- [80] S. Twaha, J. Zhu, Y. Yan, B. Li, A comprehensive review of thermoelectric technology: Materials, applications, modelling and performance improvement, *Renew. Sustain. Energy Rev.* 65 (2016) 698–726. doi:10.1016/j.rser.2016.07.034.
- [81] S.-Y. Lee, S.-J. Park, Comprehensive review on synthesis and adsorption behaviors of graphene-based materials, *Carbon Lett.* 13 (2012) 73–87. doi:10.5714/CL.2012.13.2.073.
- [82] J. Tervo, A. Manninen, R. Ilola, H. Hänninen, State-of-the-art of thermoelectric materials processing, 2009.
- [83] Z. Xu, H. Wu, T. Zhu, C. Fu, X. Liu, L. Hu, J. He, J. He, X. Zhao, Attaining high mid-Temperature performance in (Bi,Sb)<sub>2</sub>Te<sub>3</sub> thermoelectric materials via synergistic optimization, *NPG Asia Mater.* 8 (2016). doi:10.1038/am.2016.134.
- [84] H.J. Goldsmid, Bismuth telluride and its alloys as materials for thermoelectric generation, *Materials (Basel).* 7 (2014) 2577–2592. doi:10.3390/ma7042577.
- [85] Y. Min, J.W. Roh, H. Yang, M. Park, S. Il Kim, S. Hwang, S.M. Lee, K.H. Lee, U. Jeong, Surfactant-free scalable synthesis of Bi<sub>2</sub>Te<sub>3</sub> and Bi<sub>2</sub>Se<sub>3</sub> nanoflakes and enhanced thermoelectric properties of Their Nanocomposites, *Adv. Mater.* 25 (2013) 1425–1429. doi:10.1002/adma.201203764.

- [86] R.S. Zhai, Y.H. Wu, T.J. Zhu, X.B. Zhao, Thermoelectric performance of p-type zone-melted Se-doped  $\text{Bi}_{0.5}\text{Sb}_{1.5}\text{Te}_3$  alloys, *Rare Met.* 37 (2018) 1–8. doi:10.1007/s12598-018-1005-2.
- [87] C. Li, X. Qin, Y. Li, D. Li, J. Zhang, H. Guo, H. Xin, C. Song, Simultaneous increase in conductivity and phonon scattering in a graphene nanosheets/ $(\text{Bi}_2\text{Te}_3)_{0.2}(\text{Sb}_2\text{Te}_3)_{0.8}$  thermoelectric nanocomposite, *J. Alloys Compd.* 661 (2016) 389–395. doi:10.1016/j.jallcom.2015.11.217.
- [88] J. Li, Q. Tan, J.F. Li, D.W. Liu, F. Li, Z.Y. Li, M. Zou, K. Wang, BiSbTe-based nanocomposites with high ZT: The effect of SiC nanodispersion on thermoelectric properties, *Adv. Funct. Mater.* 23 (2013) 4317–4323. doi:10.1002/adfm.201300146.
- [89] C. Zhang, Z. Peng, Z. Li, L. Yu, K.A. Khor, Q. Xiong, Controlled growth of bismuth antimony telluride  $\text{Bi}_x\text{Sb}_{2-x}\text{Te}_3$  nanoplatelets and their bulk thermoelectric nanocomposites, *Nano Energy.* 15 (2015) 688–696. doi:10.1016/j.nanoen.2015.05.022.
- [90] T. Zhang, Q. Zhang, J. Jiang, Z. Xiong, J. Chen, Y. Zhang, W. Li, G. Xu, Enhanced thermoelectric performance in p-type BiSbTe bulk alloy with nanoinclusion of ZnAlO, *Appl. Phys. Lett.* 98 (2011). doi:10.1063/1.3541654.
- [91] X. Mu, H. Zhou, D. He, W. Zhao, P. Wei, W. Zhu, X. Nie, H. Liu, Q. Zhang, Enhanced electrical properties of stoichiometric  $\text{Bi}_{0.5}\text{Sb}_{1.5}\text{Te}_3$  film with high-crystallinity via layer-by-layer in-situ Growth, *Nano Energy.* 33 (2017) 55–64. doi:10.1016/j.nanoen.2017.01.013.
- [92] W. Xie, X. Tang, Y. Yan, Q. Zhang, T.M. Tritt, High thermoelectric performance BiSbTe alloy with unique low-dimensional structure, *J. Appl. Phys.* 105 (2009).

doi:10.1063/1.3143104.

- [93] X. Wang, Y. Li, G. Liu, F. Shan, Achieving high power factor of p-type BiSbTe thermoelectric materials via adjusting hot-pressing temperature, *Intermetallics*. 93 (2018) 338–342. doi:10.1016/j.intermet.2017.10.015.
- [94] Z. Li, S. Han, Y. Pan, N. Miao, J. Zhou, H. Xu, Z. Sun, Origin of high thermoelectric performance with a wide range of compositions for  $\text{Bi}_x\text{Sb}_{2-x}\text{Te}_3$  single quintuple layers, *Phys. Chem. Chem. Phys.* 21 (2019) 1315–1323. doi:10.1039/C8CP06534A.
- [95] R. a. Fisher, M.R. Watt, W. Jud Ready, S. Il Cho, S.B. Lee, G. a. Snook, P. Kao, A.S. Best, G. Lota, K. Fic, E. Frackowiak, F. Béguin, M.D. Stoller, R.S. Ruoff, Arunabha Ghosg and Young Lee, O. Inganäs, S. Admassie, M. Vangari, T. Pryor, L. Jiang, J.-F. Lu, L.L. Wang, Q.-Y. Lai, H.-Y. Chu, Y. Zhao, G. Ćirić-Marjanovic, Y. Zhang, H. Feng, X. Wu, L.L. Wang, A. Zhang, T. Xia, H. Dong, X. Li, L. Zhang, T.H. Nguyen, A. Fraiwan, S. Choi, A.S. Aricò, P. Bruce, B. Scrosati, J. Tarascon, W.V.A.N. Schalkwijk, U. De Picardie, J. Verne, C. Umr-, G. Yu, X. Xie, L. Pan, Z. Bao, Y. Cui, L. Dong, Z. Chen, D. Yang, H. Lu, Recent advances in polyaniline composites with metals, metalloids and nonmetals, *Energy Environ. Sci.* 3 (2013) 4889–4899. doi:10.1038/nmat1368.
- [96] A.H. Li, M. Shahbazi, S.H. Zhou, G.X. Wang, C. Zhang, P. Jood, G. Peleckis, Y. Du, Z.X. Cheng, X.L. Wang, Y.K. Kuo, Electronic structure and thermoelectric properties of  $\text{Bi}_2\text{Te}_3$  crystals and graphene-doped  $\text{Bi}_2\text{Te}_3$ , *Thin Solid Films*. 518 (2010) 57–60. doi:10.1016/j.tsf.2010.03.124.
- [97] M. Ye, Z. Zhang, Y. Zhao, L. Qu, Graphene Platforms for Smart Energy Generation and Storage, *Joule*. 2 (2018) 245–268.

doi:10.1016/j.joule.2017.11.011.

- [98] W. Hou, X. Nie, W. Zhao, H. Zhou, X. Mu, W. Zhu, Q. Zhang, Fabrication and excellent performances of Bi<sub>0.5</sub>Sb<sub>1.5</sub>Te<sub>3</sub>/epoxy flexible thermoelectric cooling devices, *Nano Energy*. 50 (2018) 766–776. doi:<https://doi.org/10.1016/j.nanoen.2018.06.020>.
- [99] S.J. Kim, H. Choi, Y. Kim, J.H. We, J.S. Shin, H.E. Lee, M.W. Oh, K.J. Lee, B.J. Cho, Post ionized defect engineering of the screen-printed Bi<sub>2</sub>Te<sub>2.7</sub>Se<sub>0.3</sub> thick film for high performance flexible thermoelectric generator, *Nano Energy*. 31 (2017) 258–263. doi:10.1016/j.nanoen.2016.11.034.
- [100] H. Choi, Y.J. Kim, C.S. Kim, H.M. Yang, M.W. Oh, B.J. Cho, Enhancement of reproducibility and reliability in a high-performance flexible thermoelectric generator using screen-printed materials, *Nano Energy*. 46 (2018) 39–44. doi:10.1016/j.nanoen.2018.01.031.
- [101] J. He, M.G. Kanatzidis, V.P. Dravid, High performance bulk thermoelectrics via a panoramic approach, *Mater. Today*. 16 (2013) 166–176. doi:10.1016/j.mattod.2013.05.004.
- [102] J. Yang, L. Xi, W. Qiu, L. Wu, X. Shi, L. Chen, J. Yang, W. Zhang, C. Uher, D.J. Singh, On the tuning of electrical and thermal transport in thermoelectrics: an integrated theory–experiment perspective, *Npj Comput. Mater.* 2 (2016) 15015. doi:10.1038/npjcompumats.2015.15.
- [103] Y. Pei, X. Shi, A. Lalonde, H. Wang, L. Chen, G.J. Snyder, Convergence of electronic bands for high performance bulk thermoelectrics, *Nature*. 473 (2011) 66–69. doi:10.1038/nature09996.
- [104] H. Liu, X. Yuan, P. Lu, X. Shi, F. Xu, Y. He, Y. Tang, S. Bai, W. Zhang, L.

- Chen, Y. Lin, L. Shi, H. Lin, X. Gao, X. Zhang, H. Chi, C. Uher, Ultrahigh thermoelectric performance by electron and phonon critical scattering in  $\text{Cu}_2\text{Se}_{1-x}\text{Ix}$ , *Adv. Mater.* 25 (2013) 6607–6612. doi:10.1002/adma.201302660.
- [105] L.D. Zhao, S.H. Lo, Y. Zhang, H. Sun, G. Tan, C. Uher, C. Wolverton, V.P. Dravid, M.G. Kanatzidis, Ultralow thermal conductivity and high thermoelectric figure of merit in SnSe crystals, *Nature*. 508 (2014) 373–377. doi:10.1038/nature13184.
- [106] W. Xie, X. Tang, Y. Yan, Q. Zhang, T.M. Tritt, Unique nanostructures and enhanced thermoelectric performance of melt-spun BiSbTe alloys, *Appl. Phys. Lett.* 94 (2009) 1–4. doi:10.1063/1.3097026.
- [107] Q. Tan, L.D. Zhao, J.F. Li, C.F. Wu, T.R. Wei, Z.B. Xing, M.G. Kanatzidis, Thermoelectrics with earth abundant elements: Low thermal conductivity and high thermopower in doped SnS, *J. Mater. Chem. A*. 2 (2014) 17302–17306. doi:10.1039/c4ta04462b.
- [108] M. Zebarjadi, K. Esfarjani, M.S. Dresselhaus, Z.F. Ren, G. Chen, Perspectives on thermoelectrics: From fundamentals to device applications, *Energy Environ. Sci.* 5 (2012) 5147–5162. doi:10.1039/c1ee02497c.
- [109] A.S. Lemine, M.M. Zagho, T.M. Altahtamouni, N. Bensalah, Graphene a promising electrode material for supercapacitors—A review, *Int. J. Energy Res.* 42 (2018) 4284–4300. doi:10.1002/er.4170.
- [110] P. Chakraborty, T. Ma, A.H. Zahiri, L. Cao, Y. Wang, Carbon-Based Materials for Thermoelectrics, *Adv. Condens. Matter Phys.* 2018 (2018). doi:10.1155/2018/3898479.
- [111] X. Tang, W. Xie, H. Li, W. Zhao, Q. Zhang, M. Niino, Preparation and

- thermoelectric transport properties of high-performance p-type Bi<sub>2</sub>Te<sub>3</sub> with layered nanostructure, *Appl. Phys. Lett.* 90 (2007) 1–4. doi:10.1063/1.2425007.
- [112] D. Xie, J. Xu, G. Liu, Z. Liu, H. Shao, X. Tan, J. Jiang, H. Jiang, Synergistic optimization of thermoelectric performance in p-type Bi<sub>0.48</sub>Sb<sub>1.52</sub>Te<sub>3</sub>/graphene composite, *Energies*. 9 (2016) 1–9. doi:10.3390/en9040236.
- [113] G. Zheng, X. Su, H. Xie, Y. Shu, T. Liang, X. She, W. Liu, Y. Yan, Q. Zhang, C. Uher, M.G. Kanatzidis, X. Tang, High thermoelectric performance of p-BiSbTe compounds prepared by ultra-fast thermally induced reaction, *Energy Environ. Sci.* 10 (2017) 2638–2652. doi:10.1039/c7ee02677c.
- [114] A.F. May, J.P. Fleurial, G.J. Snyder, Thermoelectric performance of lanthanum telluride produced via mechanical alloying, *Phys. Rev. B - Condens. Matter Mater. Phys.* 78 (2008) 1–12. doi:10.1103/PhysRevB.78.125205.
- [115] S.W.S.I.S.W.S.I.S.I. Kim, H. a Mun, H.S. Kim, S.W. Hwang, J.W. Roh, D.J. Yang, W.H. Shin, X.S. Li, Y.H. Lee, G.J. Snyder, S.W.S.I.S.W.S.I.S.I. Kim, K.H.H. Lee, H. a Mun, H.S. Kim, S.W. Hwang, J.W. Roh, D.J. Yang, W.H. Shin, X.S. Li, Y.H. Lee, G.J. Snyder, S.W.S.I.S.W.S.I.S.I. Kim, Supplementary Materials for Thermoelectrics. Dense dislocation arrays embedded in grain boundaries for high-performance bulk thermoelectrics., *Science* (80-. ). 348 (2015) 109–114. doi:10.1126/science.aaa4166.
- [116] T. Zhang, J. Jiang, Y. Xiao, Y. Zhai, S. Yang, G. Xu, In Situ Precipitation of Te Nanoparticles in p-Type BiSbTe and the Effect on Thermoelectric Performance, *ACS Appl. Mater. Interfaces*. 5 (2013) 3071–3074. doi:10.1021/am303145v.
- [117] Q. Zhang, X. Ai, L. Wang, Y. Chang, W. Luo, W. Jiang, L. Chen, Improved

- thermoelectric performance of silver nanoparticles-dispersed Bi<sub>2</sub>Te<sub>3</sub>composites deriving from hierarchical two-phased heterostructure, *Adv. Funct. Mater.* 25 (2015) 966–976. doi:10.1002/adfm.201402663.
- [118] W. Liu, Q. Jie, H.S. Kim, Z. Ren, Current progress and future challenges in thermoelectric power generation: From materials to devices, *Acta Mater.* 87 (2015) 357–376. doi:10.1016/j.actamat.2014.12.042.
- [119] Y. Lan, B. Poudel, Y. Ma, D. Wang, M.S. Dresselhaus, G. Chen, Z. Ren, Structure study of bulk nanograined thermoelectric bismuth antimony telluride, *Nano Lett.* 9 (2009) 1419–1422. doi:10.1021/nl803235n.
- [120] H. Kessel, J. Hennicke, R. Kirchner, T. Kessel, Rapid sintering of novel materials by FAST/SPS—Further development to the point of an industrial production process with high cost efficiency, *FCT Syst. GmbH.* (2010). <http://www.fct-systeme.de/download/20100225123420/FCT-Sintered-Materials.pdf>.
- [121] L.E. Bell, Cooling , Heating , Generating Heat with and Recovering Waste Thermoelectric, *Science* (80-. ). 321 (2008) 1457–1461. doi:10.1126/science.1158899.
- [122] W.R. Matizamhuka, Spark plasma sintering (SPS) - An advanced sintering technique for structural nanocomposite materials, *J. South. African Inst. Min. Metall.* 116 (2016) 1171–1180. doi:10.17159/2411-9717/2016/v116n12a12.
- [123] M. Pellizzari, A. Fedrizzi, M. Zadra, Spark plasma co-sintering of mechanically milled tool steel and high speed steel powders, *Materials (Basel).* 9 (2016). doi:10.3390/ma9060482.
- [124] A. Soni, Y. Shen, M. Yin, Y. Zhao, L. Yu, X. Hu, Z. Dong, K.A. Khor, M.S.

- Dresselhaus, Q. Xiong, Interface driven energy filtering of thermoelectric power in spark plasma sintered Bi<sub>2</sub>Te<sub>2.7</sub>Se<sub>0.3</sub>nanoplatelet composites, *Nano Lett.* 12 (2012) 4305–4310. doi:10.1021/nl302017w.
- [125] Y. Zhang, H. Ma, B. Sun, B. Liu, H. Liu, L. Kong, B. Liu, X. Jia, X. Chen, Thermoelectric performance of graphene composited BiSbTe bulks by high pressure synthesis, *J. Alloys Compd.* 715 (2017) 344–348. doi:10.1016/j.jallcom.2017.05.004.
- [126] P. Barvinschi, D. Tamas, R. Baies, Precise lattice parameter determination of spinel MgAl<sub>2</sub>O<sub>4</sub> from X-ray powder diffraction patterns, *XLIX* (2006) 32–35.
- [127] F. Sondermaschinen, G. Dieselstra, D. Telefon, *Dsp 510 / 515*, (n.d.).
- [128] G. Li, K.R. Gadelrab, T. Souier, P.L. Potapov, G. Chen, M. Chiesa, Mechanical properties of Bi<sub>x</sub>Sb<sub>2-x</sub>Te<sub>3</sub> nanostructured thermoelectric material, *Nanotechnology.* 23 (2012). doi:10.1088/0957-4484/23/6/065703.
- [129] J. Oh, H. Yoo, J. Choi, J.Y. Kim, D.S. Lee, M.J. Kim, J.C. Lee, W.N. Kim, J.C. Grossman, J.H. Park, S.S. Lee, H. Kim, J.G. Son, Significantly reduced thermal conductivity and enhanced thermoelectric properties of single- and bi-layer graphene nanomeshes with sub-10 nm neck-width, *Nano Energy.* 35 (2017) 26–35. doi:10.1016/j.nanoen.2017.03.019.
- [130] D. Němeček, G.J. Thomas, Raman Spectroscopy of Viruses and Viral Proteins, *Front. Mol. Spectrosc.* (2009) 553–595. doi:10.1016/B978-0-444-53175-9.00016-7.
- [131] R. Spectroscopy, Perspectives on Raman spectroscopy of Graphene, (2004) 5–8.
- [132] Q. Wang, D. Ph, Cryo-TEM sample preparation for molecular imaging, (n.d.).



- [133] B. Nanjwade, Thermal analysis, (2014).
- [134] L. Waguespack, R. Blaine, Design of a New DSC Cell with Tzero™ Technology, Proc. 29th Conf. North Am. Therm. Anal. Soc. (2001) 721–727.
- [135] P.A. Cloud, Product specification, Eng. Proced. Handb. (2008) 191–198. doi:10.1016/b978-081551410-7.50030-1.
- [136] E.I. Bîru, H. Iovu, Graphene Nanocomposites Studied by Raman Spectroscopy, Raman Spectrosc. (2018). doi:10.5772/intechopen.73487.
- [137] M. Wall, The Raman spectroscopy of graphene and the determination of layer thickness, Thermo Sci. Appl. Note. (2011) 52252.
- [138] L.G. Cañado, K. Takai, T. Enoki, M. Endo, Y.A. Kim, H. Mizusaki, A. Jorio, L.N. Coelho, R. Magalhães-Paniago, M.A. Pimenta, General equation for the determination of the crystallite size  $l_a$  of nanographite by Raman spectroscopy, Appl. Phys. Lett. 88 (2006) 2–5. doi:10.1063/1.2196057.
- [139] A. Bhardwaj, A.K. Shukla, S.R. Dhakate, D.K. Misra, Graphene boosts thermoelectric performance of a Zintl phase compound, RSC Adv. 5 (2015) 11058–11070. doi:10.1039/c4ra15456h.
- [140] R. Beams, L. Gustavo Cañado, L. Novotny, Raman characterization of defects and dopants in graphene, J. Phys. Condens. Matter. 27 (2015). doi:10.1088/0953-8984/27/8/083002.
- [141] X. Fan, F. Yang, Z. Rong, X. Cai, G. Li, Characterization and thermoelectric properties of Bi<sub>0.4</sub>Sb<sub>1.6</sub>Te<sub>3</sub> nanostructured bulk prepared by mechanical alloying and microwave activated hot pressing, Ceram. Int. 41 (2015) 6817–6823. doi:10.1016/j.ceramint.2015.01.130.
- [142] X. Zhang, Y. An, J. Han, W. Han, G. Zhao, X. Jin, Graphene nanosheet

- reinforced ZrB<sub>2</sub>-SiC ceramic composite by thermal reduction of graphene oxide, *RSC Adv.* 5 (2015) 47060–47065. doi:10.1039/c5ra05922d.
- [143] I.M. Hutchings, The contributions of David Tabor to the science of indentation hardness, *J. Mater. Res.* 24 (2009) 581–589. doi:10.1557/jmr.2009.0085.
- [144] T. Li, A.D. Pickel, Y. Yao, Y. Chen, Y. Zeng, S.D. Lacey, Y. Li, Y. Wang, J. Dai, Y. Wang, B. Yang, M.S. Fuhrer, A. Marconnet, C. Dames, D.H. Drew, L. Hu, Thermoelectric properties and performance of flexible reduced graphene oxide films up to 3,000 K, *Nat. Energy.* 3 (2018) 148–156. doi:10.1038/s41560-018-0086-3.
- [145] H.W. Zhang, G. Subhash, X.N. Jing, L.J. Kecskes, R.J. Dowding, Evaluation of hardness-yield strength relationships for bulk metallic glasses, *Philos. Mag. Lett.* 86 (2006) 333–345. doi:10.1080/09500830600788935.
- [146] S.B.A. Nemesis, Simultaneous Determination of the Seebeck Coefficient and Electrical Conductivity – Your Partner In Testing Thermoelectrics, (n.d.).
- [147] A. Mycroft, R. Sharp, The FLaSH Project, Rich.Recoil.Org. (n.d.).
- [148] X. Lu, Q.H. Tan, Q. Xiong, J. Zhang, Raman spectroscopy of isotropic two-dimensional materials beyond graphene, *Springer Ser. Mater. Sci.* 276 (2019) 29–52. doi:10.1007/978-981-13-1828-3\_2.
- [149] C. Gómez-Navarro, J.C. Meyer, R.S. Sundaram, A. Chuvilin, S. Kurasch, M. Burghard, K. Kern, U. Kaiser, Atomic structure of reduced graphene oxide, *Nano Lett.* 10 (2010) 1144–1148. doi:10.1021/nl9031617.
- [150] Z. Li, S. Han, Y. Pan, N. Miao, J. Zhou, H. Xu, Z. Sun, Origin of high thermoelectric performance with a wide range of compositions for BiXSb<sub>2-x</sub>Te<sub>3</sub> single quintuple layers, *Phys. Chem. Chem. Phys.* 21 (2019) 1315–1323.

doi:10.1039/c8cp06534a.

- [151] Z. Dong, H. Xu, F. Liang, C. Luo, C. Wang, Z.Y. Cao, X.J. Chen, J. Zhang, X. Wu, Raman characterization on two-dimensional materials-based thermoelectricity, *Molecules*. (2019). doi:10.3390/molecules24010088.
- [152] A. Bachmaier, G.B. Rathmayr, EARLY CAREER SCHOLARS IN MATERIALS SCIENCE : ARTICLE High strength nanocrystalline Cu – Co alloys with high tensile ductility, (2018) 1–11. doi:10.1557/jmr.2018.185.
- [153] Y.S. Wang, L.L. Huang, D. Li, J. Zhang, X.Y. Qin, Enhanced thermoelectric performance of Bi<sub>0.4</sub>Sb<sub>1.6</sub>Te<sub>3</sub>based composites with CuInTe<sub>2</sub>inclusions, *J. Alloys Compd.* 758 (2018) 72–77. doi:10.1016/j.jallcom.2018.05.035.
- [154] H. Choi, Y.J. Kim, C.S. Kim, H.M. Yang, M.W. Oh, B.J. Cho, Enhancement of reproducibility and reliability in a high-performance flexible thermoelectric generator using screen-printed materials, *Nano Energy*. 46 (2018) 39–44. doi:10.1016/j.nanoen.2018.01.031.
- [155] J. R. Connolly, *Diffraction Basics* , Part 2, *Introd. to X-Ray Powder Diffr.* 2 (2012) 1–12.
- [156] B. Trawiński, B. Bochentyn, N. Gostkowska, M. Łapiński, T. Miruszewski, B. Kusz, Structure and thermoelectric properties of bismuth telluride—Carbon composites, *Mater. Res. Bull.* 99 (2018) 10–17. doi:10.1016/j.materresbull.2017.10.043.
- [157] Y. Eom, F. Kim, S.E. Yang, J.S. Son, H.G. Chae, Rheological design of 3D printable all-inorganic inks using BiSbTe-based thermoelectric materials, *J. Rheol.* (N. Y. N. Y). 63 (2019) 291–304. doi:10.1122/1.5058078.
- [158] Y. Luo, J. Yang, Q. Jiang, L. Fu, Y. Xiao, W.X. Li, D. Zhang, Z. Zhou, Y. Cheng,

- Melting and solidification of bismuth antimony telluride under a high magnetic field: A new route to high thermoelectric performance, *Nano Energy*. 15 (2015) 709–718. doi:10.1016/j.nanoen.2015.05.032.
- [159] W. Liu, Q. Jie, H.S. Kim, Z. Ren, Current progress and future challenges in thermoelectric power generation: From materials to devices, *Acta Mater.* 87 (2015) 357–376. doi:10.1016/j.actamat.2014.12.042.
- [160] J. Kim, L.J. Cote, F. Kim, W. Yuan, K.R. Shull, J. Huang, Graphene oxide sheets at interfaces, *J. Am. Chem. Soc.* 132 (2010) 8180–8186. doi:10.1021/ja102777p.
- [161] B.Y. Zhao, Y. Zhu, E.J. Lavernia, Strategies for Improving Tensile Ductility of Bulk Nanostructured Materials \*\*, (2010) 769–778. doi:10.1002/adem.200900335.
- [162] C. Soldano, A. Mahmood, E. Dujardin, Production, properties and potential of graphene, *Carbon* N. Y. 48 (2010) 2127–2150. doi:10.1016/j.carbon.2010.01.058.
- [163] X. Tang, W. Xie, H. Li, W. Zhao, Q. Zhang, M. Niino, Preparation and thermoelectric transport properties of high-performance p-type Bi<sub>2</sub>Te<sub>3</sub> with layered nanostructure, *Appl. Phys. Lett.* 90 (2007) 1–4. doi:10.1063/1.2425007.
- [164] J.C. Meyer, A.K. Geim, M.I. Katsnelson, K.S. Novoselov, T.J. Booth, S. Roth, The structure of suspended graphene sheets, *Nature*. 446 (2007) 60–63. doi:10.1038/nature05545.
- [165] G.S. Nolas, J. Poon, Recent Developments Thermoelectric Materials, 31 (2016) 199–205.
- [166] I. Terasaki, Introduction to thermoelectricity, *Mater. Energy Convers. Devices*. (2005) 339–357. doi:10.1533/9781845690915.3.339.

- [167] F.J. Disalvo, Thermoelectric cooling and power generation, *Science* (80-. ). 285 (1999) 703–706. doi:10.1126/science.285.5428.703.
- [168] K. Ahmad, C. Wan, P. an Zong, Thermoelectric properties of BiSbTe/graphene nanocomposites, *J. Mater. Sci. Mater. Electron.* 30 (2019) 11923–11930. doi:10.1007/s10854-019-01538-z.
- [169] D. Zhang, J. Lei, W. Guan, Z. Ma, C. Wang, L. Zhang, Z. Cheng, Y. Wang, Enhanced thermoelectric performance of BiSbTe alloy: Energy filtering effect of nanoprecipitates and the effect of SiC nanoparticles, *J. Alloys Compd.* (2019) 1276–1283. doi:10.1016/j.jallcom.2019.01.084.
- [170] L. Chen, D. Mei, Y. Wang, Y. Li, Ni barrier in Bi<sub>2</sub>Te<sub>3</sub>-based thermoelectric modules for reduced contact resistance and enhanced power generation properties, *J. Alloys Compd.* 796 (2019) 314–320. doi:10.1016/j.jallcom.2019.04.293.
- [171] Y.C. Dou, X.Y. Qin, D. Li, Y.Y. Li, H.X. Xin, J. Zhang, Y.F. Liu, C.J. Song, L. Wang, Enhanced thermoelectric performance of BiSbTe-based composites incorporated with amorphous Si<sub>3</sub>N<sub>4</sub> nanoparticles, *RSC Adv.* 5 (2015) 34251–34256. doi:10.1039/c5ra04428f.
- [172] Y. Min, J.W. Roh, H. Yang, M. Park, S. Il Kim, S. Hwang, S.M. Lee, K.H. Lee, U. Jeong, Surfactant-free scalable synthesis of Bi<sub>2</sub>Te<sub>3</sub> and Bi<sub>2</sub>Se<sub>3</sub> nanoflakes and enhanced thermoelectric properties of Their Nanocomposites, *Adv. Mater.* 25 (2013) 1425–1429. doi:10.1002/adma.201203764.
- [173] X. Hu, Q. Xiang, D. Kong, X. Fan, B. Feng, Z. Pan, P. Liu, R. Li, G. Li, Y. Li, The effect of Ni/Sn doping on the thermoelectric properties of BiSbTe polycrystalline bulks, *J. Solid State Chem.* 277 (2019) 175–181.

doi:10.1016/j.jssc.2019.06.006.

- [174] J. Qiu, Y. Yan, T. Luo, K. Tang, L. Yao, J. Zhang, M. Zhang, X. Su, G. Tan, H. Xie, M.G. Kanatzidis, C. Uher, X. Tang, 3D Printing of highly textured bulk thermoelectric materials: mechanically robust BiSbTe alloys with superior performance, *Energy Environ. Sci.* (2019). doi:10.1039/c9ee02044f.